Lateral Load Effect on Railway Tapered Roller Bearing Performance

Constantine Tarawneh, Ph.D.
Director, UTCRS
Mechanical Engineering Department
University of Texas Rio Grande Valley

Arturo Fuentes, Ph.D.
Mechanical Engineering Department
University of Texas Rio Grande Valley

Abel Sanchez-Trinidad
Graduate Research Assistant
Mechanical Engineering Department
University of Texas Rio Grande Valley

Joseph Montalvo
Engineering Research Associate III
Mechanical Engineering Department
University of Texas Rio Grande Valley

A Report on Research Sponsored by

University Transportation Center for Railway Safety (UTCRS)

University of Texas Rio Grande Valley (UTRGV)

December 2025

Technical Report Documentation Page

1. Report No. UTCRS-UTRGV-M4CY24	2. Government Accession No.	3. Recipient's Catalog No.
4. Title and Subtitle Lateral Load Effect on Railway Tapered Roller Bearing Performance		5. Report Date December 31, 2025
		6. Performing Organization Code UTCRS-UTRGV
7. Author(s) Constantine Tarawneh, Arturo Fuentes, Abel Sanchez-Trinidad, and Joseph Montalvo		8. Performing Organization Report No. UTCRS-UTRGV-M4CY24
9. Performing Organization Name and Address University Transportation Center for Railway Safety (UTCRS) University of Texas Rio Grande Valley (UTRGV) 1201 W. University Dr. Edinburg, TX 78539		10. Work Unit No. (TRAIS)
		11. Contract or Grant No. 69A3552348340
12. Sponsoring Agency Name and Address U.S. Department of Transportation (USDOT) University Transportation Centers Program 1200 New Jersey Ave. SE Washington, DC, 20590		13. Type of Report and Period Covered Project Report June 1, 2024 – December 31, 2025
		14. Sponsoring Agency Code USDOT UTC Program
15. Supplementary Notes		

16. Abstract

Lateral forces are a critical factor in railroad tapered roller bearing performance. To improve the reliability and safety of railway systems, vibration and thermal signatures can be powerful diagnostic and prognostic tools for monitoring railway bearing health. While temperature variations can signal spall deterioration, they often become evident only after extensive damage. Therefore, understanding the effects of lateral loading on railroad tapered-roller bearings, including vibration and temperature behavior, under varying train speeds and loads is crucial. Unfortunately, there is limited publicly available research in this area.

Motivated by this area of opportunity, researchers at the University Transportation Center for Railway Safety (UTCRS) developed a dynamic bearing test rig to investigate the effects of lateral loading on bearing performance. The proposed study focuses on Association of American Railroads (AAR) class F and K bearings, widely used in freight rail service. A hydraulic cylinder setup applied lateral loads up to 60 kN (13.5 kips), mimicking forces experienced during hunting, track irregularities, and curves. Healthy and defective bearings were used for the experiments.

This study offers a unique contribution by exploring how lateral loads affect bearing vibration (in addition to temperature), providing insights into factors influencing bearing performance in the rail industry. The aim is to improve the long-term reliability and safety of rail systems by understanding how to mitigate performance-compromising issues. Based on the findings of this study, the research team plans to optimize onboard vibration, temperature, and load measurement sensors for more accurate and reliable monitoring of bearing condition in rail revenue service.

17. Key Words L/V ratio, Roller bearings, Temperature measurement, Mechanical vibration	18. Distribution Statement This report is available for download from https://www.utrgv.edu/railwaysafety/research/mechanical/index.htm

19. Security Classification (of this report) None	20. Security Classification (of this page) None	21. No. of Pages 113	22. Price

EXAMINING THE EFFECTS OF LATERAL LOADING ON RAILROAD TAPERED ROLLER BEARINGS

A Thesis

by

ABEL DAVID SANCHEZ TRINIDAD

Submitted in Partial Fulfillment of the

Requirements for the Degree of

MASTER OF SCIENCE IN ENGINEERING

Major Subject: Mechanical Engineering

The University of Texas Rio Grande Valley
May 2026

EXAMINING THE EFFECTS OF LATERAL LOADING

ON RAILROAD TAPERED ROLLER BEARINGS

A Thesis
by
ABEL DAVID SANCHEZ TRINIDAD

COMMITTEE MEMBERS

Dr. Constantine Tarawneh
Chair of Committee

Dr. Arturo Fuentes
Co-Chair of Committee

Dr. Heinrich Foltz
Committee Member

May 2026

ABSTRACT

Sanchez Trinidad, Abel D., Examining the Effects of Lateral Loading on Railroad Tapered Roller Bearings. Master of Science in Engineering (MSE), May 2026, 87 pp., 15 tables, 71 figures, 31 references.

The loading conditions experienced by freight railcar bearings vary as a function of vehicle operating conditions. Under static conditions, bearings are primarily subjected to radial loads transmitted through the wheelset. During operation, however, track irregularities, braking events, railcar load imbalances, and curving introduce complex impact, longitudinal, and lateral forces in addition to the normal radial loading. These lateral forces increase friction within the bearing raceways, which could accelerate wear and potentially lead to premature spall initiation and propagation. While prior research at the University Transportation Center for Railway Safety (UTCRS) has demonstrated that vibration signatures can be used to detect bearing defect development, the influence of lateral loading on bearing performance across varying load and speed conditions remains largely unexplored. A test fixture capable of applying lateral forces up to 50% of the applied vertical load was designed, fabricated, and integrated onto the Single Bearing Tester (SBT) at the University of Texas Rio Grande Valley (UTRGV). A series of experiments was conducted under empty and fully loaded conditions at multiple operating speeds to quantify the effects of lateral loading on bearing temperature and vibration response. The results indicate that using this experimental fixture for the application of lateral load produced an abrupt increase in operating temperature on the inboard side of the bearing, accompanied by a decrease in temperature on the outboard. In experiments performed with a defective bearing, it

was noticed that for every 4.45 kN (1 kip) of lateral load, there is approximately a 1°C (1.8°F) increase in bearing operating temperature. The lateral load forces the rollers into a more constrained state against the inboard cone rib, significantly reducing internal clearance and altering the dynamic behavior by limiting their ability to skew. This shift in the internal load path concentrates sliding friction primarily at the inboard rib, creating localized heating while simultaneously decreasing the friction in the outboard cone. Changes in vibration levels were also observed with the introduction of lateral loading on defective bearings. Moreover, applying a continuous lateral load for longer durations produces cyclic temperature trending events exhibited in both unloaded and fully loaded operating conditions.

DEDICATION

Quiero dedicar esta tesis a mi familia, por ser el pilar por lo que he logrado. A mi padre, David Sánchez Zavala, quien me guió desde pequeño por el camino que me llevó a convertirme en ingeniero. Gracias por darme el conocimiento y las herramientas necesarias para seguir adelante, por acompañarme en cada paso y por apoyarme en cada proyecto que yo hacía. Papá, gracias por siempre estar ahí desde pequeño, tú me has formado en el hombre que soy hoy. A mi madre, Ileana Trinidad Román, por su amor incondicional y su apoyo constante. Gracias por estar siempre a mi lado, por impulsarme a seguir adelante y por luchar por mí en todo momento. Sin ti, no habría sido posible alcanzar mis metas. A mi hermana, Yuliana Sánchez Trinidad, por tu apoyo en los momentos difíciles y por darme fuerza cuando más lo necesitaba. Gracias por siempre protegerme y por ser un apoyo incondicional cuando sentía que todo se derrumbaba. A mi querida, Citlali Zuñiga, por apoyarme en este camino. Gracias por creer en mí, por tu ayuda incondicional y por caminar a mi lado en esta etapa. Gracias por tu amor incondicional

Los amo con todo mi corazón.

ACKNOWLEDGEMENTS

I want to thank my friends Jeff, Santana, Diego A., David, Eddy, Teresa, Curtis, Diego L., Aaron, Roger, Lee, Joseph, Sergio, Alex, Daniel, and Carlos R., as well as the faculty of the UTCRS team. Without them, this journey would have been much more difficult. Thank you all for being part of my life and for creating many memories together that I will always cherish and look back on. I hope we continue to be part of each other's lives and see one another achieve our goals. To the UTRGV Baja Racing Team, I had the privilege of serving as captain for five years. I will always cherish the many memories we made, especially during those meetings when we came together to build the car.

To Dr. Arturo Fuentes, thank you for your mentorship in Baja and UTCRS. Your guidance and the time you spent helping me navigate my early career have made all the difference. I am deeply appreciative of the time you have dedicated to my growth and for the technical expertise you have shared with me.

Lastly, I would like to thank Dr. Constantine Tarawneh. You gave me my first glimpse into engineering during your summer camps back in 2014, which led to my decision to become a mechanical engineer. Thank you for welcoming me into your research center, for your constant guidance, and for investing so much time in my future. Your support has truly shaped my experience as both a student and an engineer.

The author wishes to acknowledge the University Transportation Center for Railway Safety (UTCRS) for funding this project under the USDOT UTC Program Grant No. 69A3552348340.

DISCLAIMER

The contents of this thesis reflect the views of the authors who are responsible for the facts and the accuracy of the information presented herein. This document is disseminated under the sponsorship of the U.S. Department of Transportation's University Transportation Centers Program, in the interest of information exchange. The U.S. Government assumes no liability for the contents or use thereof.

TABLE OF CONTENTS

Page

LIST OF TABLES

Page

LIST OF FIGURES

Page

CHAPTER I

INTRODUCTION

1.1 Introduction

During operation, freight railcars are subjected to lateral forces arising from vehicle-track interaction, including track geometry variations and curve negotiation. Flange contact, creepage, and centrifugal effects increase lateral forces as the freight car moves through a curved track. A railcar is supported by two bogies, each containing two wheelsets and four bearings, as shown in Figure 1. The weight of the railcar is distributed between the bogies, which allow relative motion as the railcar negotiates a curve. To better understand how these lateral forces are transmitted and resisted, it is important to understand how a tapered roller bearing works in a railcar.

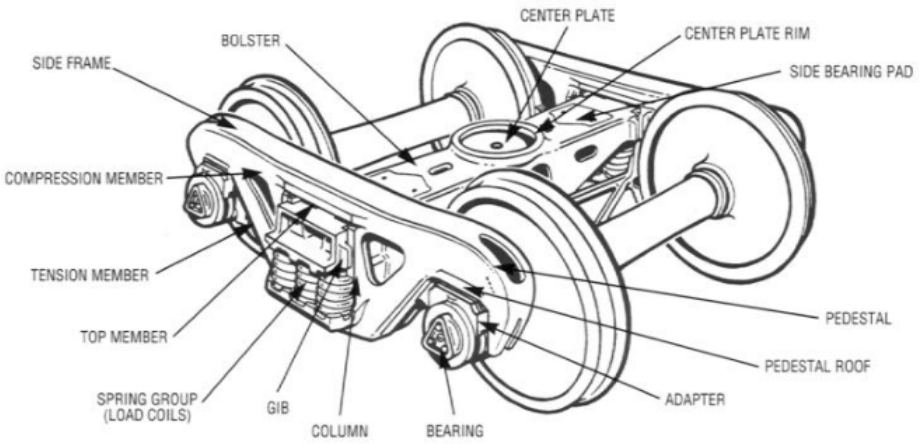

Figure 1. Railcar bogie components [1]

1.2 Tapered Roller Bearing

The wheelsets on the bogies of a railroad freight car use double-row tapered roller bearings, which are designed to accommodate high radial loads while also resisting axial forces generated during dynamic operation. The tapered roller bearing currently in use in freight railcar

service has three crucial subcomponents: the outer ring (cup), the inner ring (cone), and the rollers. These parts enable tapered roller bearings to operate at high speeds and under heavy cargo loads while maintaining minimal friction during motion. Tapered roller bearings are mounted at the end of wheelsets, as shown in Figure 1, supporting the load of the railcar and cargo.

The exploded view in Figure 2 illustrates the multiple subcomponents of a tapered roller bearing. There are two cones (inner rings), each containing 23 rollers, held by a cage that separates them and prevents misalignment during operation. The spacer ring maintains proper clearance between the cones to prevent axial movement. The grease seal, located at the end of the cup, encloses the cone and prevents grease from leaking. Wear rings are the final subcomponent; they absorb load forces and prevent metal-to-metal contact between rotating and stationary parts. The grease seals and the wear rings also help keep debris and other contaminants from entering the bearing. When a railcar tapered roller bearing is mounted onto a wheelset, the components closest to the end cap are referred to as the outboard (OB) side, whereas those away from the end cap are the inboard (IB) side.

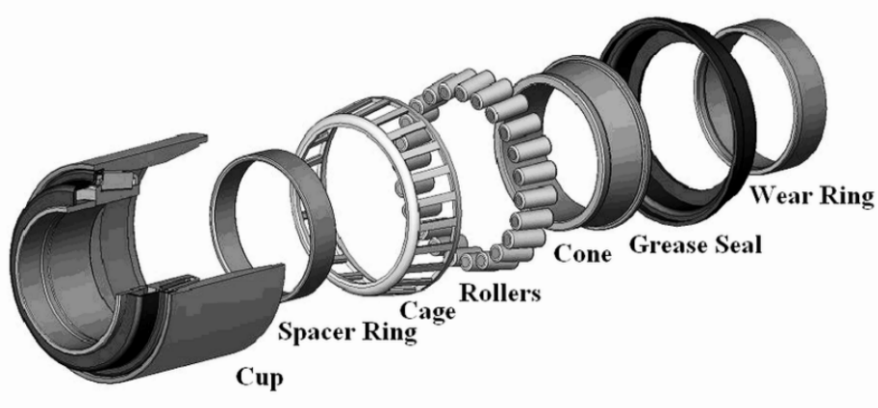

Figure 2. Subcomponents of a tapered roller bearing [2]

Railroad freight railcar bearings are classified by their dimensions and load capacities. The two most commonly used in North America are class F and class K bearings, both rated by

the Association of American Railroads (AAR) [2] to carry loads up to 153.0 kN (34.4 kips) per bearing. The research presented in this thesis analyzes the effects of lateral loading on class K bearings, which have been replacing their class F counterpart over the past two decades. Table 1 lists the different bearing classes and their load capacities

Table 1. Bearing Classes and Bearing Specifications [2]

Bearing Class	Cup Dimension Diameter × Width [inch]	Cup Dimension Diameter × Width [cm]	Bearing Load [kN] / [kips]
E	6 × 11	15.24 × 11.94	117.0/26.3
F	6 ½ × 12	16.51 × 30.48	153.0/34.4
G	7 × 12	17.78 × 30.48	169.0/38.0
K	6 ½ × 9	16.51 × 22.86	153.0/34.4

1.2.1 Types of Defects

Bearing defects are generally caused by one or more of the following three factors: rolling contact fatigue (RCF), lubricant contamination, and geometric out-of-tolerance conditions. RCF can cause microcracks to develop, which can propagate during operation, leading to surface spalling [3][4]. Spalls release metallic debris, increasing wear and further degrading the performance of components with rolling raceways [5] leading to increased temperatures and accelerated lubricant breakdown. A localized RCF defect characterized by spalling and pitting on a bearing cone (inner ring) is depicted in Figure 3.

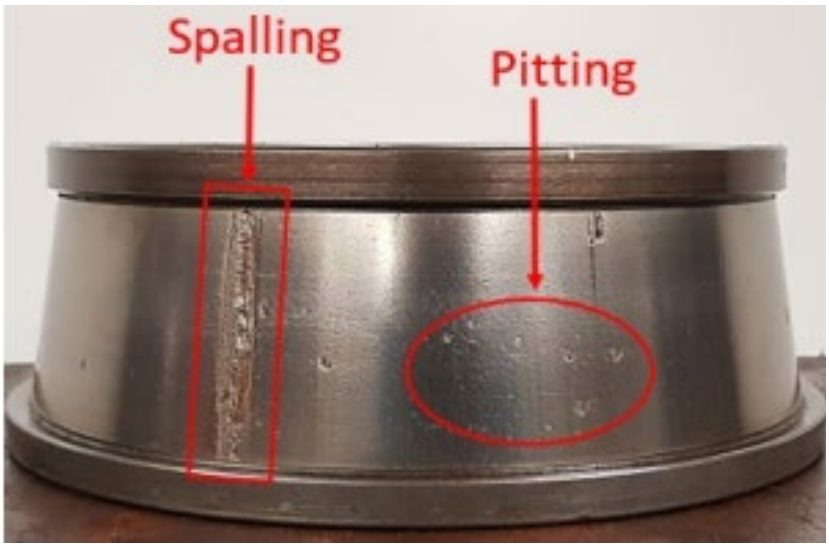

Figure 3. Fatigue spalling and pitting on a cone raceway of a tapered roller bearing [3]

Lubricant contamination most commonly occurs when moisture mixes with the bearing grease. This form of contamination, often referred to as water-etching, is frequently observed in field applications. Moisture interaction with the grease causes lubricant degradation and leads to raceway corrosion. As a result, etch marks appear along the raceways. Under continuous operation, this type of defect can propagate, accelerating bearing degradation. Figure 4 shows water-etch damage on a cone raceway.

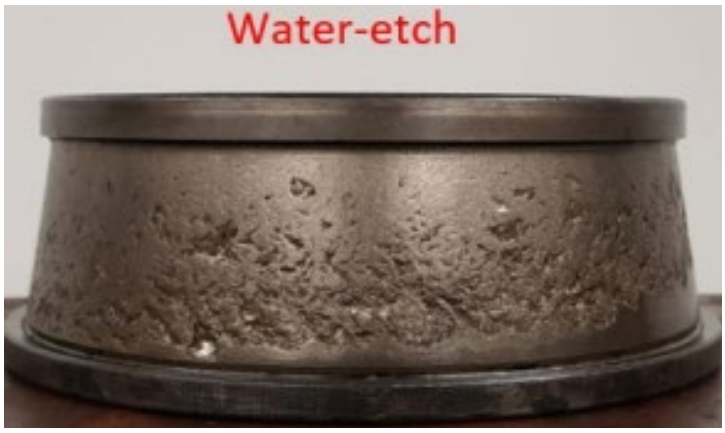

Figure 4. Water-etch damage on a cone raceway of a tapered roller bearing [3]

A geometric defect refers to components with manufacturing errors that fall outside the tolerance of a part's dimensions. Examples of geometric defects include out-of-round raceways, poor concentricity, and non-uniform diameters. Geometric defects cause roller misalignment and

abnormal stress distributions. If left unchecked, the defects may cause a bearing to seize, leading to derailment.

1.3 Wayside Technologies Systems

According to data from the Federal Railroad Administration (FRA), defective bearings and wheels are consistently among the leading mechanical causes of rail derailments in the United States [6]. As such, wayside technology systems have been deployed throughout North America to identify defective bearings and wheels during operation. These systems are integrated with the rail tracks in designated locations and will alert rail operators if a bearing or wheel is operating above an established threshold. Each time a railcar passes a wayside system, data is collected and analyzed. The measured parameters are compared against established thresholds to identify abnormal behavior or early signs of failure. There are three systems commonly used in the rail industry: the Hot Bearing (or Box) Detectors (HBDs) and Acoustic Bearing Detectors (ABDs) that assess bearing health and the Wheel Impact Load Detectors (WILDs) that evaluate wheel health.

1.3.1 Hot Bearing Detectors (HBDs)

An HBD, shown in Figure 5, uses infrared sensors to measure the bearing and wheel temperatures. The AAR suggested temperature threshold is set to trigger an alarm for train operators if the bearing operating temperature exceeds 94.4°C (170°F) above ambient or 52.8°C (95°F) above the temperature of the bearing on the opposite side of the axle. Over 6,000 HBDs have been installed on U.S. railways, with spacing ranging from 24 to 48 km (15 to 30 mi) [7]. However, HBDs can be spaced up to 64 km (40 mi) in areas with lower population density [8]. The spacing between HBDs limits their effectiveness, as a bearing may fail while traveling between successive detector locations. In the 2023 East Palestine, Ohio, derailment, an

investigation determined that the railcar traveled about 42 km (26 mi) with a bearing “on fire” while passing through three HBDs, the last of which sent a signal to the locomotive cab to stop [9]. After the derailment, 1,000 new units were installed on tracks to be able to detect failing bearings sooner [10].

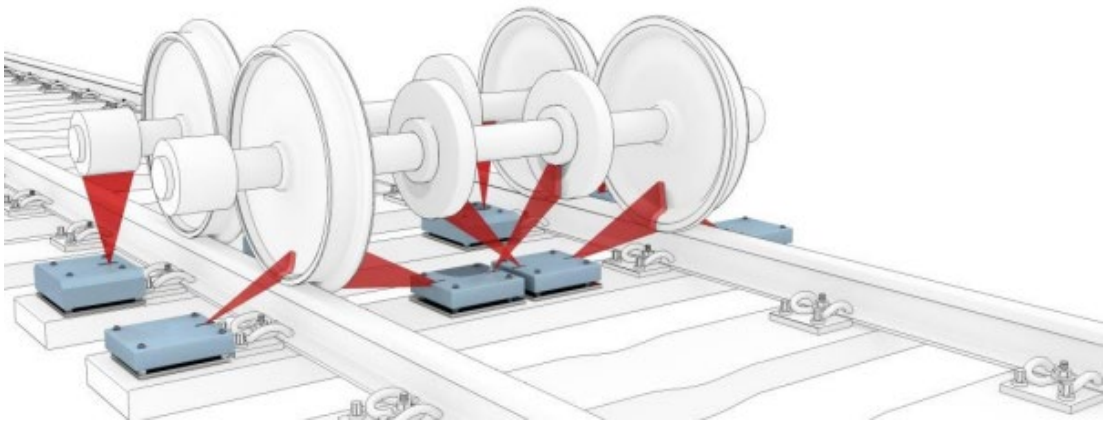

Figure 5. Hot Bearing Detector (HBD) [11]

Bearings exceeding temperature thresholds are removed from service and inspected; if no defects are found upon inspection, they are classified as “non-verified” [12]. At the University Transportation Center for Railway Safety (UTCRS), researchers have concluded that defective bearings can operate at temperatures below those of healthy (defect-free) bearings [13]; therefore, temperature inspection is only informative once wear has reached a significant level. HBDs excel at detecting end-of-life bearings when major raceway degradation has already occurred. As a result, HBDs are considered reactionary and cannot provide proactive maintenance recommendations based on historical bearing temperature performance.

1.3.2 Trackside Acoustic Detection Systems (TADS™)

Trackside Acoustic Detection Systems (TADS™) are an example of an ABD that uses microphones to detect acoustic signatures during bearing operation, as pictured in Figure 6. The system uses sound to determine the condition of the bearings and wheels as they pass through the detectors. TADS™ detect bearings known as “growlers,” which contain defects spanning the

majority of the raceways. Unfortunately, only 19 systems have been installed on North American railways, meaning that some trains may never cross one of these systems throughout the life of their bearings [14].

Figure 6. Trackside Acoustic Detection System (TADS™) site [15]

1.3.3 RailBAM (Rail Bearing Acoustic Monitor)

RailBAM (Rail Bearing Acoustic Monitor), pictured in Figure 7, uses tie-mounted auxiliary sensors and a signal-processing electronics rack located in a wayside enclosure. Similar to TADS™, RailBAM uses microphones to assess the condition and severity of bearing defects; it can detect early signs of defects with 95% reliability. There are 20 RailBAMs installed throughout North America as of 2017 [16].


Figure 7. RailBAM (Rail Bearing Acoustic Monitor) site [16]

1.4 Effects of Lateral Loading on Wheelset Bearing

Given the known capabilities and limitations of existing wayside monitoring technologies, it is important to examine how lateral loading directly affects wheelset bearings, as these forces can influence the conditions these systems aim to detect. Lateral loading refers to horizontal forces that act sideways – perpendicular to the tracks – on a wheelset's axle bearings. These forces are present during curve negotiation, alignment deviations, and track-induced excitation. The lateral-to-vertical ratio (L/V) characterizes the wheel-rail interaction between the static vertical wheel load and the dynamic lateral forces transmitted through the bogie. The L/V ratio is influenced by multiple operational and track-related factors, such as a reduced curve radius, increased track stiffness, increased speed, which leads to hunting behavior, and inadequate yaw damping of the impact ring. These factors increase lateral forces and, in turn, raise the L/V ratio.

In North American freight rail, L/V ratios ranging from ~1.25 to 1.5 are associated with an increased risk of flange climb derailment [17][18]; here, the wheel's flange – the inner protruding rim – literally "climbs" up the side of the rail instead of staying on the track. When negotiating a curve, railcars experience increased lateral loading on the wheelset. Excessive lateral forces relative to the vertical load may lead to the loss of wheel-rail contact. Safe operating L/V limits are typically higher for unloaded railcar conditions than for fully loaded conditions due to the reduced vertical load. For continued operation, FRA considers an L/V value below 0.8 acceptable under both loaded and unloaded conditions. Table 2 summarizes safe L/V ratio ranges based on loading conditions and lists the recommended FRA threshold [17].

Table 2. L/V safe operating ranges [16][17]

Condition	Vertical Load (Relative)	L/V
Unloaded	Low	0.6-0.8
Fully Loaded	High	0.3-0.5
FRA Practice	Threshold	0.8

1.5 Motivation

The work presented in this thesis focuses on a railcar bearing's response under lateral loading for both healthy and defective bearing states. Studies have investigated the effects on wheelsets during curve negotiation; however, publicly available research specifically focused on bearing behavior remains limited. By identifying and analyzing the effects exhibited by bearings during curve negotiation in both healthy (defect-free) and defective states, this research provides new insight into the internal behavior of bearing components under operation. The findings from this study may also support the railway industry in developing improved bearing designs and advancing condition-monitoring technologies that more effectively assess bearing health during in-service operation. The research presented centers on the development of a laboratory test fixture capable of replicating the lateral loading conditions experienced by a bearing during railway operation when negotiating a curve or under significant railcar hunting behavior.

This thesis is organized as follows: Chapter II introduces the governing equations in the mechanics of lateral loading of a bearing. Chapter III describes the experimental methods employed to collect data. The results and discussion of data collected from a healthy (defect-free) bearing and a defective bearing are presented in Chapters IV and V, respectively. Conclusions and recommendations for future research are discussed in Chapter VI.

CHAPTER II

MECHANICS OF LATERAL LOADING

2.1 Mechanics of Lateral Loading

When a freight railcar is in motion, the wheelsets and bogie assemblies are subjected to a combination of vertical, lateral, and longitudinal forces that are ultimately transmitted through the axle bearings. These forces arise from wheel-rail contact mechanics and vehicle-track dynamic interactions. As a train negotiates a curve, the railcar mass experiences a centrifugal acceleration, producing an outward lateral force on the vehicle body and wheelsets. The forces produced, commonly referred to as creep forces, modify the contact conditions at the wheel-rail interface increasing the tangential forces transmitted through the contact patch.

Creep force is defined as the tangential force generated at the wheel-rail contact patch due to small relative slip, or creepage, between the rolling surfaces. Even though the wheel normally rolls without sliding, elastic deformation between the wheel and rail produces a localized micro-slip that generates tangential forces acting in both the lateral and longitudinal directions of the contact patch. During curve negotiation, the outward centrifugal loading increases the lateral component of the creep force, which contributes to higher lateral loads within the wheelset and associated components, including the axle bearings, as illustrated in Figure 8.

In addition to the creep forces developed at the contact patch, curve negotiation also generates flange forces when the wheel flange contacts the gauge face of the rail. The flange force acts as a reaction force opposing the outward motion of the wheelset and is required to

maintain the wheelset within the track gauge. From a mechanics standpoint, this interaction is consistent with Newton's Third Law of Motion where the lateral force exerted by the wheel on the rail is counteracted by an equal and opposite reaction force from the rail on the wheel. The magnitudes of both creep and flange forces are influenced by operation and track parameters, including train speed, curve radius, vehicle loading, wheel-rail friction conditions, suspension stiffness, and track structural stiffness. In general, higher speeds and tighter curve radii increase centrifugal loading, thereby amplifying lateral forces transmitted through the wheelset and bogie. Furthermore, insufficient yaw damping or increased track stiffness can intensify the lateral forces by reducing the system's ability to dissipate dynamic energy.

Hunting is a dynamic phenomenon in which the wheelset sways or "snakes" from side to side at high speeds, influencing the lateral forces transmitted. The self-excited lateral oscillation of the wheelsets and bogie arises from the coupled interaction between wheel conicity, suspension characteristics, and track conditions, which together create an unstable lateral motion of the wheelsets relative to the track centerline [19]. The hunting motion significantly amplifies lateral forces at the wheel-rail interface, thereby increasing the loads transmitted through the axle bearings.

Although multiple force mechanisms act simultaneously within the wheel-rail-bogie system, the present study focuses specifically on the influence of sustained lateral creep forces that develop during curving conditions. Understanding how these lateral loads propagate through the wheelset and influence bearing behavior is critical for evaluating their impact on bearing temperature, vibration response, and long-term reliability.

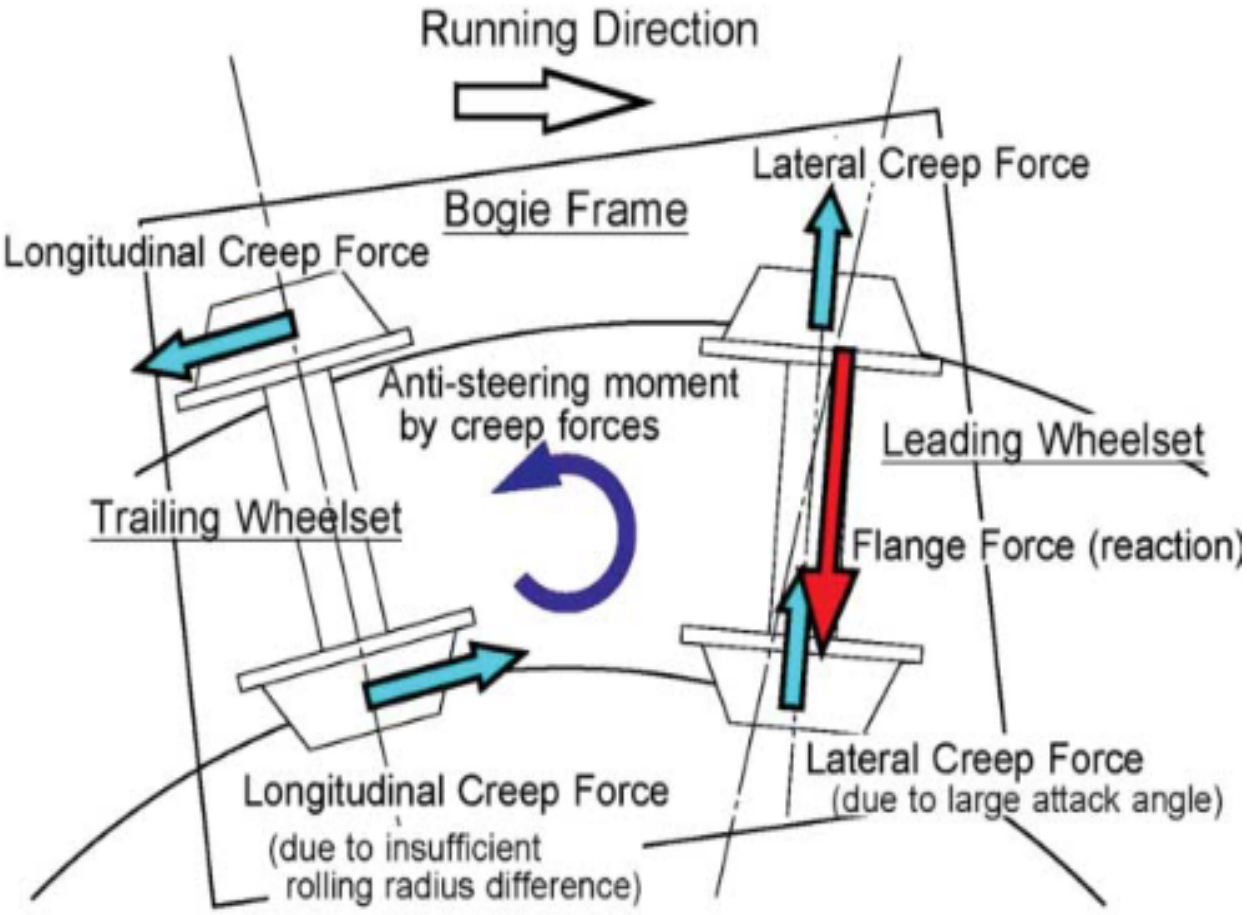

Figure 8. Centrifugal effects on wheelsets in curves [21]

2.1.1 Calculating Radius of a Curve

Equation (1) correlates the curve radius, *R*, to the degree of curvature, *D*. The rail industry defines curvature using the 100-ft chord, where the degree of curvature corresponds to the central angle formed by a 30.5m (100 ft) chord along a circular track alignment, as demonstrated in Figure 9. As an example, the radius for a 30.5m (100 ft) chord and a 1º curve is approximately 1,746.5 m (5,730 ft) [21].

$$R = \frac{5{,}730\ ft}{D} \tag{1}$$

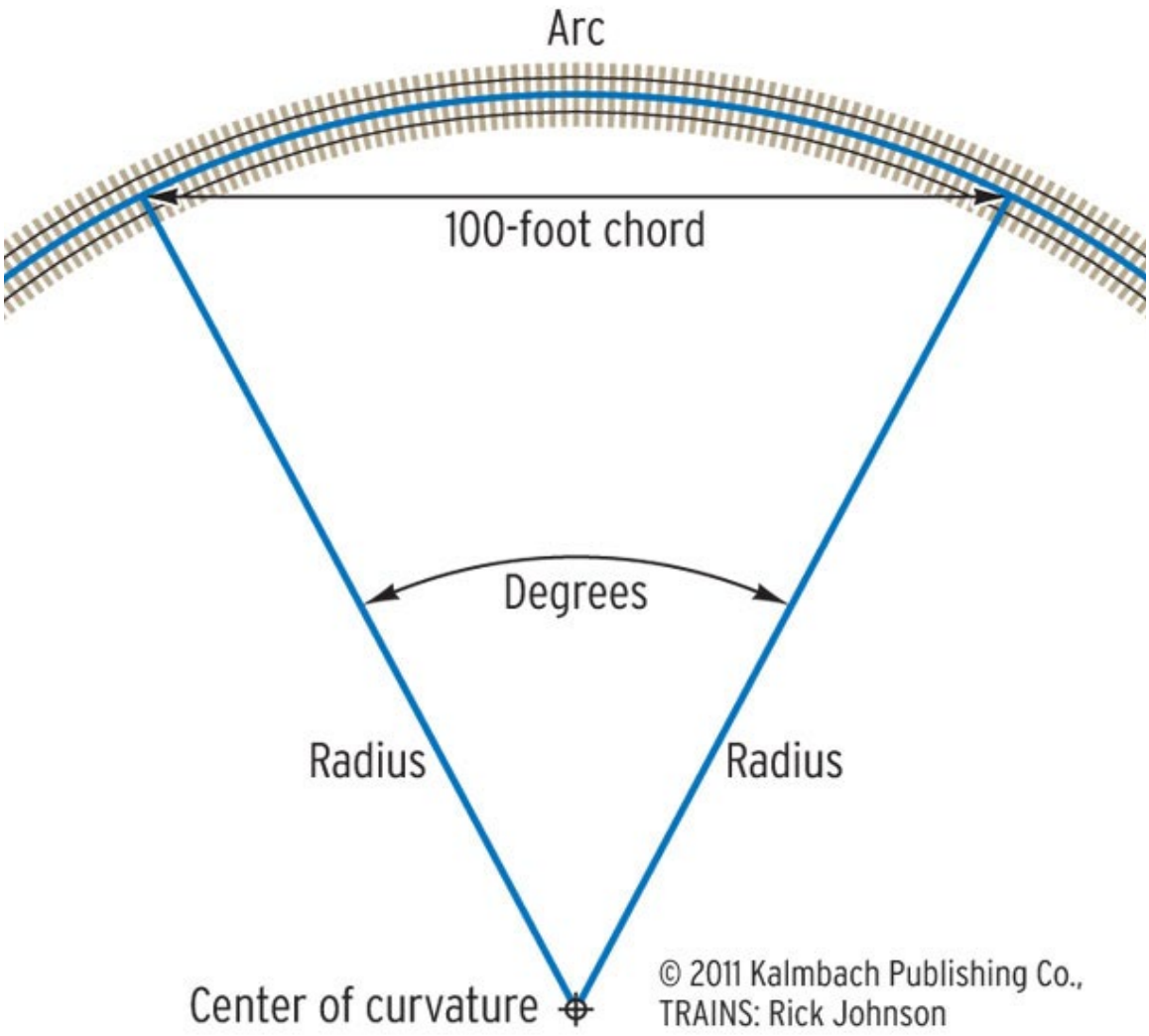

Figure 9. 1° curve based on a 100-ft chord [22]

Equation (1) was derived from the relationship between the chord length, radius, and central angle $C = 2R\sin(D/2)$; by substituting the chord length, it converts to $R = 50/\sin(D/2)$, resulting in a 1° curve approximating the previously stated 1,746.5 m (5,730 ft) radius. The degree of curvature and the radius are inversely proportional. A higher degree means a sharper, tighter curve, while a lower radius indicates the center of the circle is closer to the track. Table 3 lists curve degrees from real tracks in operation and their corresponding radii calculated using Equation (1). The 2.4-12-degree curves are used by MxV Rail, located in Pueblo, Colorado, which operates trains at speeds ranging from 16 to 113 kph (10 to 70 mph)

[23]. The 8-10-degree curves are found on the track at the Tehachapi Loop in Tehachapi Pass, in South Central California [24].

Table 3. Degree of Curve to Radius

Degree of Curve	Radius [ft]	Radius [m]
1.0º	5,730	1746.5
2.4º	2,387	727.6
5.5º	1,042	317.6
5.8º	988	301.1
10.3º	556	169.5
10.7º	535	163.1
10.8º	531	161.8
12.0º	477	145.4
16.0º	358	109.1

2.1.2 Calculating Lateral Loading

During a curve negotiation, centrifugal forces act on the bogie mass, generating a lateral load. Lateral forces are calculated using [25][26]

$$F_{lat} = \frac{\left(\frac{W}{g}\right) * V^2}{R} \tag{2}$$

where F_{lat} is the lateral force, W is the gross weight, g is the acceleration due to gravity, V is the velocity, and R is the curve radius. Equation (2) assumes steady-state curving conditions and neglects transient effects such as track irregularities and vehicle hunting. When calculating the total railcar mass, the wheelset weight must be included. The total weight of a fully loaded railcar (100% load) is about 1272 kN (286 kips), and that of an unloaded railcar is about 249 kN (56 kips), which is equivalent to approximately 17% of a full railcar load. Depending on operating conditions, a small curve radius can produce high lateral forces on the train. Because

this study focuses on a single tapered roller bearing, calculations are performed only for that bearing, as the applied lateral load acts exclusively on it. Tables 4 and 5 present calculation results for a curve with a radius of 956 ft (6° curve).

Table 4. F_{lat} for 100% load at R = 956 ft (6° curve)

Speed	**Lateral Load (F_{lat})**	**L/V**
234 RPM (40 kph or 25 mph)	1.5 kips / 6.7 kN	0.04
420 RPM (72 kph or 45 mph)	5 kips / 22.2 kN	0.14
560 RPM (96.6 kph or 60 mph)	9 kips / 40 kN	0.25

Table 5. F_{Lat} for 17% load at R=956 ft (6° curve)

Speed	**Lateral Load (F_{lat})**	**L/V**
234 RPM (40 kph or 25 mph)	0.3 kips / 1.3 kN	0.04
420 RPM (72 kph or 45 mph)	1 kips / 4.5 kN	0.14
560 RPM (96.6 kph or 60 mph)	1.7 kips / 7.5 kN	0.25

CHAPTER III

EXPERIMENTAL METHODS

To evaluate the effects of lateral loading on a tapered roller bearing, a structural frame was designed and integrated into the UTCRS Single-Bearing Tester (SBT). The system applies a controlled lateral force on a bearing adapter that is representative of the forces experienced by a freight car during curving events. To support simultaneous radial and lateral loading, a linear bearing assembly was engineered to allow controlled translational motion of the bearing adapter during the lateral force application. Primary structural components were analyzed using finite element analysis (FEA) to ensure that the modified system could safely withstand the applied loads without excessive stress or deformation. The results of the analyses can be viewed in APPENDIX A.

3.1 Single-Bearing Tester (SBT)

The UTCRS SBT, pictured in Figure 10, reproduces the loading and operating conditions experienced by freight railcar bearings in rail revenue service. The tester applies a radial load to the bearing in a cantilever configuration, replicating the load path observed during field operation. The test axle is supported by two spherical-roller pillow-block bearings. The SBT simulates both fully loaded (100% load, 153 kN or 34.4 kips per bearing) and unloaded (17% load, 26 kN or 5.8 kips per bearing) railcar conditions. A belt-and-pulley system drives the test axle with a 22 kW (30 hp) variable-frequency motor at rotational speeds corresponding to train traveling speeds up to 137 kph (85 mph).

Two hydraulic-driven frame assemblies were employed to simulate lateral forces associated with curve negotiation. A front ram frame, shown in Figure 11, was engineered to apply a lateral force directly to the bearing adapter using an 8.26 cm (3.25 in) hydraulic cylinder connected to an ENERPAC P462 two-stage, 10,000 psi hand pump. Structural analysis confirmed that the assembly could safely apply lateral loads of up to 15 kips (see APPENDIX A). A rear ram frame applies an opposing load at the center of the rotating axle, as shown in Figure 12. The rear ram incorporates a bearing interface that transmits load while the axle rotates, thereby counteracting the forces induced by the front ram and maintaining mechanical equilibrium in the system. Detailed FEA results for both loading assemblies are provided in APPENDIX A.

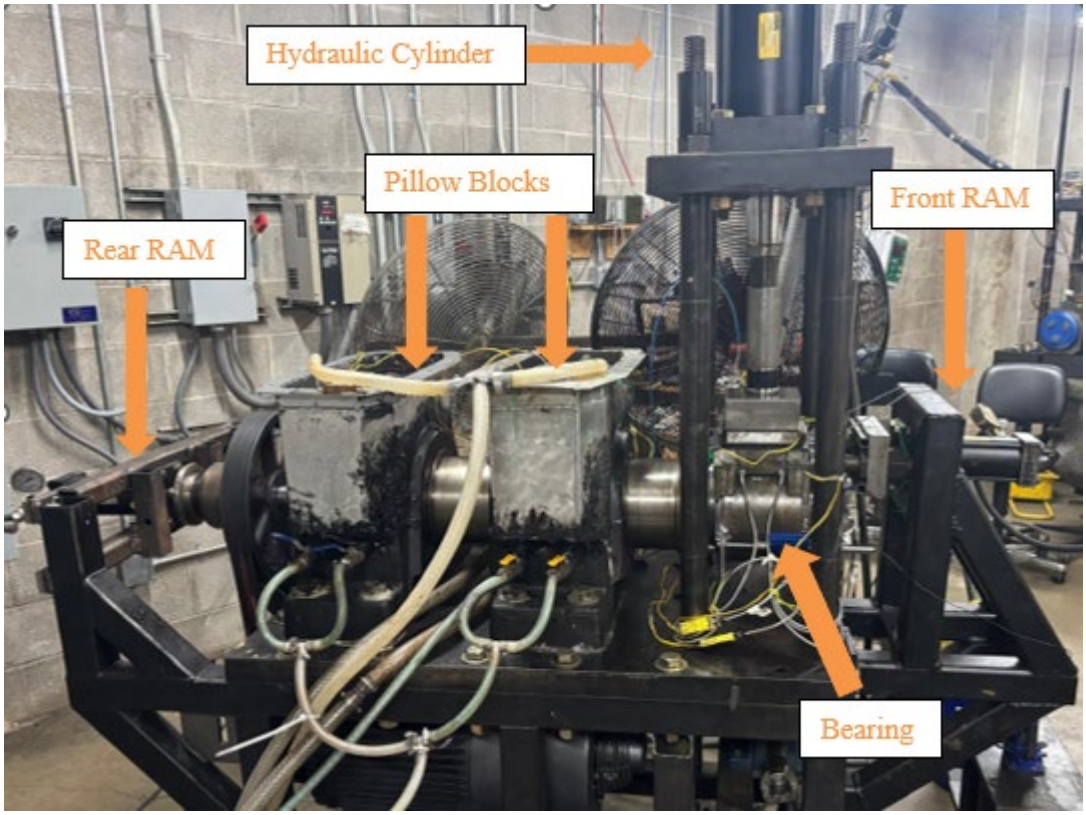

Figure 10. Single-Bearing Tester (SBT) laboratory setup with bearing, front ram, rear ram, and hydraulic cylinder.

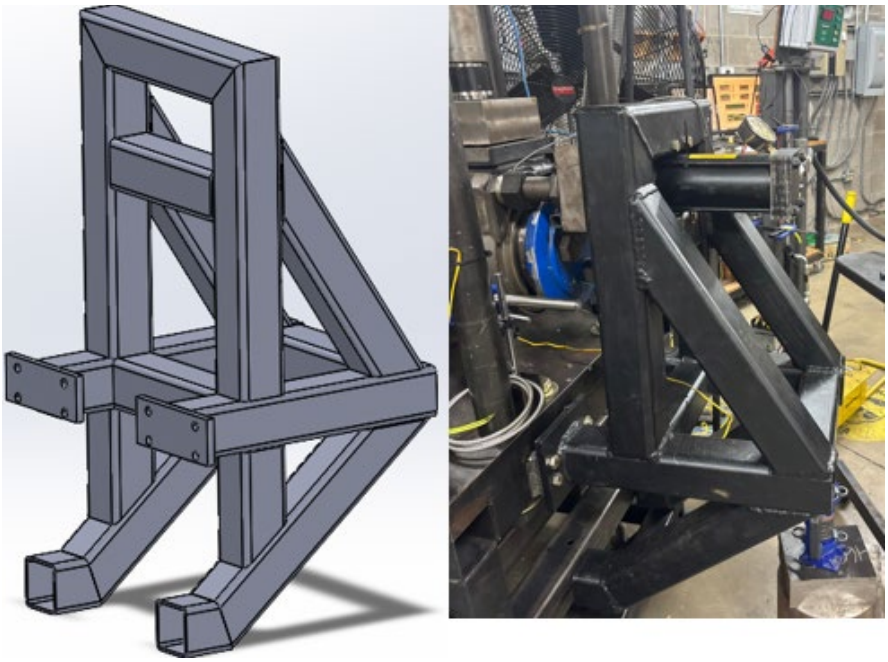

Figure 11. Front ram computer-aided design (CAD) assembly (left) and experimental assembly (right)

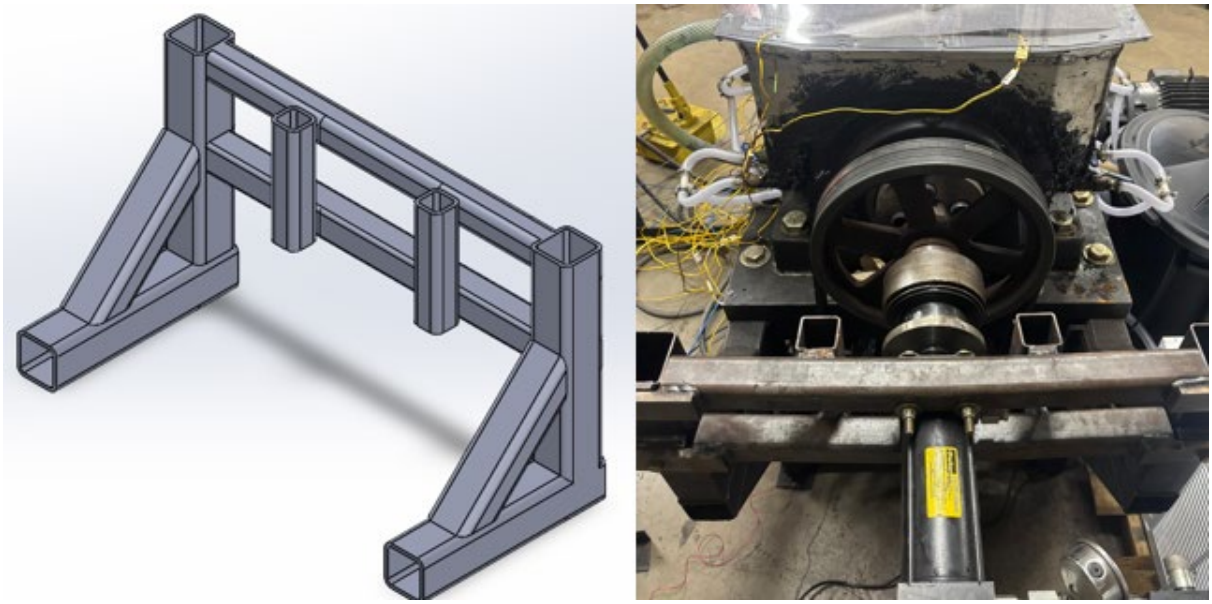

Figure 12. Rear ram CAD assembly (left) and experimental assembly (right)

3.2 Linear Bearing Assembly

A custom linear bearing assembly was designed to enable controlled translational motion of the bearing adapter under lateral loading, as shown in Figure 13. The linear bearing assembly is seated above the bearing adapter and supports the load of a fully loaded railcar while allowing

lateral motion. By allowing the bearing adapter to move sideways, the assembly prevents bending moments from developing in the upper hydraulic loading system that would otherwise occur if lateral forces were applied to a rigidly constrained adapter. The linear bearings ensure that the applied load is transmitted primarily as a lateral force.

The assembly consists of three cylindrical rollers, each with a diameter of 3.81 cm (1.5 in) and a length of 12.27 cm (4.83 in), housed within a machined A36-steel casing measuring 15.24 cm × 15.24 cm × 6.35 cm (6 in × 6 in × 2.5 in). For the structural analysis, the allowable weight, W_{allow}, per unit length, was calculated using

$$W_{allow} = \frac{\sigma_y}{F.S.} * d * \frac{1}{8} \tag{3}$$

where σ_y is the yield strength, $F.S.$ is the factor of safety, and d is the distance constant. Given a yield strength of 2.07 GPa (300,000 lb/in^2) and a factor of safety of 2, the resulting allowable weight per unit length was 49.25 kN/cm (28,125 lbf/in). The reaction force equation

$$R_i = a_i * W_{allow} * L \tag{4}$$

was derived by applying distribution coefficients to a specific load case for the roller segment with a given length spacing, L, of 4.14 cm (1.63 in). In Equation (4), $i = 1$, 2, and 3 correspond to the three reaction forces calculated as R_1, R_2, and R_3, and a_i are coefficients determined by beam spacing with values of 0.375, 1.25, and 0.375, respectively. The outer supports, R_1 and R_3, had reaction forces of 76.5 kN (17,191 lbf) while the central support, R_2, was calculated to be 254.9 kN (57,304 lbf). The maximum bending stress seen by the assembly was then calculated using

$$\sigma_{max} = \frac{M_{max}\, c}{I} \tag{5}$$

where M_{max} is the maximum bending moment, c is the maximum distance away from the neutral axis, and I is the moment of inertia. The area moment of inertia had a value of 27.89 cm^4 (0.67 in^4) and was calculated using $I = bh^3/12$, for a rectangular cross-section with a base, b, of 15.24 cm (6 in) and a height, h, of 2.80 cm (1.1 in). The maximum bending moment

$$M_{max} = \left(\frac{1}{8}\right) * W_{allow} * L^2 \quad (6)$$

had a value of 1.1 kN·m (9,341 lbf·in) with a resulting maximum bending stress, σ_{max}, of 290.32 MPa (42,107 psi).

The rollers were manufactured from AISI 52100 annealed bearing steel. In order to attain the required hardness and strength, the roller bearings were heat-treated by austenitizing at 1040°C (1904ºF) for 30 minutes to dissolve carbides, followed by oil quenching and tempering for one hour at 840°C (1544ºF) [27]. Finite element (FE) analysis confirmed that the assembly could safely sustain the maximum vertical load during testing. Refer to APPENDIX A for the FE analysis results.

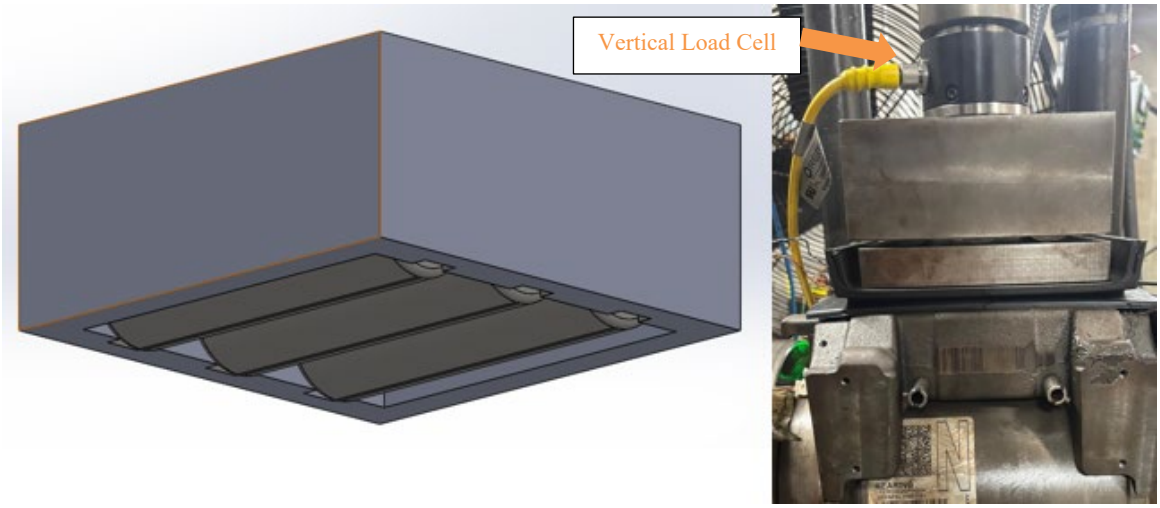

Figure 13. (left) CAD figure of the linear bearing assembly and (right) linear bearing assembly and vertical load cell on laboratory tester setup

3.3 Instrumentation and Data Acquisition

Vibration measurements were obtained using two uniaxial microelectromechanical system (MEMS) accelerometers with a measurement range of ±100 g. The accelerometers were mounted on the inboard top (IBT) and the inboard mote (IBM) locations of the bearing adapter, as pictured in Figure 14. Each sensor was installed on a 3D-printed mounting base, which was attached to a machined railway adapter. Vibration data were collected at a sampling frequency of 5.12 kHz for 16 seconds at 10-minute intervals using a National Instruments (NI) cDAQ-9174 chassis utilizing two NI-9205 modules and one NI-9213 module via NI LabVIEW software.

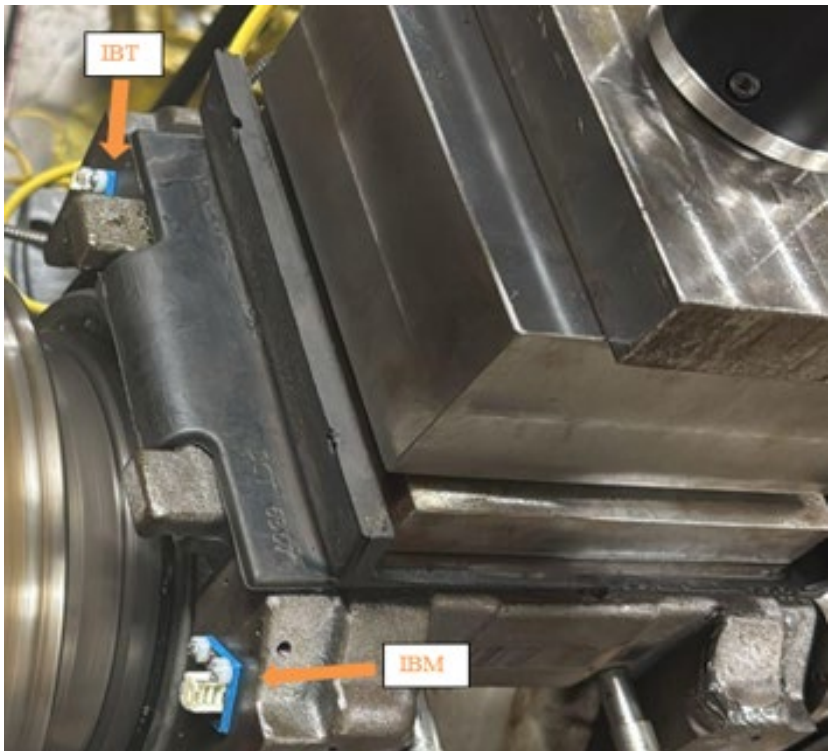

Figure 14. Inboard top (IBT) and inboard mote (IBM) accelerometer locations

Bearing operating temperature was measured using bayonet-style K-type thermocouples affixed to the bearing adapter, as pictured in Figure 15. Specifically, the bearing operating temperature at the inboard and outboard sides of the bearing was obtained by averaging the readings from the two thermocouples that recorded the temperature of the bearing cup at the

inboard and outboard raceways at the two sides of the bearing adapter. Load measurements were obtained using three load cells: one vertical load cell, shown in Figure 13, and two lateral load cells positioned to contact the face of the bearing adapter, depicted in Figure 16.

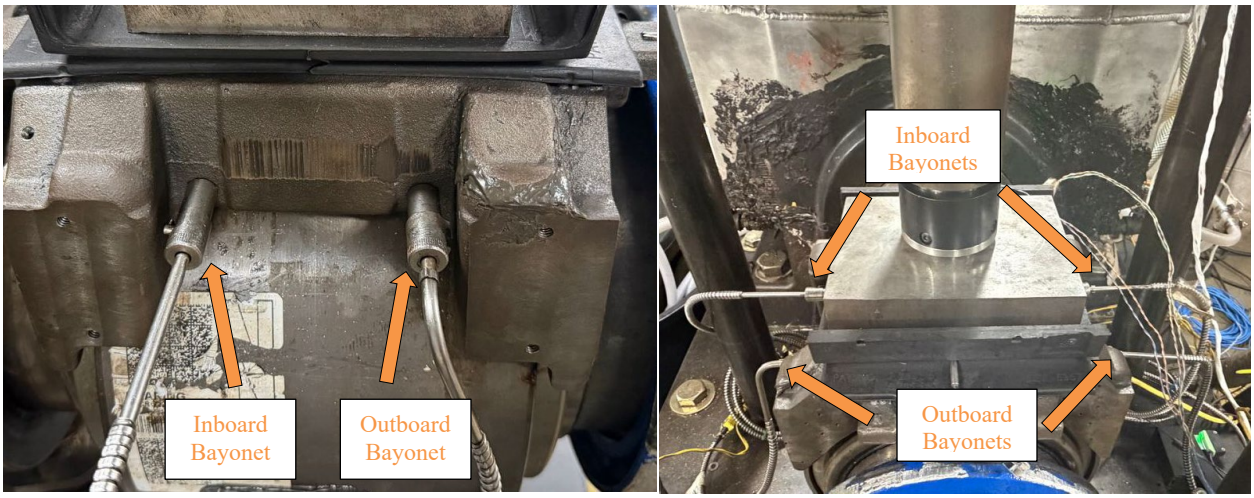

Figure 15. Bayonet-style-K-type thermocouples affixed to the bearing adapter and locations

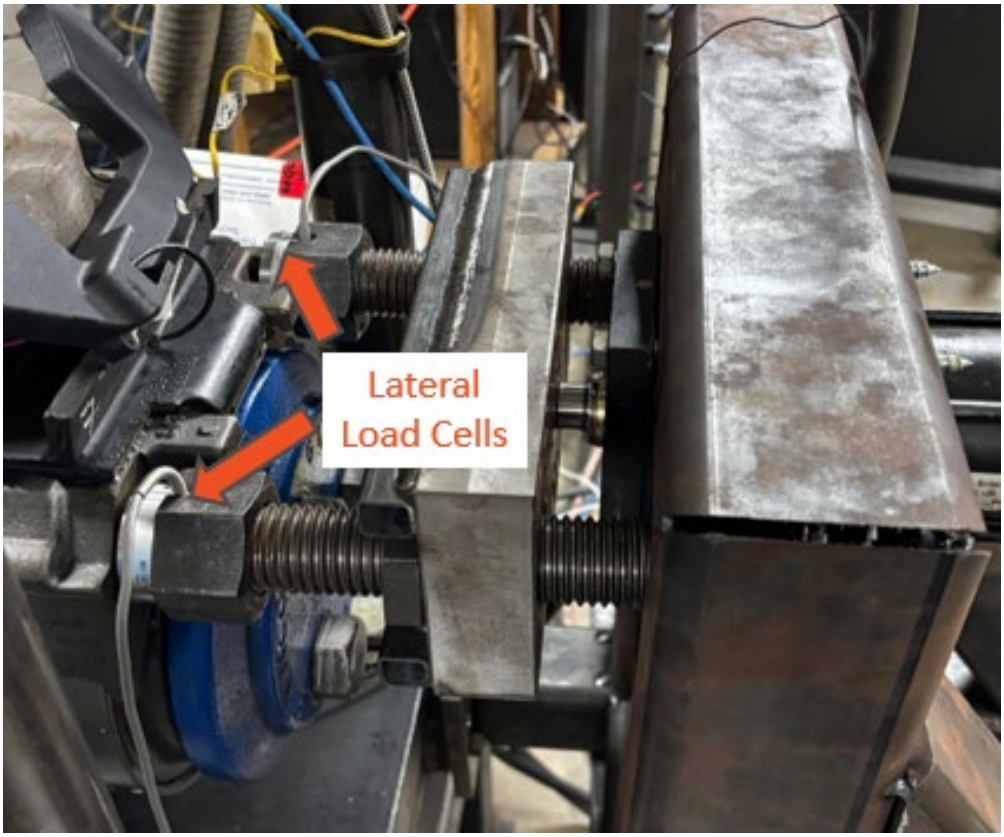

Figure 16. Lateral load cells on the bearing adapter

The displacement of the bearing under lateral loading was measured using a Linear Variable Differential Transformer (LVDT) with a linearity error of ±0.2% of full-scale output (FSO), corresponding to ±0.102 mm (±0.004 in). The LVDT was mounted on a magnetic base placed on the SBT frame. A fixed plate attached to the inboard side of the bearing served as the reference for the measured displacement, as shown in Figure 17.

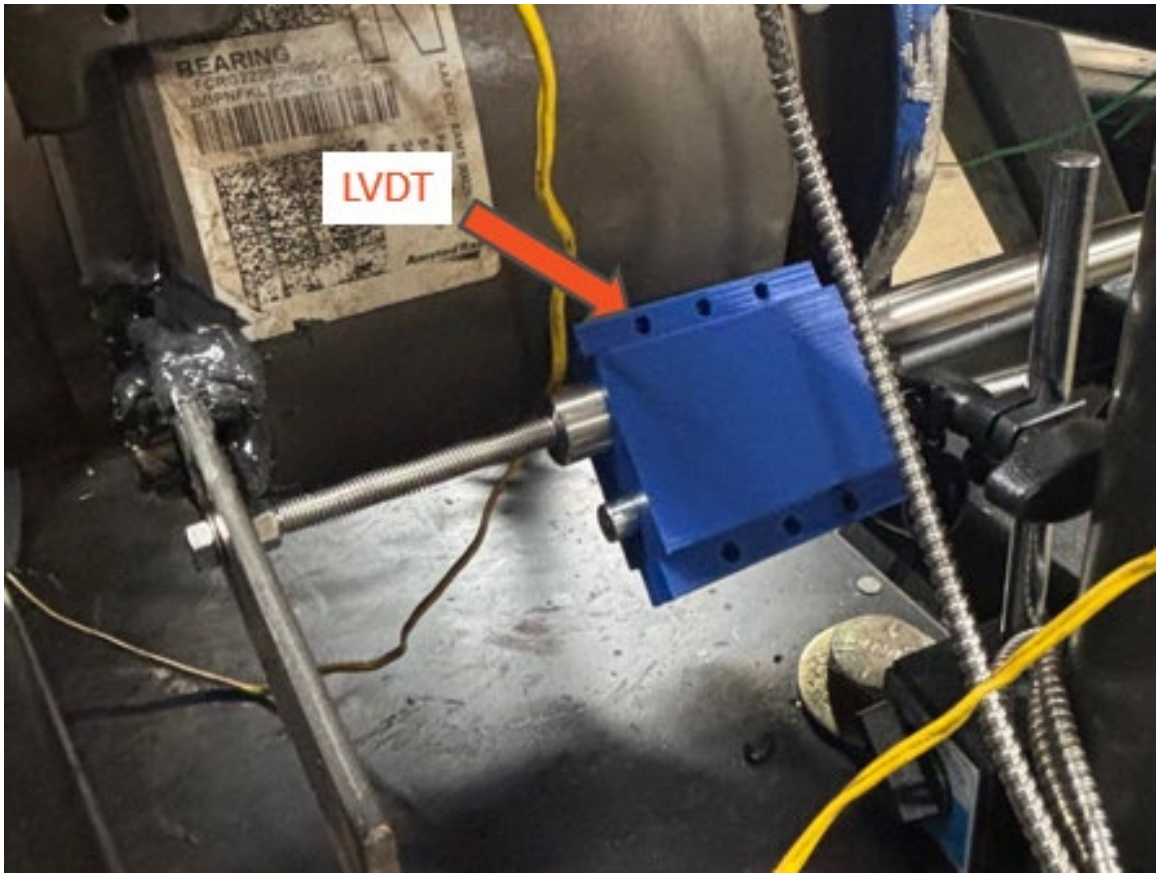

Figure 17. Linear Variable Differential Transformer (LVDT) device used to measure the lateral displacement of the bearing

Motor power and rotational speed were monitored and controlled using a variable frequency drive (VFD), enabling consistent test conditions and continuous monitoring of system performance throughout the experiments.

3.4 Experimental Conditions and Procedures

Experiments were conducted under two vertical load conditions: an unloaded railcar (17% of full load equivalent to 26.0 kN or 5.85 kips per bearing) and a fully loaded railcar (100% of full load equivalent to 153.0 kN or 34.4 kips per bearing). For each load case, testing was performed at three rotational speeds representative of train operating speeds: 234 rpm (simulating 40 kph or 25 mph), 420 rpm (simulating 72 kph or 45 mph), and 560 rpm (simulating 97 kph or 60 mph). To assess the influence of lateral loading on damaged bearing components, two bearing conditions were evaluated during testing: a healthy control bearing cup (Exp. 305) and a defective bearing containing a cup spall (Exp. 296B).

Table 6 and Table 7 summarize the lateral loading cases evaluated for the control (nominal/healthy) and defective bearing, respectively. Each test began with no lateral load applied (L/V = 0) to establish baseline conditions. At high speeds and full loads, the lateral load was raised incrementally using ~19.1 kN (4.3 kip) steps to maintain specific L/V ratios. At lower speeds and unloaded conditions, the increments ranged from 1.8 kN (0.4 kips) to 5.3 kN (1.2 kips). During testing, the lateral load was periodically removed (L/V = 0) to verify measurement repeatability and system stability.

The tables present operating speed, applied vertical load, and equivalent track curvature to evaluate multiple loaded and unloaded case scenarios. The L/V ratio is provided to quantify the severity of each condition. These loading conditions encompass both typical operational scenarios and more severe curve-negotiation instances to assess the effects of lateral loading on the bearing temperature and vibration response.

Table 6. Control bearing lateral load cases examined

Speed [kph]	Speed [mph]	Speed [ft/s]	Load [%]	Degree of Curve	Radius [m]	Radius [ft]	F_{lat} [kN]	F_{lat} [kips]	L/V
97	60	88	100	9.0°	195	640	60.1	13.50	0.38
97	60	88	100	6.0°	291	956	40.0	9.00	0.25
97	60	88	100	3.0°	564	1850	20.0	4.50	0.12
97	60	88	17	11.7°	149	490	15.4	3.45	0.50
97	60	88	17	7.6°	230	754	9.9	2.23	0.34
72	45	66	100	16.0°	110	360	59.2	13.30	0.37
72	45	66	100	10.7°	162	530	40.0	9.00	0.25
72	45	66	100	5.5°	317	1040	20.5	4.60	0.13
72	45	66	100	5.8°	299	980	22.2	5.00	0.14
72	45	66	17	16.3°	107	350	12.0	2.70	0.39
72	45	66	17	10.4°	168	550	7.6	1.70	0.24
40	25	37	100	10.8°	162	530	10.7	2.40	0.06
40	25	37	100	10.4°	168	550	8.0	1.80	0.05

Table 7. Defective bearing lateral load cases examined

Speed [kph]	Speed [mph]	Speed [ft/s]	Load [%]	Degree of Curve	Radius [m]	Radius [ft]	F_{Lat} [kN]	F_{Lat} [kips]	L/V
97	60	88	100	3.0°	594	1950	19.6	4.40	0.12
97	60	88	100	5.7°	305	1000	38.3	8.60	0.24
97	60	88	100	8.7°	199	654	58.3	13.10	0.37
97	60	88	100	6.0°	291	956	40.0	9.00	0.25
97	60	88	17	7.8°	225	738	10.1	2.28	0.32
97	60	88	17	10.5	166	543	13.8	3.10	0.44
72	45	66	100	10.8°	161	528	40.9	9.20	0.26
72	45	66	100	16.0°	109	357	60.1	13.50	0.38
72	45	66	100	10.3°	168	554	38.7	8.70	0.24
72	45	66	17	11.5°	151	496	8.4	1.90	0.27
72	45	66	17	16.3°	107	350	12.0	2.70	0.38
40	25	37	100	10.3°	169	556	7.1	1.60	0.04
40	25	37	100	11.0°	158	520	12.5	2.80	0.08

CHAPTER IV

RESULTS AND DISCUSSION FOR A HEALTHY BEARING

4.1 Experiment 305: Healthy Bearing

This chapter focuses on results obtained from Experiment 305: the evaluation of lateral loading on a control bearing (healthy, non-defective). A healthy, non-defective bearing is defined as having no discernible surface damage or defects on the assembly (including rollers, cup, and cone raceways) prior to testing.

Figure 18 shows the control bearing cup used for this study. Visual inspection confirms that no defects were present on any of the bearing components. The control bearing had a measured unmounted lateral clearance of 0.584-0.660 mm (0.023-0.026 in). The experiments described in this chapter emulate a railcar bearing operating at 72 kph (45 mph) under unloaded and fully loaded conditions at varying L/V ratios. This speed was chosen as a representative case to examine the effects of lateral loading on a railcar bearing; however, additional speeds and scenarios were evaluated, as listed in Table 6. The lateral case scenarios correspond to combinations of operating speeds, vertical applied load, and simulated track curvature that produce specific lateral force magnitudes and lateral-to-vertical load ratios (L/V). Results for all the test scenarios listed in Table 6 are provided in APPENDIX B.

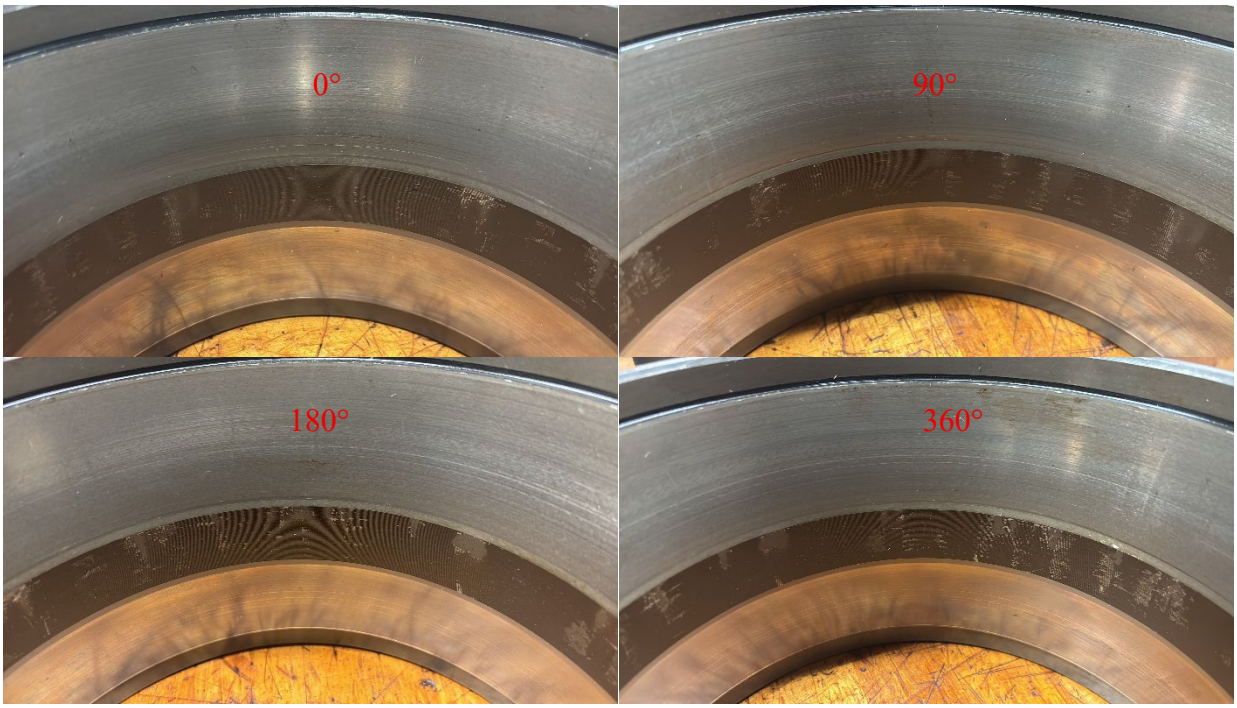

Figure 18. 360° view of the control cup used in Experiment 305

The following sections present the results for Experiment 305 with a control bearing at 72 kph (45 mph) under 17% load (empty railcar) with varying lateral loading to attain L/V ratios of 0.39 and 0.24, and 100% load (fully loaded railcar) with L/V ratios of 0.37, 0.25, 0.13, and 0.14, as listed in Table 6.

4.2 Effects of Lateral Load at 72 kph (45 mph) and Unloaded Railcar

4.2.1 Temperature and Vibration Profiles

At 72 kph (45 mph) for 17% load (empty railcar load), L/V ratios of 0.39 and 0.24 were tested with degrees of curvature of 16.3° and 10.4° and lateral loads of 12.0 kN (2.7 kips) and 7.6 kN (1.7 kips), respectively. The initial operating period lasted approximately two hours with no lateral load (L/V = 0) to allow the bearing to reach steady state operating temperature. Figure 19 shows the corresponding temperature and vibration profiles over the ~13 hours of operation. The graph displays the temperature change (ΔT) for both the inboard (IB) and outboard (OB) bearing locations. The baseline temperatures for both the inboard and outboard sides stabilized at

~16.5°C (29.7ºF), about 7ºC (12.6ºF) below the Control Bearing Correlation line (red line). The data showed a typical temperature response for a healthy bearing operating under similar conditions, as established by UTCRS through statistical analysis of control bearing data [28].

At approximately the two-hour mark, a lateral load of 12.0 kN (2.7 kips) (L/V = 0.39) was applied, corresponding to a simulated 16.3° curve. An increase in temperature was observed, with the effect more pronounced on the inboard side, where ΔT reached 19°C (34.2ºF) above ambient. The temperature behavior is consistent with the expected redistribution of internal bearing loads in which the lateral force shifts the contact load toward the inboard rib and increases the localized contact stress.

After the lateral load was removed (~7.5 hours), the bearing temperatures gradually returned to their original baseline values. The second lateral load application of 7.6 kN (1.7 kips) (L/V = 0.24) at the 10-hour mark, corresponding to a 10.4° curve, produced a similar response. The inboard temperature showed a moderate increase, while the outboard temperature remained relatively stable, with both temperatures returning to baseline levels after the lateral load was removed. Overall, the temperature remained consistent with expected temperature profiles for a healthy bearing operating under stable conditions.

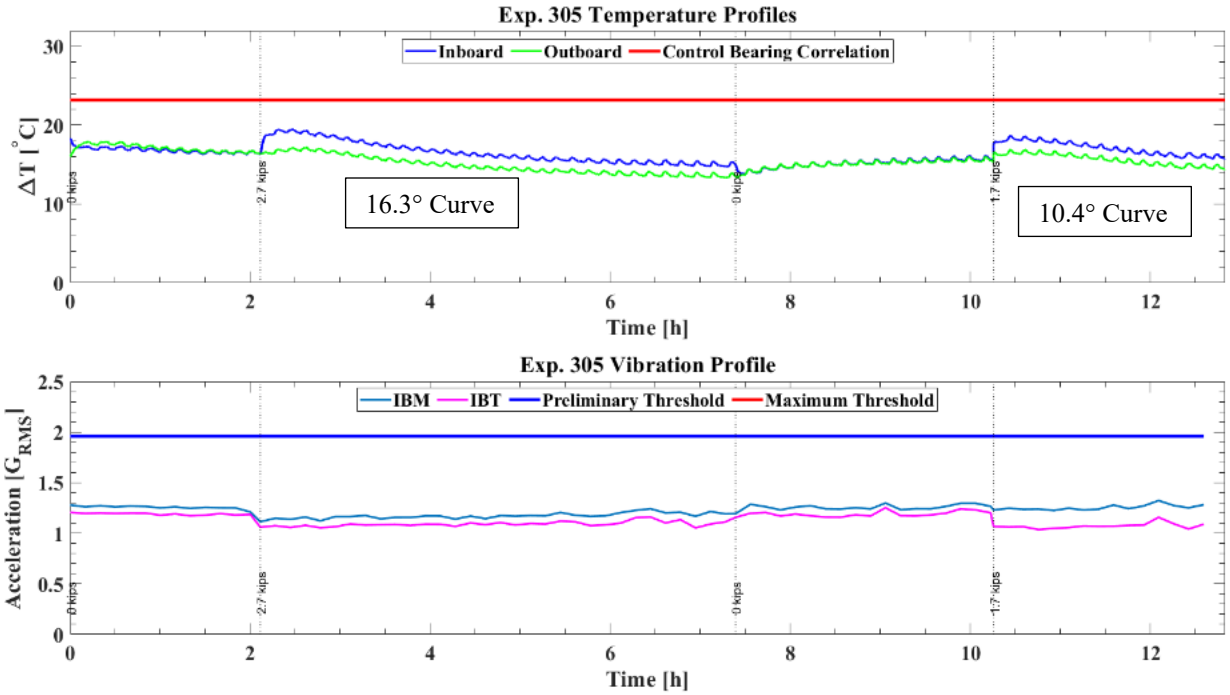

Figure 19. Control bearing temperature and acceleration at 72 kph (45 mph) for 17% load (empty railcar load) with varying lateral loads

The vibration profiles of the IBM and IBT accelerometers (cyan and magenta curves) are shown in the bottom plot of Figure 19. The baseline vibration level for both sensors remained near 1.2 G_{RMS}, well below the preliminary threshold of 2 G_{RMS} (blue line), which indicates that the bearing is healthy (defect-free).

Here, it is important to explain that vibration levels below the preliminary threshold (blue line) indicate a defect-free bearing; vibration levels above the preliminary threshold but below the maximum threshold (red line) suggest that the bearing may be defective or is a reconditioned bearing that may contain repaired defects or some minor surface damage; and vibration levels above the maximum threshold indicate a defective bearing with 97% confidence.

Minor fluctuations in the acceleration profiles coincide with the application and removal of lateral load. However, these variations are small and do not exhibit impulsive behavior, sudden increases, or upward trends indicative of surface damage or spalling. The vibration levels

remained consistent and repeatable during each load segment, confirming that the bearing operated in a stable condition and that curve negotiation does not meaningfully affect bearing temperature and vibration for a healthy bearing under the 72 kph (45 mph) and 17% load operating conditions.

4.2.2 Lateral Load and LVDT Displacement

During the experiment, lateral load and displacement measurements were collected using an LVDT, as described in Chapter III and shown in Figure 17. The displacement profile (Figure 20 bottom) aligns with the lateral load increments (Figure 20 top) applied during the experiment and corresponds directly with the observed temperature and vibration responses. At the start of the experiment, during baseline measurements, the LVDT indicated a displacement of 0.102 mm (0.004 in), attributed to its ±0.2% full-scale linearity error.

The displacement response follows the applied lateral load, increasing with L/V and returning to near-baseline values upon load removal. The maximum measured displacement approached the unmounted lateral clearance of the bearing (0.584-0.660 mm or 0.023-0.026 in), indicating that lateral loading progressively reduces internal clearance and shifts the internal load distribution.

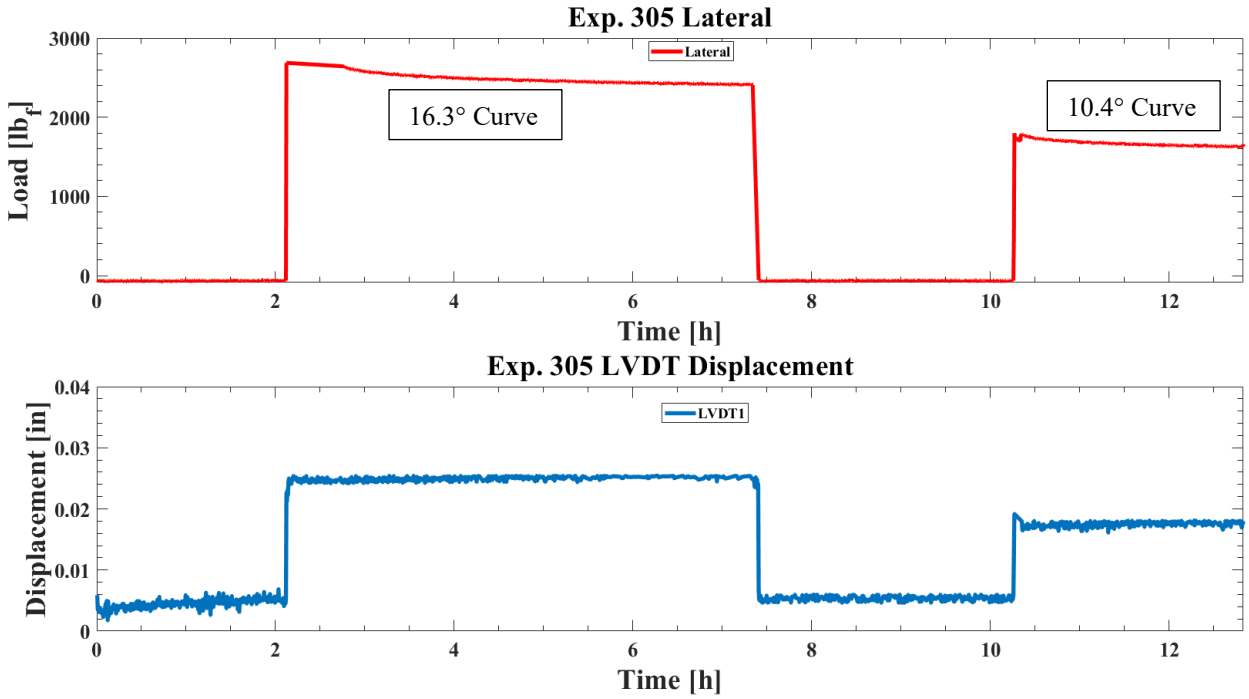

Figure 20. Control bearing lateral load and displacement at 72 kph (45 mph) for 17% load (empty railcar load) with varying lateral load

4.2.3 Motor Power and Applied Vertical Load

The motor power and the vertical load measurements were also recorded during the experiments, as shown in Figure 21. The motor power remained relatively constant throughout the test, with only minor fluctuations observed during changes in lateral load. Under baseline conditions (L/V = 0), the motor power stabilized at approximately 2.6 kW. When the 12.0 kN (2.7 kip) lateral load (L/V = 0.39) was applied near the two-hour mark, the motor power decreased slightly to approximately 2.3 kW, then returned to baseline once the load was removed. A second minor reduction in power was observed during the 7.6 kN (1.7 kip) lateral load application late in the experiment, as shown in Figure 21 (top).

Overall, the motor-power profile remained relatively stable throughout the experiment, although a measurable decrease of approximately 10% was observed during the lateral load applications. The observed reduction in motor power, despite the increase in inboard temperature, may be attributed to redistribution of internal contact forces rather than an increase

in global frictional resistance, although further investigation would be required to fully isolate this effect.

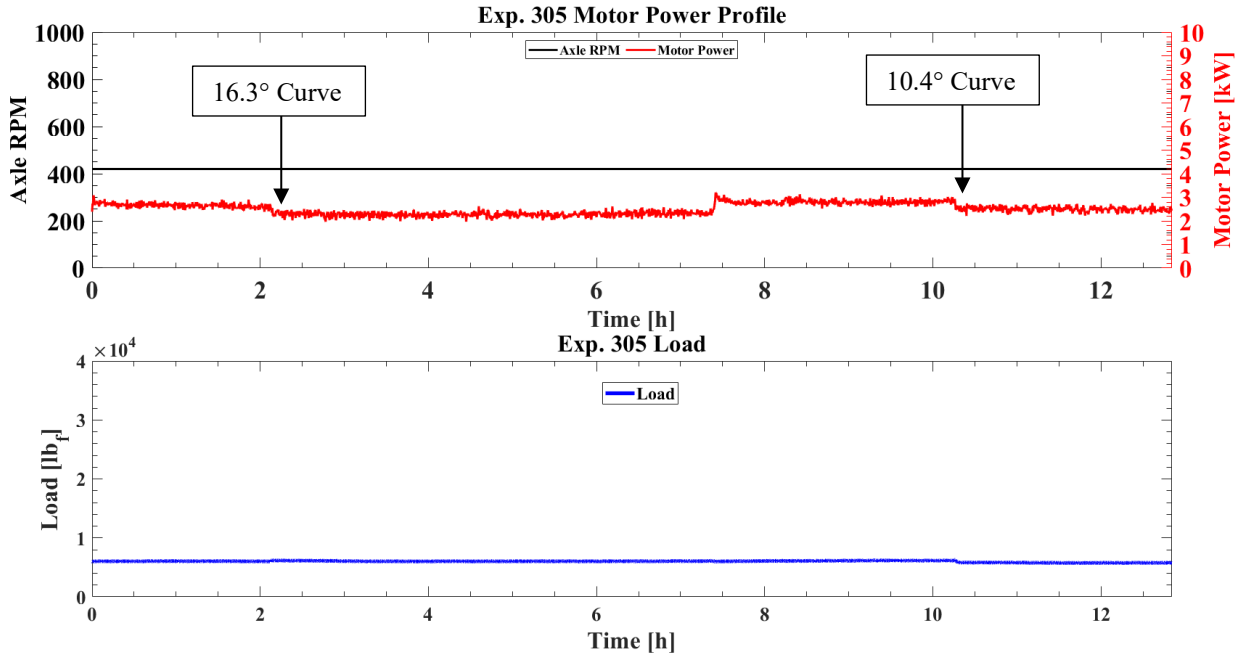

Figure 21. Control bearing power and vertical load at 72 kph (45 mph) for 17% load (empty railcar load) with varying lateral loads

4.3 Effects of Lateral Load at 72 kph (45 mph) and Fully Loaded Railcar

4.3.1 Temperature and Vibration Profiles

At 72 kph (45 mph) and 100% load, the lateral loading cases evaluated in this section included L/V ratios of 0.37, 0.25, 0.13, and 0.14, with degrees of curvature of 16°, 10.7°, 5.5°, and 5.8°, and lateral loads of 59.2 kN (13.3 kips), 40.0 kN (9.0 kips), 20.5 kN (4.6 kips), and 22.2 kN (5.0 kips), respectively. Figure 22 shows the corresponding temperature and vibration profiles over ~44 hours of operation. Prior to applying lateral loads, the bearing was allowed to reach a steady state operating temperature of approximately 37°C (66.6ºF) above ambient conditions, which served as the baseline temperature. At ~7.5 hours, a lateral load of 59.2 kN (13.3 kips) (L/V = 0.37) was applied, corresponding to a simulated 16° curve. After applying the lateral load, the inboard temperature rose to 42°C (75.6ºF) above ambient, while the outboard

temperature fell to approximately 30.5°C (54.9ºF) above ambient, dropping below the established Control Bearing Correlation threshold. This temperature behavior indicated a redistribution of internal contact forces within the bearing. The applied lateral load shifts the load path toward the inboard raceway, increasing frictional heating on the inboard side while reducing load sharing and frictional heating on the outboard side.

Once the lateral load was removed, both inboard and outboard temperatures gradually returned to their baseline values. This behavior was repeated for each subsequent loading condition, where higher lateral loads produced larger temperature differences between the inboard and outboard sides. It should be noted that the current experimental setup allows for lateral load to be applied in a single direction, whereas field service would show opposite raceways affected on the bearing mates during curve negotiation.

For smaller simulated curve degrees (5.5° and 5.8°), the temperature differences were less pronounced, and the bearing cooled more rapidly, with temperatures occasionally falling slightly below the Control Bearing Correlation. Overall, the bearing temperature remained consistent with that expected for a healthy, defect-free bearing.

The vibration levels remained near 1.7 G_{RMS} throughout the experiment. Some slight oscillations appeared during transitions of lateral loading; however, no significant changes in vibration were observed. Overall, these results indicate that, for a healthy bearing, simulated curve negotiation does not significantly influence vibration levels under the tested operating conditions.

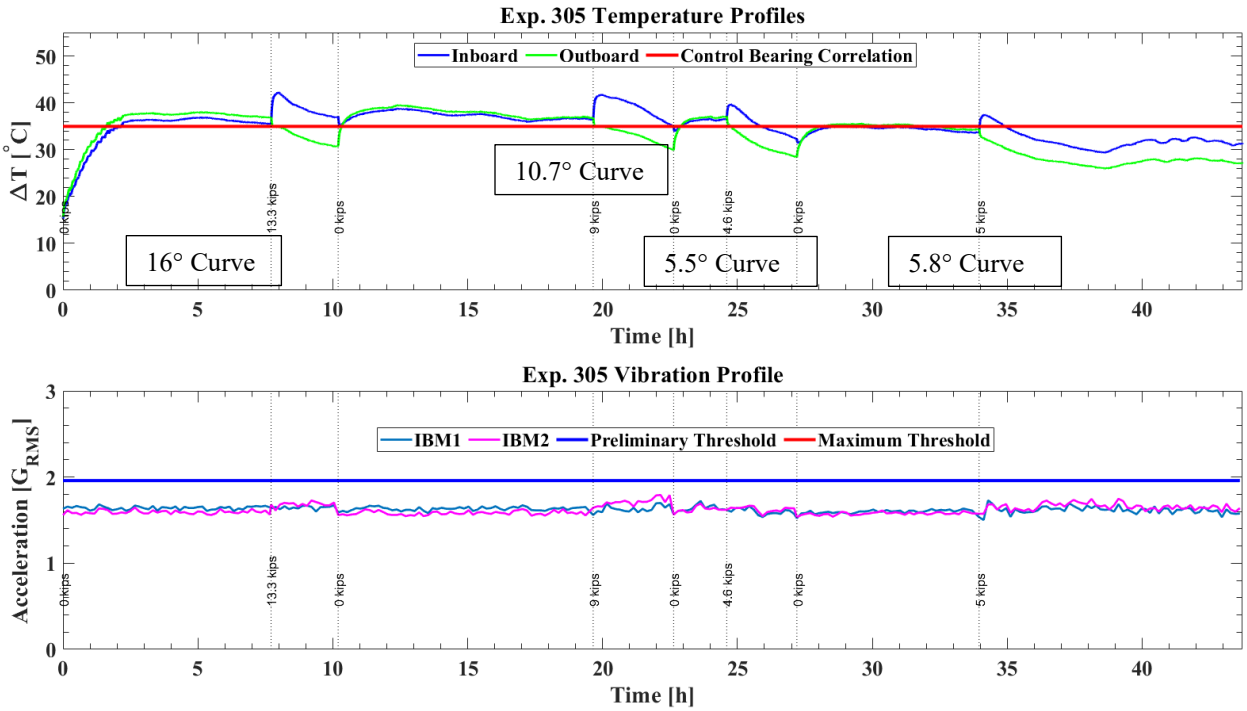

Figure 22. Control bearing temperature and acceleration at 72 kph (45 mph) for 100% load (fully loaded railcar) with varying lateral loads

4.3.2 Lateral Load and LVDT Displacement

For the control bearing under 100% load, lateral load and displacement measurements were collected and are plotted in Figure 23. The displacement response closely corresponds to the applied lateral loads and the simulated curve severity. Similar to the unloaded bearing, the displacement magnitude increased with the applied lateral load and approached the measured unmounted lateral clearance, indicating a progressive reduction in internal clearance and a corresponding shift in the internal load distribution.

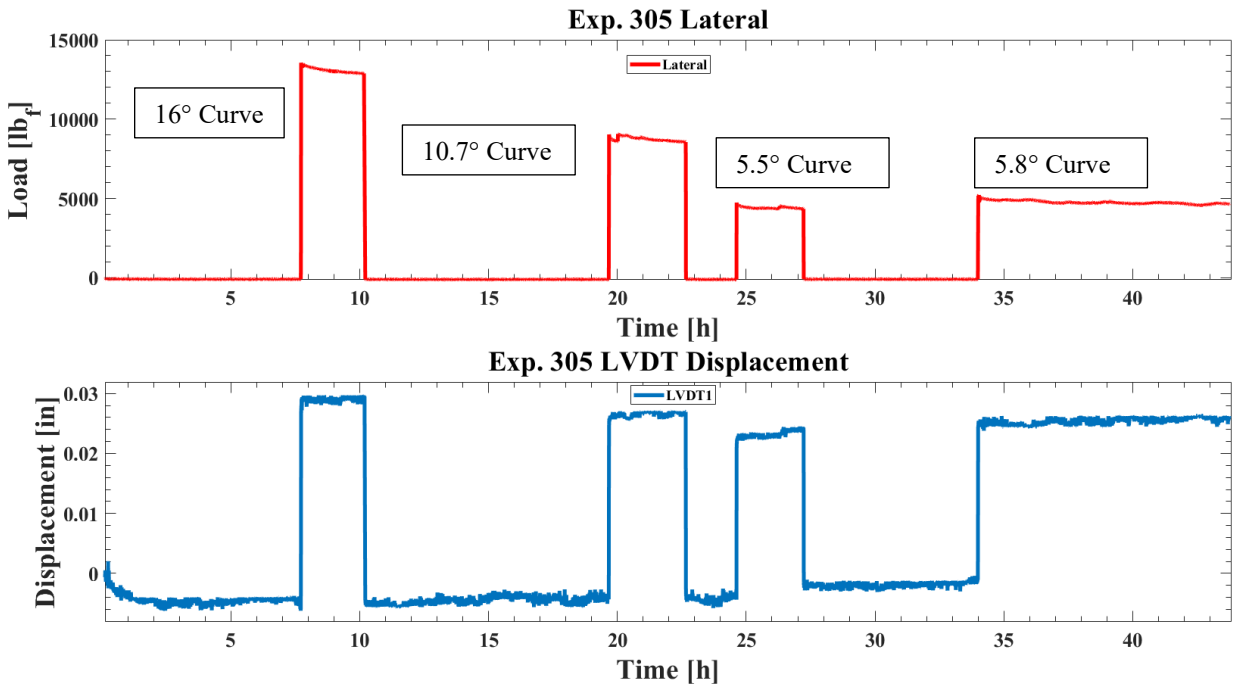

Figure 23. Control bearing lateral load and displacement at 72 kph (45 mph) for 100% load (fully loaded railcar) with varying lateral load

4.3.3 Motor Power and Applied Vertical Load

Motor power and vertical load measurements were recorded for the fully loaded bearing, and are plotted in Figure 24. Motor power remained between 6.2 kW and 7 kW throughout the experiment, with only minor fluctuations. No consistent relationship between lateral load and motor power variation was observed. Although small oscillations were present due to system dynamics, these fluctuations did not correspond directly to changes in bearing temperature or vibration. As with the 17% load condition, the results for the fully loaded railcar condition indicate that lateral loading during simulated curve negotiation has minimal influence on motor power consumption for a healthy bearing.

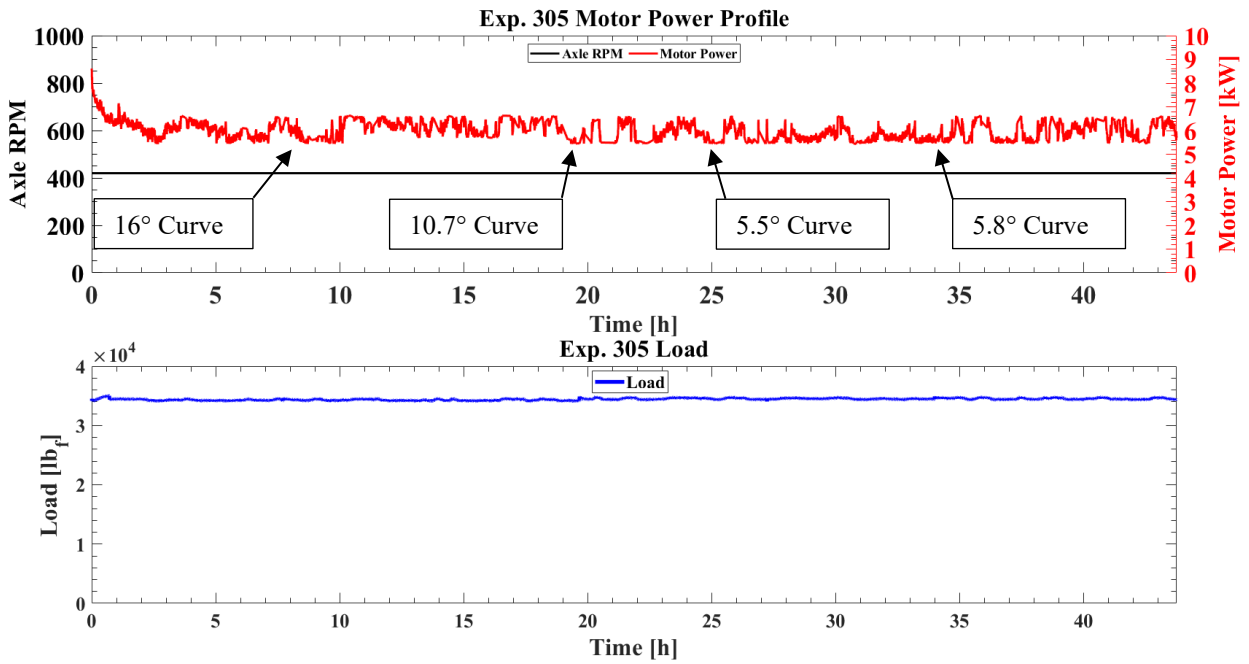

Figure 24. Control bearing power and vertical load at 72 kph (45 mph) for 100% load (fully loaded bearing) with varying lateral loads

4.4 Summary of Results

For the control bearing (defect-free, healthy) under unloaded (i.e., empty railcar or 17% load) and fully loaded (100% load) operating conditions, measured thermal and dynamic responses from Experiment 305 are summarized in Table 8. The table lists the maximum and average temperature change above ambient (ΔT), vibration (acceleration), power consumption, and measured displacement for each lateral load case studied. The final column, $\Delta T/F_{lat}$, quantifies the sensitivity of temperature to lateral loading by subtracting the average bearing operating temperature from the baseline temperature (ΔT) and dividing by the applied lateral load (F_{lat}), providing an estimate of the temperature response per unit lateral force applied. Although there are no significant temperature changes at either 17% or 100% load under any lateral load conditions, the largest temperature change occurred at 17% load with a 7.6 kN (1.7 kip) force, yielding a response of 0.25ºC/kN (1.1ºC/kip). At 17% load (unloaded railcar load), the vibration levels within the healthy bearing decrease under lateral loading, whereas at 100%

load, the system's vibrational response remains unchanged regardless of the applied lateral load. The data suggests that, for the unloaded condition, the applied lateral load tends to decrease roller vibration by reducing the internal clearances within the bearing.

Table 8. Lateral response summary of a control bearing operating at 72 kph (45 mph)

Load [%]	**F_{lat} [kN] / [kips]**	**Max ΔT [ºC] / [ºF]**	**Avg. ΔT [ºC] / [ºF]**	**Accel. [G_{RMS}]**	**Power [kW]**	**Disp. [mm] / [in]**	**ΔT / F_{lat} [ºC/kN] / [ºC/kips]**
17	0	16.5 / 29.7	16.5 / 29.7	1.25	2.6	0.102 / 0.004	-
17	12.0 / 2.7	19.0 / 34.2	17.8 / 32.0	1.1	2.3	0.635 / 0.025	0.20 / 0.9
17	7.6 / 1.7	18.4 / 33.1	17.5 / 31.5	1.2	2.5	0.432 / 0.017	0.25 / 1.1
100	0	37.0 / 66.6	37.0 / 66.6	1.7	6.2	-0.102 / -0.004	-
100	59.2 / 13.3	42.0 / 75.6	39.0 / 70.2	1.7	6.3	0.711 / 0.028	0.09 / 0.4
100	40.0 / 9.0	42.0 / 72.0	39.0 / 70.2	1.7	6	0.660 / 0.026	0.13 / 0.6
100	20.5 / 4.6	40.0 / 72.0	38.5 / 69.3	1.7	5.8	0.584 / 0.023	0.16 / 0.7
100	22.2 / 5.0	37.3 / 67.1	37.2 / 67.0	1.7	6.1	0.610 / 0.024	0.02 / 0.1

CHAPTER V

DEFECTIVE BEARING: RESULTS AND DISCUSSION

5.1 Experiment 296B: Defective Bearing

This chapter focuses on results obtained from Experiment 296B: the evaluation of lateral loading on a defective bearing. The bearing used in this experiment contained a large defect in the form of a spall on the outboard raceway of the bearing cup (outer ring). The spall had an initial area of A_o = 24 cm^2 (3.72 in^2) which is pictured in Figure 25. The bearing had an accumulated total service distance of 43,130 km (26,800 mi) with an unmounted lateral clearance of 0.533-0.635 mm (0.021-0.025 in).

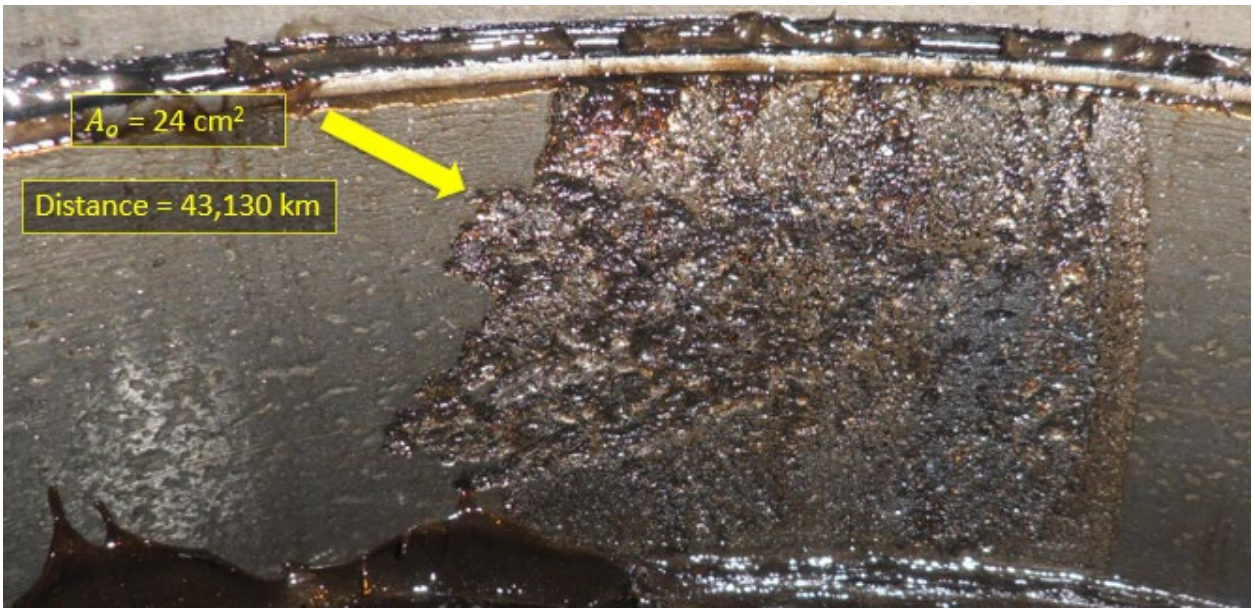

Figure 25. Defective bearing used in Experiment 296B with a large spall on the outboard (OB) raceway of the cup (outer ring)

A complete summary of the experimental cases examined was provided in Chapter 3 in Table 6. Given the large volume of data collected, this chapter focuses on the results most

relevant to the research objectives. The following sections present the results for Experiment 296B at 100% load at two speeds: 72 kph (45 mph) and 97 kph (60 mph). At 72 kph (45 mph), the evaluated L/V ratios were 0.26, 0.38, and 0.24, as discussed in Section 5.2. Section 5.3 presents results for 97 kph (60 mph) with L/V ratios of 0.12, 0.24, 0.37, and 0.25. The results for the cases from Table 6 not described in this chapter are included in APPENDIX C.

5.2 Effects of Lateral Load at 72 kph (45 mph) and Fully Loaded Railcar

5.2.1 Temperature and Vibration Profiles

For this test, the bearing cup was positioned such that the spalled region on the raceway was directly under the applied vertical load. The experiment ran for approximately 33 hours. At 72 kph (45 mph) and 100% load, L/V ratios of 0.26, 0.38, and 0.24 were tested with degrees of curvature of 10.8°, 16.0°, and 10.3° corresponding to lateral loads of 40.9 kN (9.2 kips), 60.1 kN (13.5 kips), and 38.7 kN (8.7 kips), respectively. The temperature and vibration responses of the bearing are shown in Figure 26. At the beginning of the experiment, a baseline temperature of 37°C (66.6ºF) above ambient was established by allowing the bearing to reach steady state operating conditions. The lateral load of 40.9 kN (9.2 kips) was then applied. The thermal response was comparable to that of the control bearing, with the inboard temperature rising and the outboard temperature dropping. Under the 10.8° curve condition, the inboard temperature peaked at approximately 48.5°C (87.3ºF) above ambient, while the outboard side remained near 39.5°C (71.1ºF) above ambient. When the lateral load was increased to simulate a 16° curve, the thermal response became more pronounced, with the inboard temperature reaching approximately 49.5°C (89.1ºF) above ambient and the outboard remaining near 39.5°C (71.1ºF) above ambient. In each case, the temperatures returned to the baseline after the lateral load was removed. Just like in the case of the healthy bearing, the results indicate that lateral loading

shifted the internal load path toward the inboard side even in the presence of an outboard raceway spall.

The vibration measurements showed that the defective bearing operated with a baseline acceleration of approximately 7.4 GRMS at the start of the experiment, which is well above the maximum threshold (red line), indicative of the presence of a defect within the bearing. Under the 10.8° curve condition, the bearing vibration increased to approximately 8.6 GRMS, which likely indicates that the spall defect was being aggravated under L/V conditions or that the spall was propagating. During bearing operation, spall propagation generates metallic debris that becomes trapped within the rolling elements and lubricant, accelerating defect growth and increasing the vibration levels within the bearing.

During simulation of a 16° curve, vibration levels decreased to 6.3 G_{RMS} and remained stable. After the lateral load was removed, near the 26-hour mark, vibration levels returned to baseline, exhibiting similar fluctuations. The removal of the lateral load altered the internal load distribution within the bearing, which may explain the observed fluctuations in acceleration levels. The results suggest that higher L/V ratios produce more constrained roller motion as the rollers pass over the defect. In other words, the increased lateral load tends to suppress the likelihood of roller misalignment as the rollers pass through the spalled region of the cup (outer ring) raceway.

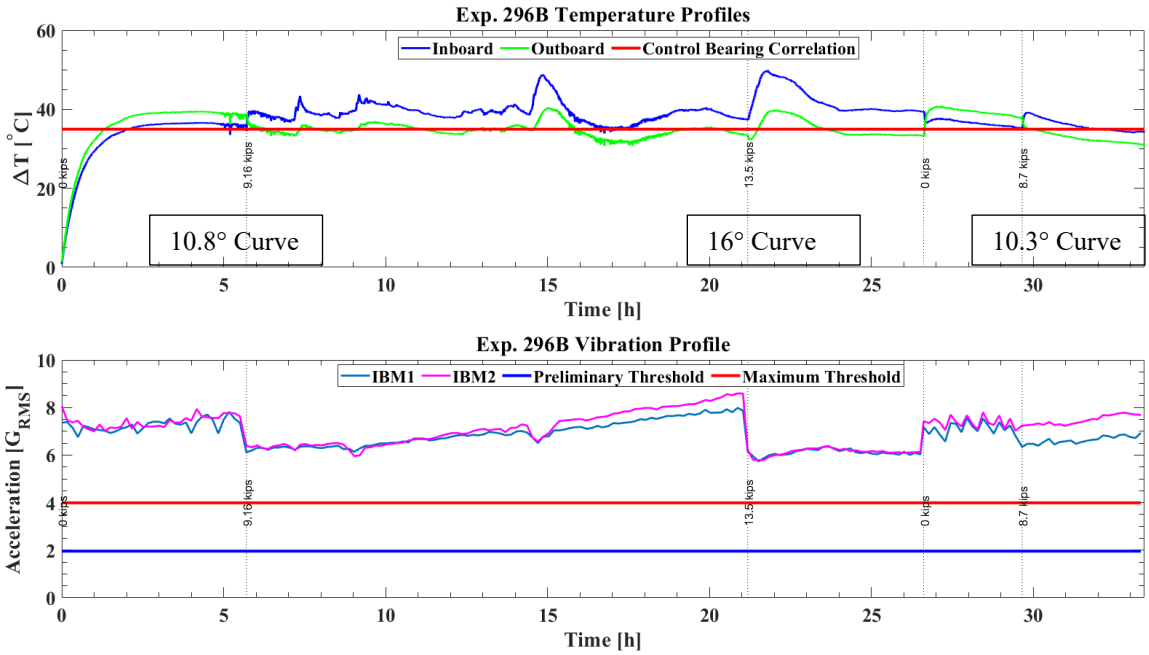

Figure 26. Defective bearing temperature and acceleration at 72 kph (45 mph) for 100% load (fully loaded railcar) with varying lateral loads

5.2.2 Lateral Load and LVDT Displacement

The lateral load and displacement profiles shown in Figure 27 align with the applied loading sequence and correlate with the temperature and vibration profiles. As the lateral load increased, displacement rose from about 0.381 mm (0.015 in) at the 10.8º curve to 0.610 mm (0.024 in) at the 16º curve, then decreased to 0.457 mm (0.018 in) at the 10.3º case. The peak displacement was roughly comparable to the bearing's unmounted lateral clearance, suggesting that the lateral load gradually suppressed the internal clearance and moved the bearing into a more constrained internal state.

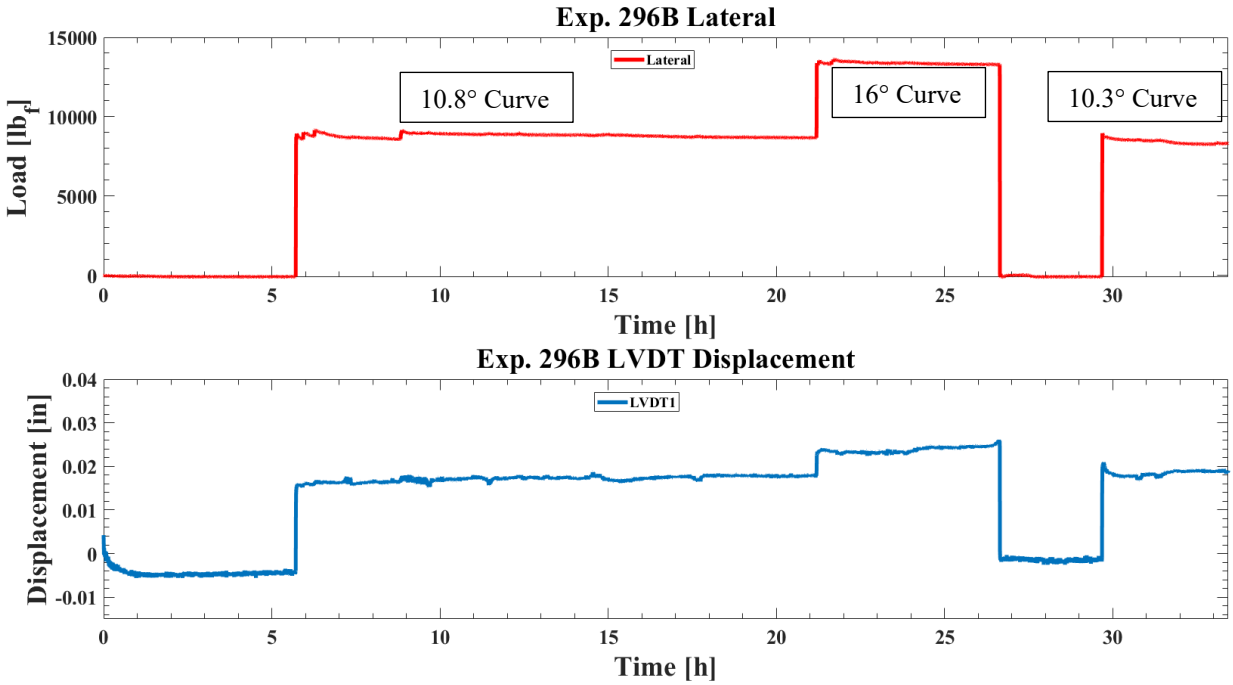

Figure 27. Defective bearing lateral load and displacement at 72 kph (45 mph) for 100% load (fully loaded railcar) with varying lateral load

5.2.3 Motor Power and Applied Vertical Load

Experiment 296B shows that while motor power responded to lateral loading, axle speed and the vertical applied load were not affected by it. Baseline power was stable at 5.5 kW, but it increased to about 7 kW when a lateral load simulating a 10.8º curve was applied. The power profile also showed more oscillations, peaking near 8.5 kW under an equivalent lateral load of a 16º curve. While motor power alone does not pinpoint the exact friction mechanism, the rise in temperature and vibration levels within the bearing suggest that lateral loading altered the internal load distribution, thus affecting the thermal and dynamic response of the bearing.

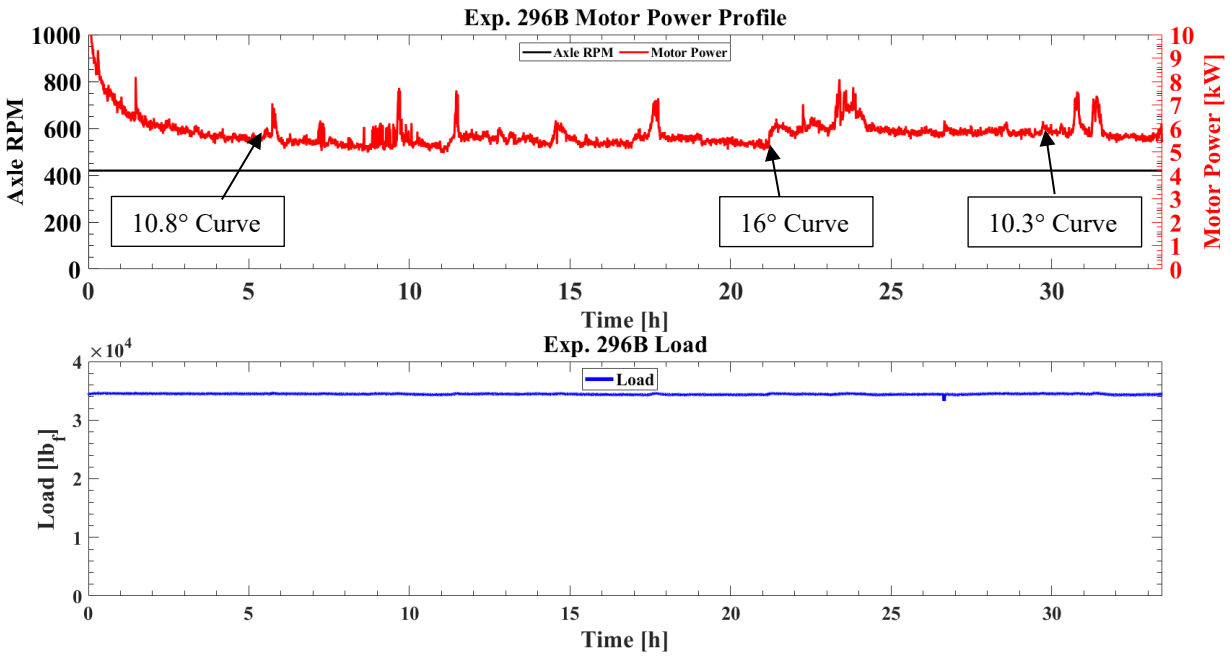

Figure 28. Defective bearing power and vertical load at 72 kph (45 mph) for 100% load (fully loaded railcar) with varying lateral loads

5.3 Effects of Lateral Load at 97 kph (60 mph) and Fully Loaded Railcar

At 97 kph (60 mph) and 100% load (fully loaded railcar), L/V ratios of 0.12, 0.24, 0.37, and 0.25 were tested with degrees of curvature of 3.0°, 5.7°, 8.7°, and 6.0° corresponding to lateral loads of 19.6 kN (4.4 kips), 38.3 kN (8.6 kips), 58.3 kN (13.1 kips), and 40.0 kN (9.0 kips), respectively.

5.3.1 Temperature and Vibration Profiles

At the start of the experiment, the bearing's baseline (steady state) temperature was about 52.5°C (94.5ºF) above ambient, as shown in Figure 29. When the lateral load was applied, the thermal responses were similar to those in previous tests; the bearing inboard raceway temperature increased, while the outboard raceway temperature either decreased slightly or remained relatively lower. Under the 6° curve condition, the inboard temperature rose from approximately 53.2°C (95.8ºF) to 61.5°C (110.7ºF) above ambient. Increasing the lateral load to 13.1 kips (L/V = 0.37, corresponding to an 8.7° curve) raised the inboard raceway temperature to

about 65.3°C (117.5ºF) above ambient. These results indicate that at 97 kph (60 mph), the inboard temperature change scaled with lateral load, increasing by roughly 0.23ºC/kN (1°C/kip) under higher loads. The outboard side experienced less temperature increase, consistent with a redistribution of internal contact forces toward the inboard rib and the roller large-end contact region.

The defective bearing operated above the maximum vibration threshold from the start of the experiment, with the IBM and IBT accelerometers (refer to Figure 14) recording roughly 13.8 and 12.6 GRMS, respectively. When the lateral load was first applied at 19.6 kN (4.4 kips) (L/V = 0.12), the vibration signals stabilized but did not decrease. Unlike the experiments performed with the healthy (defect-free) bearing, the vibration levels within the defective bearing remained higher during lateral loading intervals and decreased when the lateral load was removed. This behavior can be explained by the combined effects of lateral loading and defect interactions, where the reduced internal spacing caused by the application of the lateral load enhances the roller/spall contact resulting in higher vibration levels within the bearing. Additionally, the IBT accelerometer response increased and approached the IBM accelerometer response under lateral load, but after lateral load removal, it dropped and remained around 12.5 G_{RMS}.

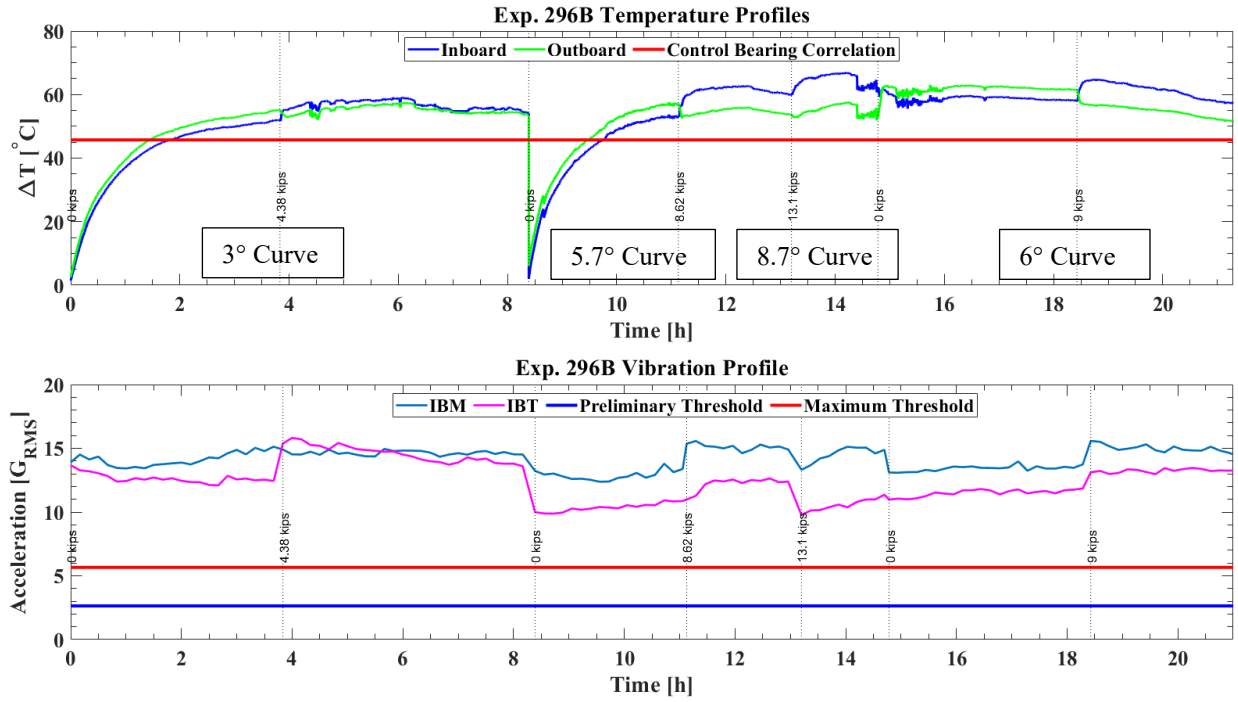

Figure 29. Defective bearing temperature and acceleration at 97 kph (60 mph) for 100% load (fully loaded railcar) with varying lateral loads

5.3.2 Lateral Load and LVDT Displacement

The lateral load and displacement profiles for this experiment are shown in Figure 30. Initially, the LVDT signal shifted to approximately -0.254 mm (-0.010 in), indicating an offset from the original zero reference. This shift could be due to mounting tolerances, sensor bracket movement, or other instrumentation effects during testing. Using this shifted reading as the baseline, the measured displacements under simulated 3°, 5.7°, 8.7°, and 6° curve conditions were approximately 0.686 mm (0.027 in), 0.660 mm (0.026 in), 0.813 mm (0.032 in), and 0.584 mm (0.023 in), respectively. These displacements remained roughly within the available unmounted lateral clearance. However, because the LVDT signal exhibited an offset and did not fully return to its initial value after the lateral load was removed, the displacement data should be treated as trends rather than as absolute measurements of bearing position. Nonetheless, these

results demonstrate that the applied lateral loads significantly reduced the available lateral clearance within the bearing.

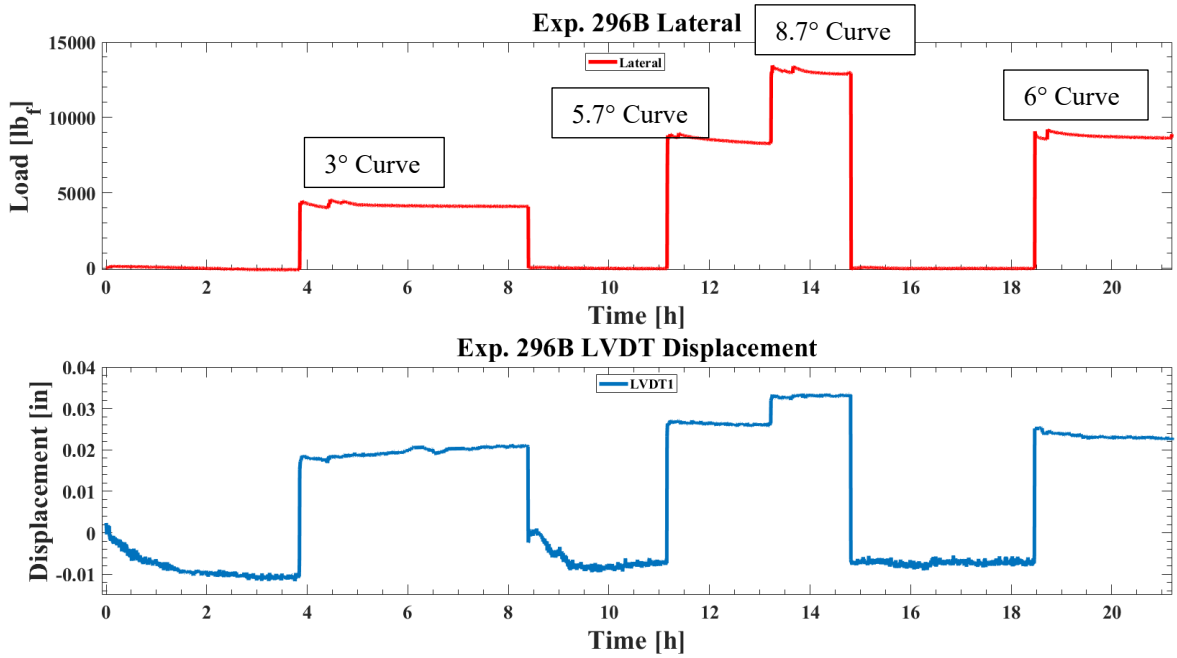

Figure 30. Defective bearing lateral load and displacement at 97 kph (60 mph) for 100% load (fully loaded railcar) with varying lateral load

5.3.3 Motor Power and Applied Vertical Load

The data plotted in Figure 31 indicate that the motor power was affected slightly by the applied lateral load, but the axle speed and applied vertical load remained steady throughout the test. Initially, the motor power stabilized around 7.3 kW at baseline. When a lateral load of 19.6 kN (4.4 kips) (L/V = 0.12) was applied to simulate a 3° curve, the power increased to about 7.9 kW, reflecting the additional torque required to maintain speed. The test was restarted at roughly the 8.5-hour mark, and the new baseline settled at approximately 7.7 kW. Under the 5.7° curve condition, which corresponds to 38.3 kN (8.6 kips) (L/V = 0.24), the power showed more pronounced spikes, reaching approximately 8.5 kW. This motor power behavior aligns with previously shown power profiles for the test cases examined under the 72 kph (45 mph) speed condition.

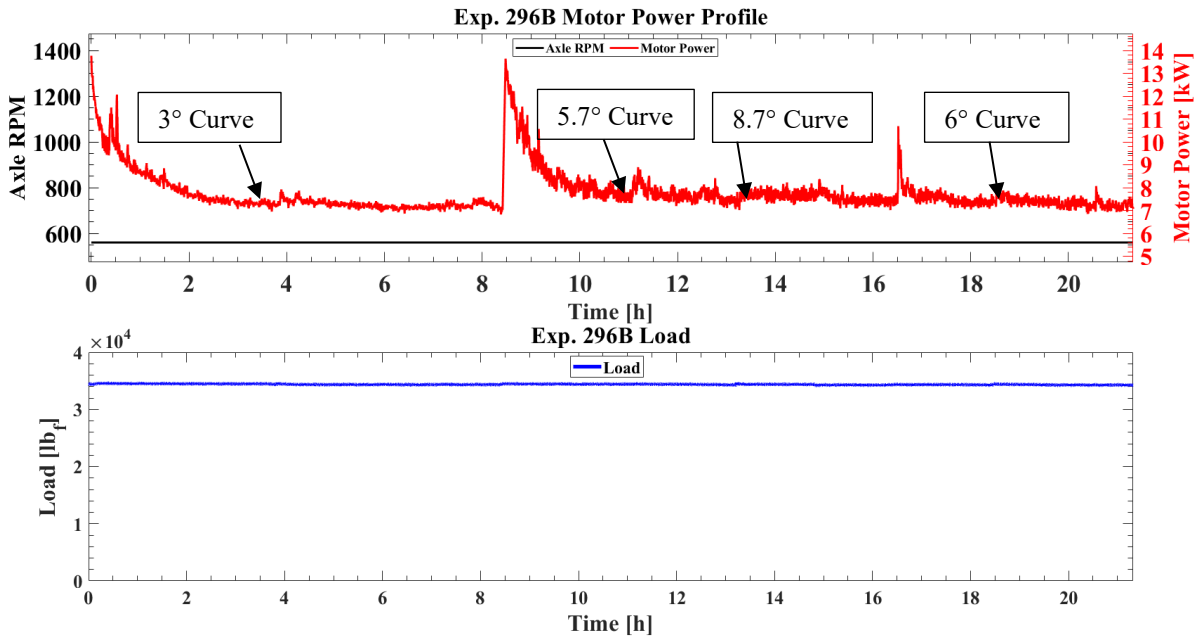

Figure 31. Defective bearing motor power and vertical load at 97 kph (60 mph) for 100% load (fully loaded railcar) with varying lateral loads

5.4 Summary and Conclusion of Results

Table 9 summarizes the operating conditions and measured responses for the defective bearing during Experiment 296B. The table lists the maximum and average bearing operating temperature above ambient (ΔT), vibration levels (acceleration), motor power consumption, and measured displacement for each lateral load case. The final column shows the change in maximum temperature rise relative to the zero-lateral-load condition, normalized by the applied lateral load, thereby providing an estimate of the thermal response per unit lateral force.

Table 9. Lateral response summary of the defective bearing in Experiment 296B

Speed [kph] / [mph]	**Load [%]**	**F_{lat} [kN] / [kips]**	**Max ΔT [ºC] / [ºF]**	**Avg. ΔT [ºC] / [ºF]**	**Accel. [G_{RMS}]**	**Power [kW]**	**Disp. [mm] / [in]**	**ΔT / F_{lat} [ºC/kN] / [ºC/kips]**
72 / 45	100	0	37.0 / 66.6	37.0 / 66.6	7.4	5.5	-0.076 / -0.003	-
72 / 45	100	40.9 / 9.2	48.4 / 87.1	42.7 / 76.9	8.6	7.3	0.381 / 0.015	0.27 / 1.2
72 / 45	100	60.1 / 13.5	49.2 / 88.6	43.1 / 77.6	6.3	7.5	0.457 / 0.018	0.20 / 0.9
72 / 45	100	20.5 / 4.6	39.0 / 70.2	38.0 / 68.4	7.3	7	0.381 / 0.015	0.09 / 0.4
97 / 60	100	0	52.5 / 94.5	52.5 / 94.5	14.2	7.4	-0.254 / -0.010	-
97 / 60	100	19.6 / 4.4	59.0 / 106.2	55.8 / 100.4	14.7	7.3	0.432 / 0.017	0.34 / 1.5
97 / 60	100	38.3 / 8.6	62.4 / 112.3	57.5 / 103.5	14.6	7.6	0.635 / 0.025	0.27 / 1.2
97 / 60	100	58.3 / 13.1	67.0 / 120.6	59.8 / 107.6	15	7.5	0.762 / 0.030	0.25 / 1.1
97 / 60	100	40.0 / 9.0	64.3 / 115.7	58.4 / 105.1	15.3	7.8	0.559 / 0.022	0.29 / 1.3

5.4.1 Understanding Temperature Trends

The temperature trends in this study were observed during the application of a lateral load to simulate curve negotiation. In the laboratory setup, the lateral load was applied to the outboard side of the bearing adapter. The design of the tapered roller bearing directed this lateral load inward, increasing contact at the inboard cone rib and the large roller end, as illustrated in Figure 32. This contact increased localized sliding friction, resulting in a rapid rise in inboard temperature during lateral loading. However, following the abrupt temperature rise, a cool down period ensued even with the lateral load still applied. This behavior can be seen in almost all the temperature profiles shown in this study.

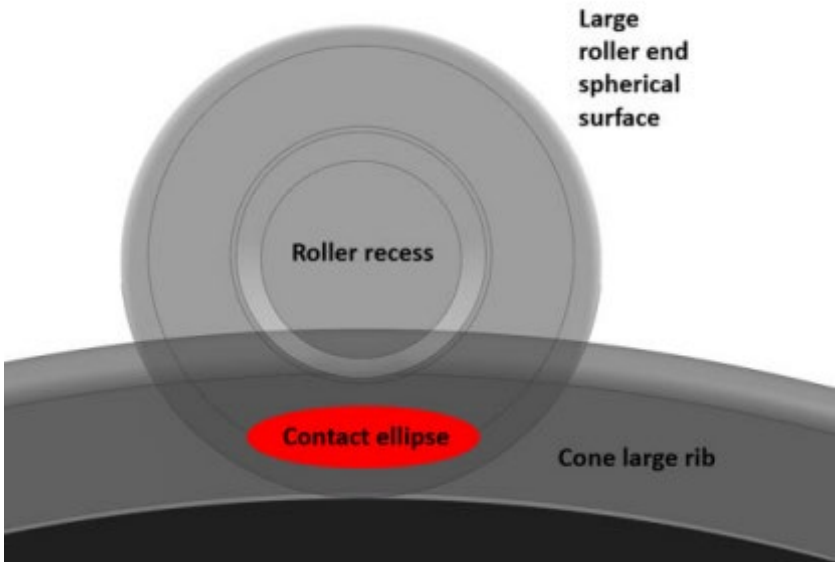

Figure 32. Roller and cone interaction displaying the contact ellipse zone [30]

A plausible explanation for this behavior is that, as the cone rib temperature increased, the grease became less viscous (i.e., thinner) causing it to spread more efficiently into the rib-roller contact zones of the tapered roller bearing. This action likely reduced localized friction and helped dissipate heat, enabling the bearing to reach thermal equilibrium. Consequently, the inboard temperature gradually decreased and stabilized even under lateral loading. Simultaneously, the shifted load path reduced contact severity on the outboard side, as shown in Figure 33, which explains the consistent drop in outboard raceway temperature. This behavior was repeatable in the healthy bearing (Experiment 305), whereas the defective bearing (Experiment 296B) exhibited larger temperature fluctuations due to the altered rib-roller contact zone caused by the larger outboard raceway spall.

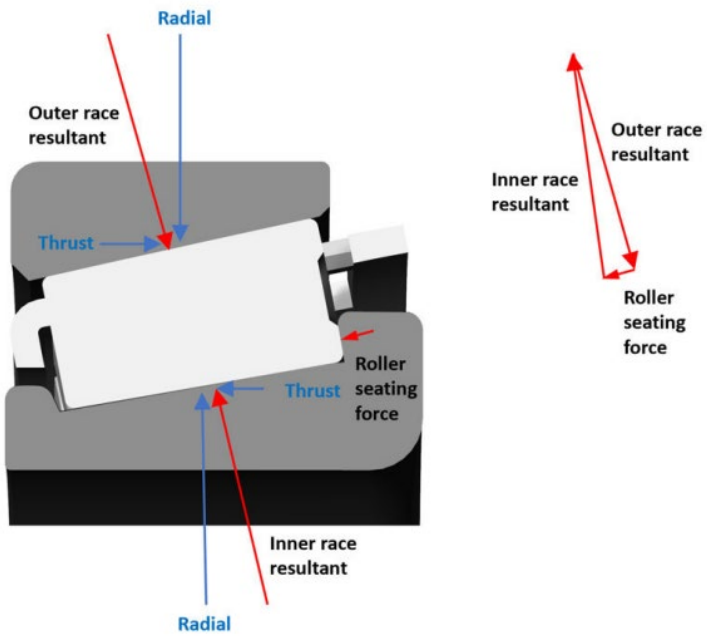

Figure 33. Roller and cone interaction side view showing the seating force caused by the tapered roller angle [30]

The temperature profiles in Figure 34 clearly demonstrate this behavior. During the 97 kph (60 mph) test with lateral load on the defective bearing, the inboard temperature gradually increased, while the outboard temperature decreased and then stabilized. Under prolonged, continuous lateral loading, the inboard temperature continued to rise, reflecting ongoing frictional heating from the altered internal load path and increased contact at the inboard cone rib. This temperature pattern represents a worst-case laboratory scenario. In field service conditions, a bearing would not typically experience continuous curve-negotiation loading for hours. Instead, trains repeatedly enter and exit curved track, limiting the duration of sustained lateral loading and allowing the operating temperature to recover between events. Consequently, the bearing temperature reflects the cumulative effects of operating conditions over longer periods, whereas vibration responds much faster to transient load changes and defect interactions. Thus, vibration is the more immediate indicator of transient events, whereas temperature is a slower measure of cumulative bearing severity.

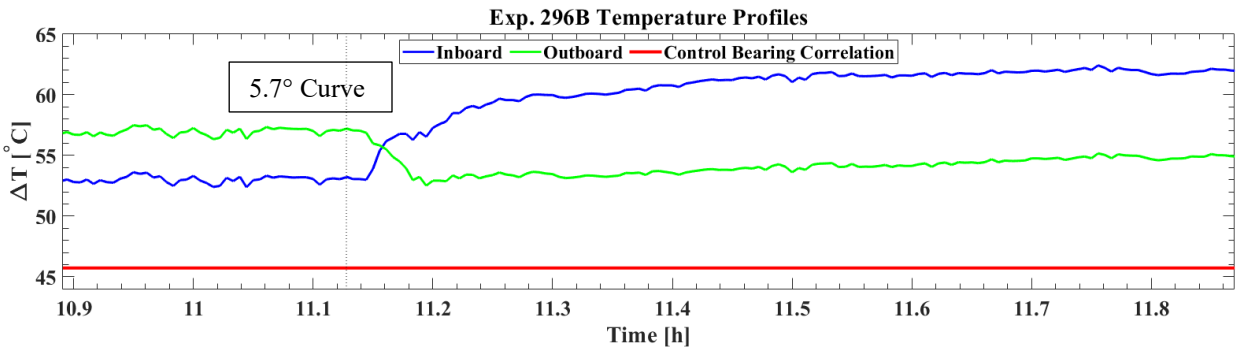

Figure 34. Temperature profile of Experiment 296B-defective bearing at 97 kph (60 mph) for 100% load (fully loaded railcar)

5.4.2 Spall Defect Growth Prognostics

Post-test inspection of the defective bearing used in Experiment 296B showed clear signs of spall propagation, consistent with the thermal and vibration data observed during testing. Comparing pre-test (Figure 25) and post-test (Figure 35) photographs, the outboard raceway cup spall area increased from an initial area of A_o = 24 cm^2 (3.72 in^2) to a final area of A_c = 48.3 cm^2 (7.48 in^2) after running 72,550 km (45,081 mi), yielding a spall growth ratio of 2, relative to the pre-test mileage of 43,130 km (26,800 mi). The measured growth remained consistent with the general growth correlation patterns displayed in Figure 36, indicating that the defect propagation stayed near the expected spall area growth ratio correlation (red line) [31]. Overall, the evidence suggests that simulated curve negotiation did not accelerate spall growth beyond typical propagation trends.

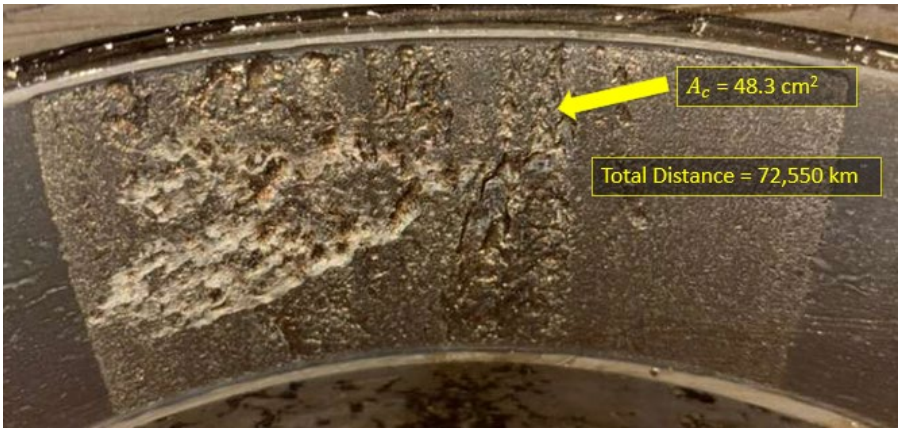

Figure 35. Post-test of the defective cup used with an OB spall

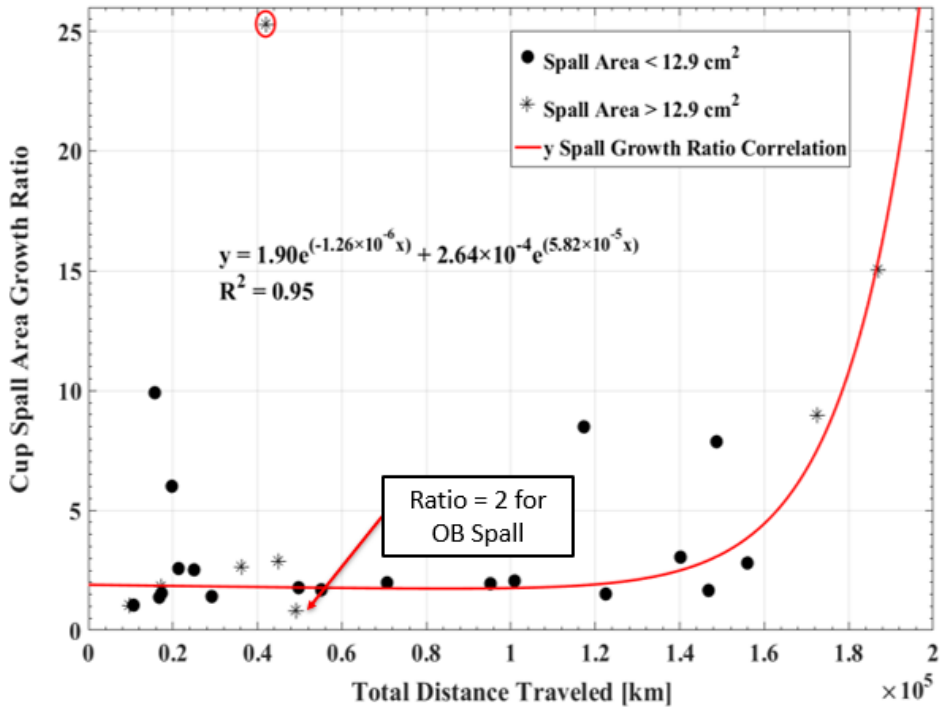

Figure 36. Spall Area Growth Ratio versus total distance traveled [31]

In addition to the growth of the original outboard cup raceway defect, post-test inspection revealed new spalling on the inboard cup raceway, as depicted in Figure 37. Spall propagation is inherently dynamic and does not proceed at a constant rate. Growth tends to be rapid during early initiation, then may slow as the defect expands across the raceway width or encounters local geometric constraints, before increasing again as circumferential propagation continues. The spall area growth rate is defined as

$$Spall\ Area\ Gowth\ Rate = \frac{(Current\ Spall\ Area\ -\ Original\ Spall\ Area)}{Total\ Distance\ Traveled} \qquad (7)\ [31]$$

The trends shown in Figure 38 indicate that both the outboard and inboard cup raceway defects remain generally consistent with the fitted growth relationships. Accordingly, while lateral loading seems to have affected the temperature and vibration response of the bearing during operation, the post-test observations do not provide strong evidence that it accelerated spall

propagation beyond the expected defect-growth behavior witnessed in railroad tapered roller bearings.

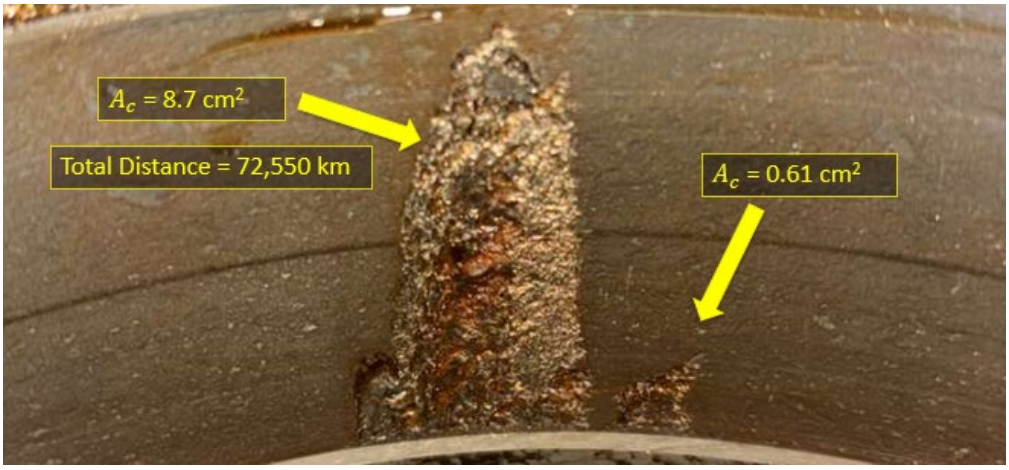

Figure 37. Inboard cup raceway spalls that developed during testing of the defective bearing

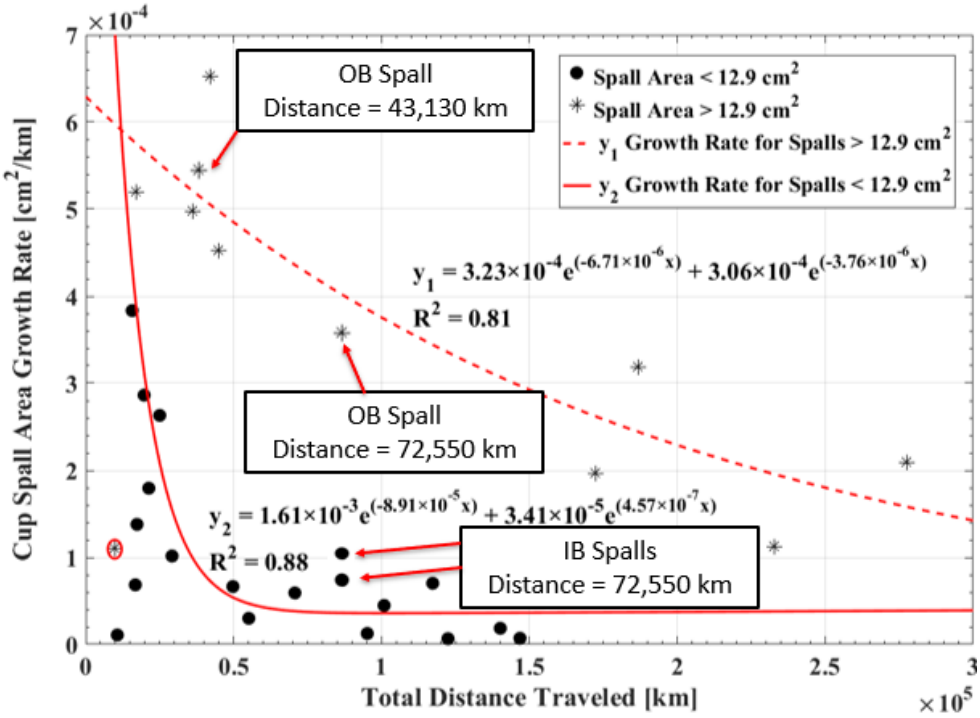

Figure 38. Spall Area Growth Rate versus total distance traveled since initiation [31]

CHAPTER VI

CONCLUSIONS

The main objective of this study was to explore the effects of lateral loads on healthy and defective railroad bearings. In freight rail service, bearings experience lateral loads when a train navigates curves or if one or more of the railcars (i.e., bogies) exhibit hunting events in which the car body rocks laterally. These events can introduce significant lateral loads and, depending on their magnitude, the railcar total weight, and the train speed, can contribute to conditions associated with derailment risk. To evaluate these effects under controlled laboratory conditions, a dedicated experimental fixture capable of applying lateral forces was designed, fabricated, and integrated into the University Transportation Center for Railway Safety (UTCRS) Single Bearing Tester. This modified configuration enabled a systematic evaluation of bearing behavior under combined lateral and vertical loading (L/V) representative of curve negotiation and/or bogie hunting events.

In this study, a healthy and a defective bearing were subjected to lateral loads of up to 60.1 kN (13.5 kips) at varying operating speeds and railcar loads, simulating several curves with degrees ranging from 3° to 16.3°. The results indicated that the effect of lateral loads on bearing operating temperature was marginal and was in the order of about 1ºC for every 4.45 kN (1.0 kip) of applied lateral load, on average. However, this effect is largely due to the extended application of lateral load on the bearing under laboratory scenarios, as a bearing in field service operation would not typically experience continuous curve negotiation for several hours. The temperature increase appeared to subside once the lateral load was removed. When lateral load

was applied at the outboard side of the test configuration, an increase in temperature was consistently observed on the inboard side of the bearing, while a corresponding decrease occurred on the outboard side. This response was consistent with redistribution of the internal load path within the tapered roller bearing, where contact friction shifted toward the inboard cone rib and roller large-end contact region, increasing localized sliding friction on the inboard side while reducing it on the outboard side. This temperature rise occurred more rapidly at higher lateral loads; however, the onset of this trend was already noticeable at lateral loads of 40.0 kN (9 kips).

The inboard temperature response observed in this study was strongly influenced by the current experimental configuration. During curve negotiation, centrifugal forces act on regions farthest from the center of the curve, resulting in increased loading on the inboard side of the bearing for the inner rail. In the laboratory setup, the applied lateral load forced the rollers into a more constrained condition against the inboard ring, thereby reducing the available internal clearance. As a result, all rollers on the inboard side became engaged, although the rollers within the vertically loaded zone continued to experience the highest stresses. At the same time, the outboard raceway experienced reduced localized sliding friction at the cone rib, despite the continued presence of external lateral load. This constrained internal condition altered roller dynamics by limiting their ability to move, skew, or translate laterally within the bearing assembly.

The applied lateral load did not appear to have a marked effect on the vibration response of the healthy bearing, but it did affect vibration levels within the defective bearing. Vibration measurements showed that the healthy bearing maintained stable vibration levels under simulated curve negotiation, with only minor fluctuations that did not indicate damage,

instability, or defect initiation. In contrast, the defective bearing exhibited changes in vibration response under lateral loading conditions, particularly at higher speeds and higher L/V ratios. The application of the lateral load restricted the space available for roller motion and appeared to enhance roller interaction with the defective region within the bearing.

Post-test inspection and spall growth evaluation indicated that lateral loading did not significantly accelerate defect propagation. Based on the calculated spall area growth ratio and spall area growth rate, the measured spall propagation remained consistent with expected defect growth trends associated with normal bearing operation rather than being amplified by the simulated curve-negotiation conditions.

Overall, the findings of this research provide improved insight into the thermal, mechanical, and dynamic response of railroad tapered roller bearings subjected to lateral loading. The results highlighted the importance of considering lateral forces when interpreting bearing temperature behavior, particularly for condition-monitoring systems such as hot bearing detectors. Although lateral loading measurably altered temperature response and defect-related vibration behavior, it did not, under the present laboratory conditions, provide evidence of accelerated spall growth. These findings provided a foundation for future work involving alternative loading directions, extended-duration testing, and correlation with field operating conditions.

REFERENCES

[1] Shahidi, Parham et al. “Estimation of Bogie Performance Criteria Through On-Board Condition Monitoring.” *Annual Conference of the PHM Society* (2014): n. page.

[2] J. D. Lima, *Residual Service Life Prognostic Models for Tapered Roller Bearings*, Master’s Thesis, Dept. of Mechanical Engineering, Univ. of Texas Rio Grande Valley, 2020.

[3] Tarawneh, C., Koester, L., Fuller, A. J., Wilson, B. M., and Turner, J. A. (2012), “Service Life Testing of Components with Defects in the Rolling Contact Fatigue Zone,” ASTM International, STP 1548, West Conshohocken, PA, pp 67-83.

[4] Goshima, T., Ishihar, S., Shimizu, M., and Mizoguchi, A. (2010), “Crack Propagation and Initiation Lives for Surface Pitting Due to Rolling/Sliding Contact,” Journal of Thermal Stresses, 33(11), pp 1087-1106. DOI: 10.1080/01495739.2010.511917

[5] Nikas, G. K. (2016), “Algebraic Equations for the Pile-Up Geometry in Debris Particle Indentation of Rolling Elastohydrodynamic Contacts,” ASME Journal of Tribology, 138(2), 021503. DOI: 10.1115/1.4031516

[6] U.S. Department of Transportation, *Train Accidents by Type and Rates*, Federal Railroad Administration Office of Safety, [Online]. Available: https://safetydata.fra.dot.gov/officeofsafety/publicsite/query/TrainAccidentsFYCYWithRates.aspx.

[7] Tarawneh, C. M., Wilson, B. M., & Martin, A. (2013). Statistical investigation of wayside hot-box detector data. *International Journal of Railway Technology*, 2(3), 1–16

[8] Tarawneh, C. M., Estrada, R., Wilson, B. M., & Martin, A. (2014). Field implementation statistical analysis of an emerging bearing condition monitoring system. In J. Pombo (Ed.), Proceedings of the Second International Conference on Railway Technology: Research, Development and Maintenance. Civil-Comp Press

[9] R. H. Cantwell, “Bearings Down on Bearings”, *Railway Age,* Mar. 15, 2024. https://www.railwayage.com/mechanical/freight-cars/bearing-down-on-bearings/#.

[10] Association of American Railroads, "Freight Railroads Announce Key Safety Measures in Drive to Zero Accidents," *Association of American Railroads*, Mar. 8, 2023. [Online]. Available: https://www.aar.org/news/freight-railroads-announce-key-safety-measures-in-drive-to-zero-accidents/.

[11] Ose, Mixanikos. "Heat Detectors-box and Brake Disc (Hot Box & Hot Wheel Detection System)." Heat Detectors-box and Brake Disc (Hot Box & Hot Wheel Detection System). N.p., 16 July 2015. Web.

[12] H. Wang, T. F. Conry, and C. Cusano, 1996, "Effects of Cone/Axle Rubbing Due to Roller Bearing Seizure on the Thermomechanical Behavior of a Railroad Axle," *Journal of Tribology*, vol. 118, no. 2, pp. 311-319.

[13] C. M. Tarawneh, L. Sotelo, A. A. Villarreal, N. de los Santos, R. L. Lechtenberg, and R. Jones, "Temperature profiles of railroad tapered roller bearings with defective inner and outer rings," in *Proc. ASME Joint Rail Conf. (JRC)*, Columbia, SC, USA, Apr. 2016, pp. V001T01A004. doi: 10.1115/JRC2016-5816.

[14] Tarawneh, C. (2024). *Historical Implications of Wayside Detector Systems and their Ability to Detect Hot Bearing Derailments* (Paper No. JRC2024-125389). In *Proceedings of the 2024 Joint Rail Conference (JRC 2024)*. The American Society of Mechanical Engineers

[15] Marketing, Nuthouse. "Advanced Rail Engineering." Etion Digitise, www.ansysrail.co.za/trackside-solutions/.

[16] M. Stewart, E. Flynn, B. P. Marquis, and Sharma & Associates, Department of Transportation. Federal Railroad Administration. "An Implementation Guide for Wayside Detector Systems," Washington, DC, United States, May 2019.

[17] U.S. Government. (n.d.). 49 CFR § 213.110: Gage restraint measurement systems. Code of Federal Regulations. Retrieved November 18, 2025

[18] Matsumoto, A., Sato, Y., Ohno, H., Shimizu, M., Kurihara, J., Tomeoka, M., … Mizuno, M. (2012). Continuous observation of wheel/rail contact forces in curved track and theoretical considerations. Vehicle System Dynamics, 50(sup1).

[19] Elkins, J. A. (1993). Testing and analysis techniques for safety assessment of rail vehicles: The state of the art. Vehicle System Dynamics, 22(3-4), 185-208

[20] Yao, Y., Wu, G., Sardahi, Y., & Sun, J. Q. (2018). Hunting stability analysis of high-speed train bogie under the frame lateral vibration active control. *Vehicle System Dynamics*, *56*(2), 297–318. https://doi.org/10.1080/00423114.2017.1375128

[21] Matsumoto, A., Sato, Y., Ohno, H., Shimizu, M., Kurihara, J., Tomeoka, M., … Mizuno, M. (2012). Continuous observation of wheel/rail contact forces in curved track and theoretical considerations. *Vehicle System Dynamics*, *50*(sup1).

[22] Hook, J. G. (2025, January 24). *Fundamentals of Railway Curve Superelevation: With explanation of curve radius and degree of curve* [PDF]. JGH Tech

[23] Cotey, A. (2011, January 1). *Measuring track curvature*. Trains Magazine. Retrieved November 18, 2025

[24] MxV Rail. (2024, October 1). *Moving forward in rail innovation with MxV Rail's new test tracks*. MxV Rail. Retrieved November 18, 2025,

[25] Patowary, K. (2016, December 1). *Tehachapi Loop*. Amusing Planet. Retrieved November 12, 2025

[26] Kravets, V.V., Kravets, T.V. Evaluation of the centrifugal, coriolis, and gyroscopic forces on a railroad vehicle moving at high speed. *Int Appl Mech* 44, 101–109 (2008). https://doi.org/10.1007/s10778-008-0024-3

[27] Stickels, C.A. Carbide refining heat treatments for 52100 bearing steel. *Metall Trans* **5**, 865–874 (1974). https://doi.org/10.1007/BF02643140

[28] Tarawneh, C. M., de los Santos, N., Sotelo, L., Lechtenberg, R. L., Villarreal, A. A., & Jones, R. (2016). Temperature Profiles of Railroad Tapered Roller Bearings with Defective Inner and Outer Rings. *Proceedings of the 2016 Joint Rail Conference*. April 12-15, 2016, Columbia, SC, USA. JRC2016-5816

[29] Predikto. N.p.: Predikto, n.d. Predicting Hot Box Detector Failures. Predikto, 2015.

[30] Culver, C. (n.d.). *Tapered roller bearing rib-roller end scoring damage in aircraft landing wheels* (Tech. Paper No. 11786). The Timken Company. Retrieved November 18, 2025

[31] De Los Santos, N. (2019). Development of prognostic techniques for surface defect growth in railroad bearing rolling elements (Master's thesis). The University of Texas Rio Grande Valley.

APPENDIX A

APPENDIX A

FEA LINEAR BEARING, FRONT AND REAR RAM

FEA-Linear Bearing

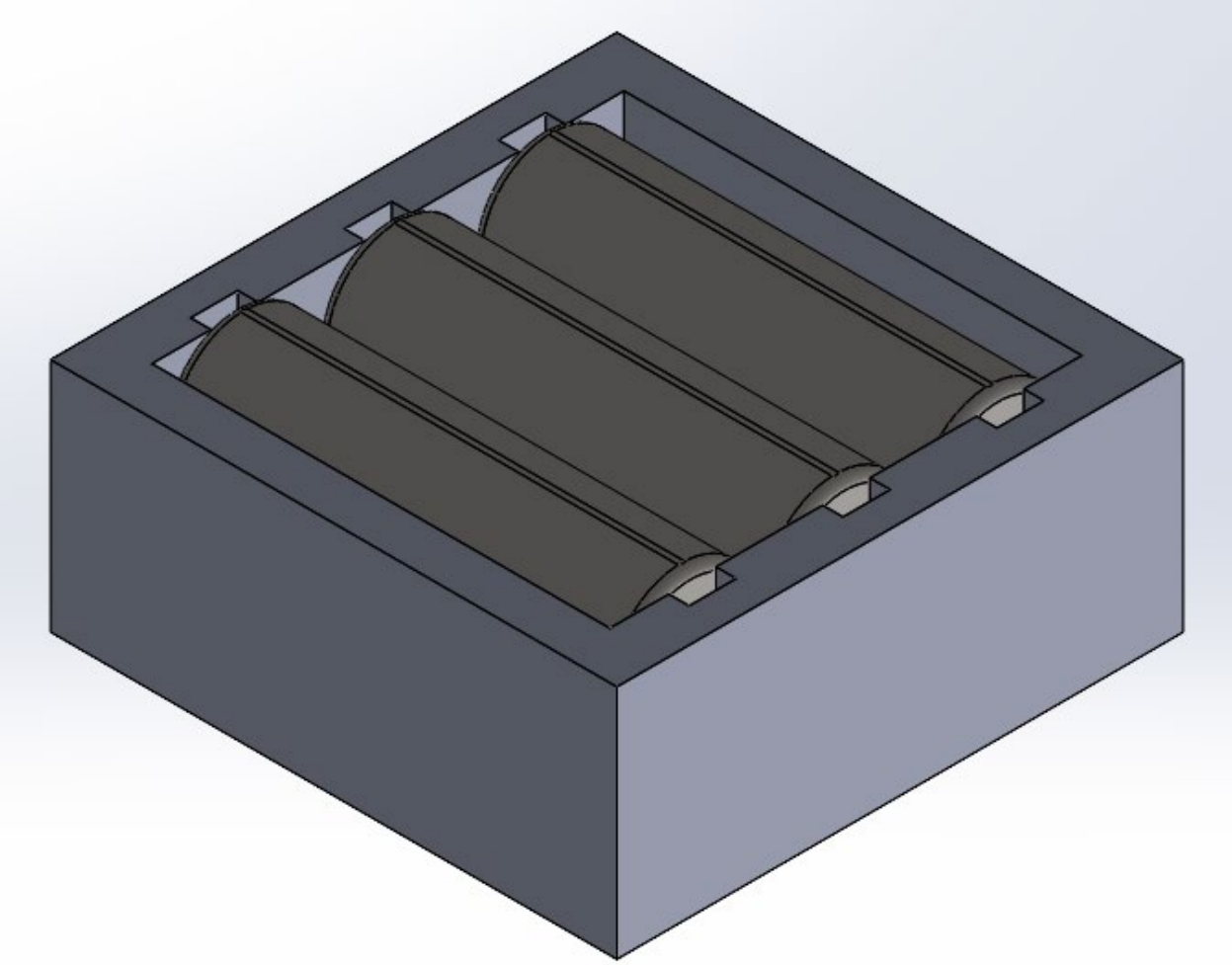

Figure 39. Linear bearing SolidWorks design

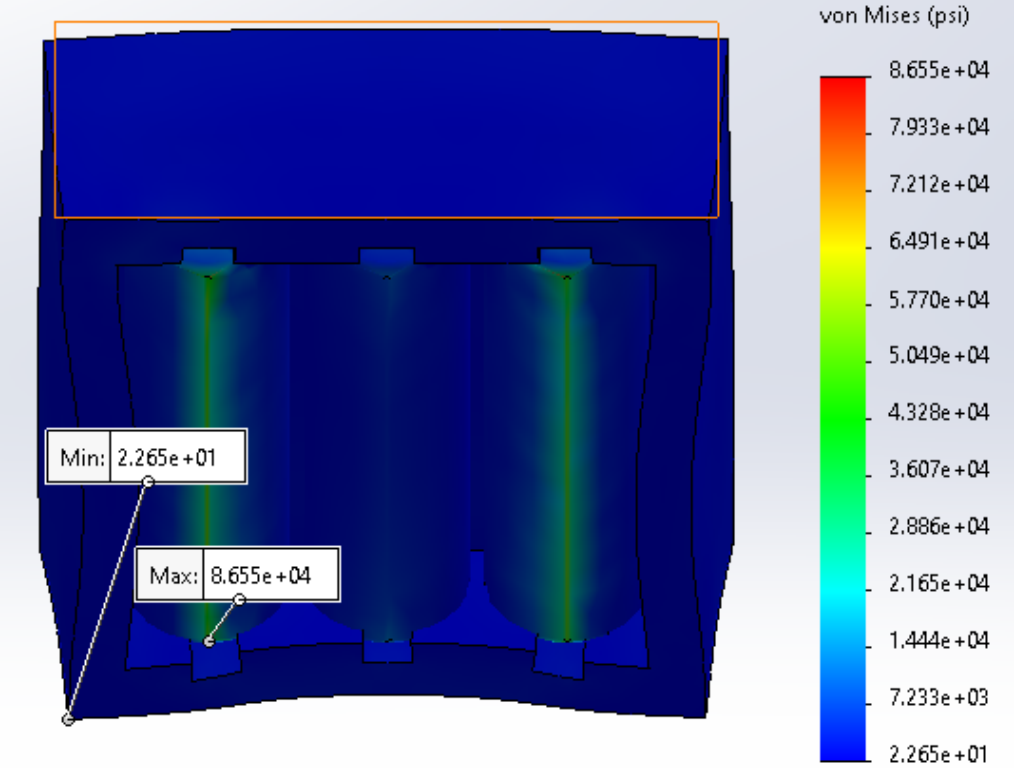

Figure 40. FEA linear bearing- stress (von Mises (psi))

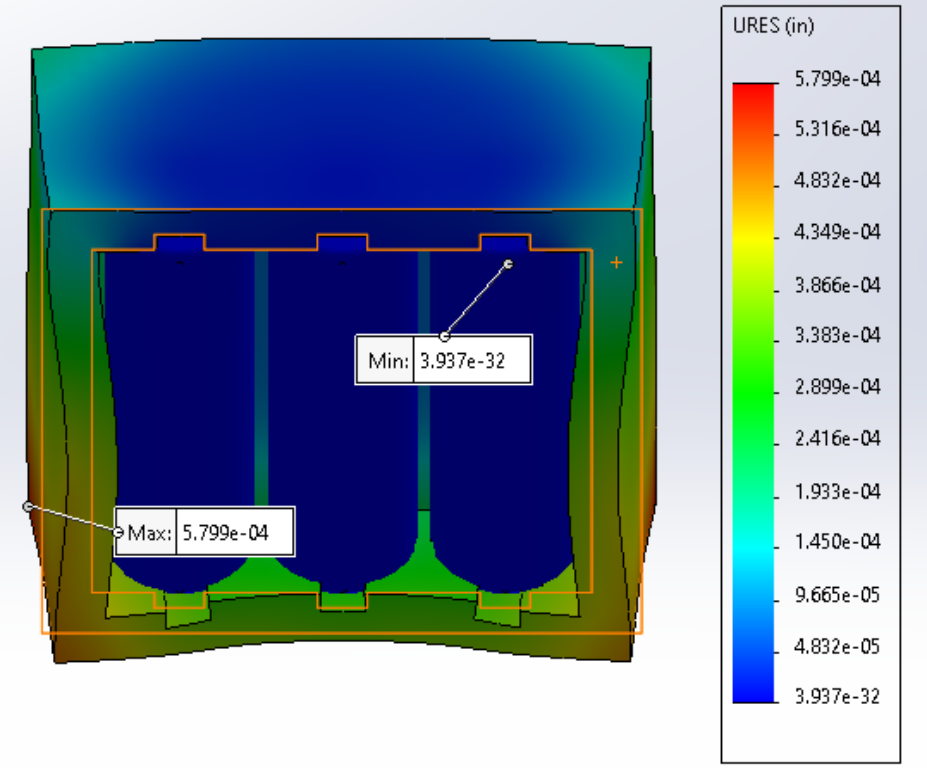

Figure 41. FEA linear bearing-displacement (in)

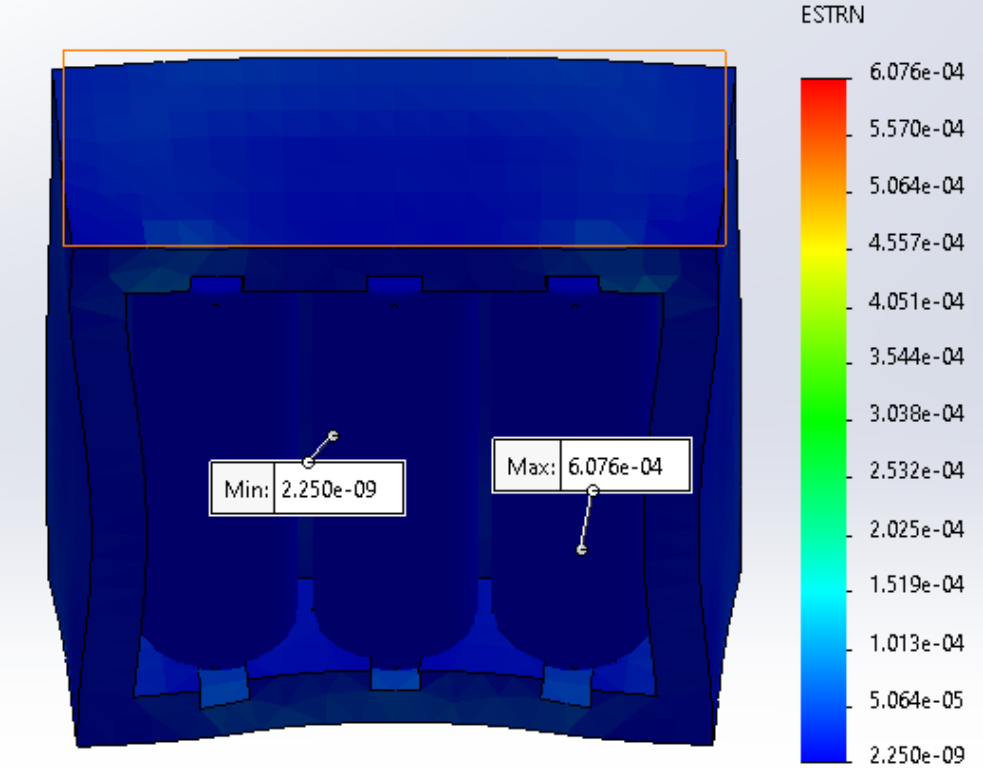

Figure 42. FEA linear bearing-strain

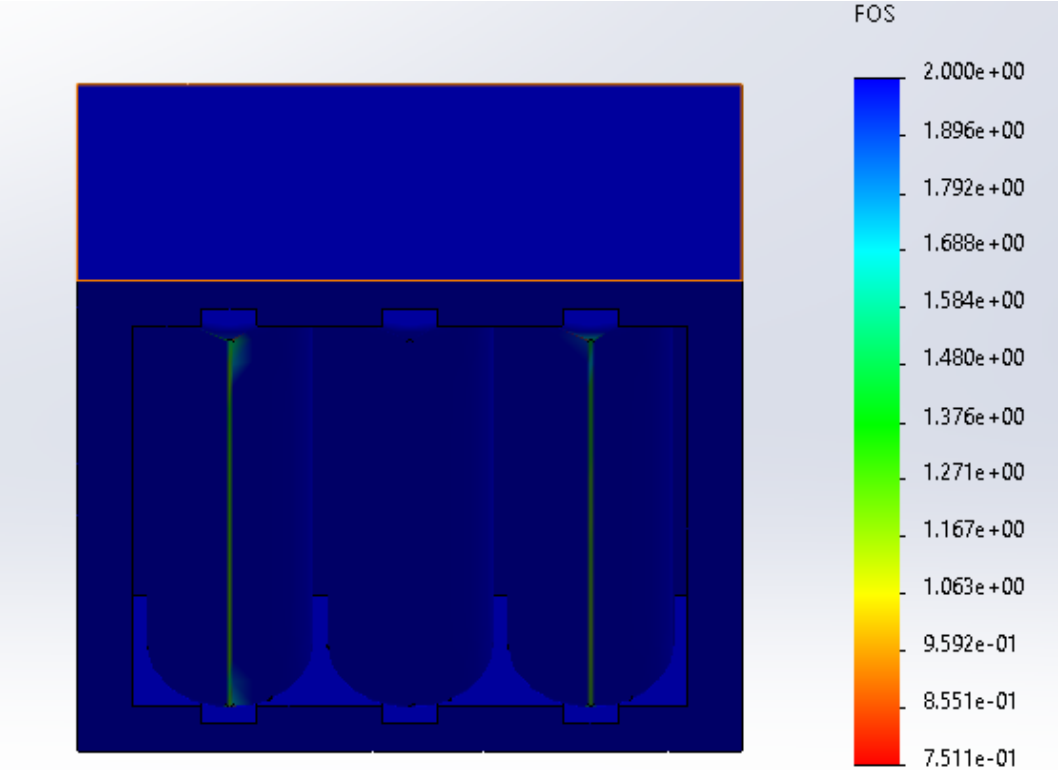

Figure 43. FEA linear bearing-Factor of Safety

FEA-Front Ram

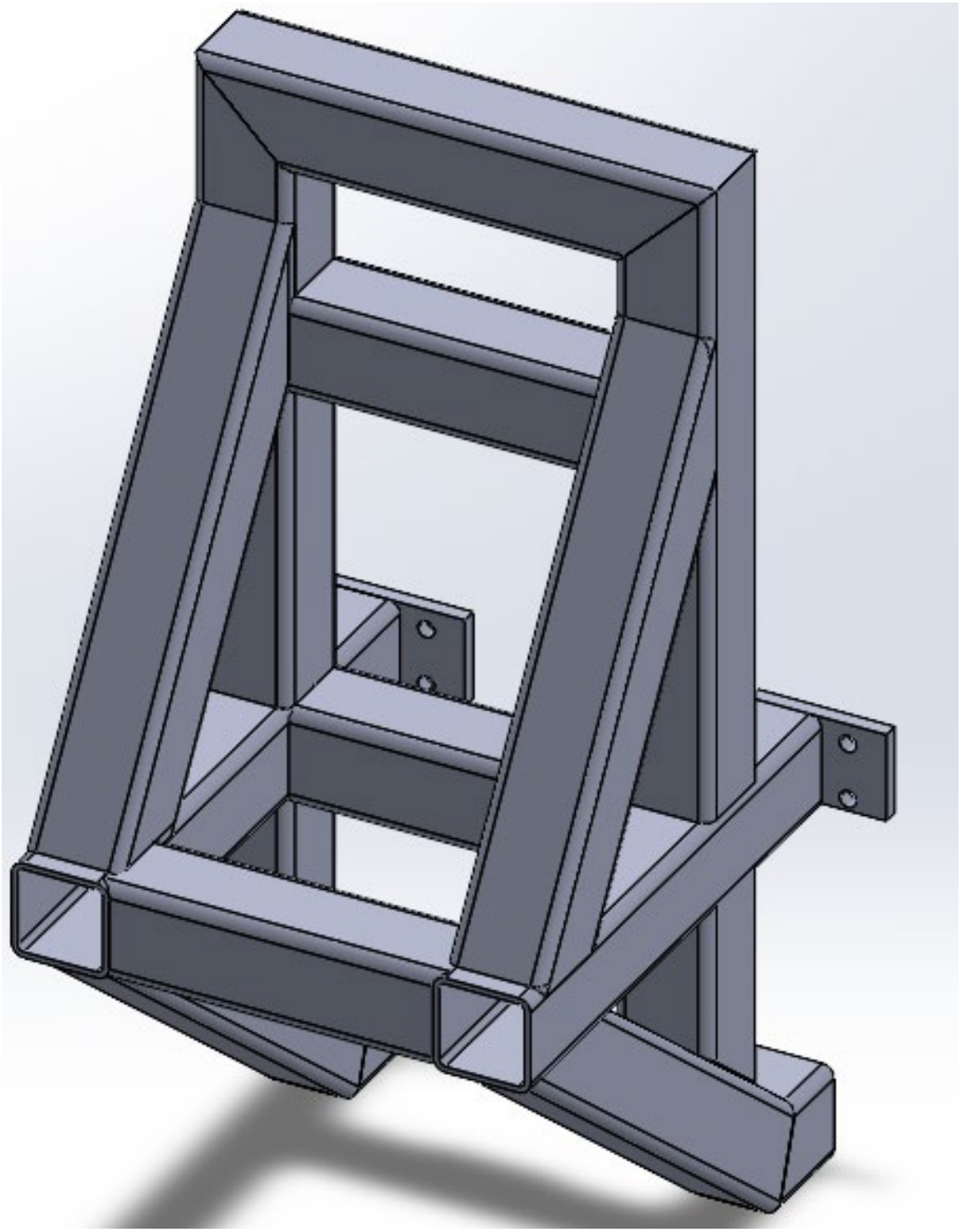

Figure 44. Front ram SolidWorks design

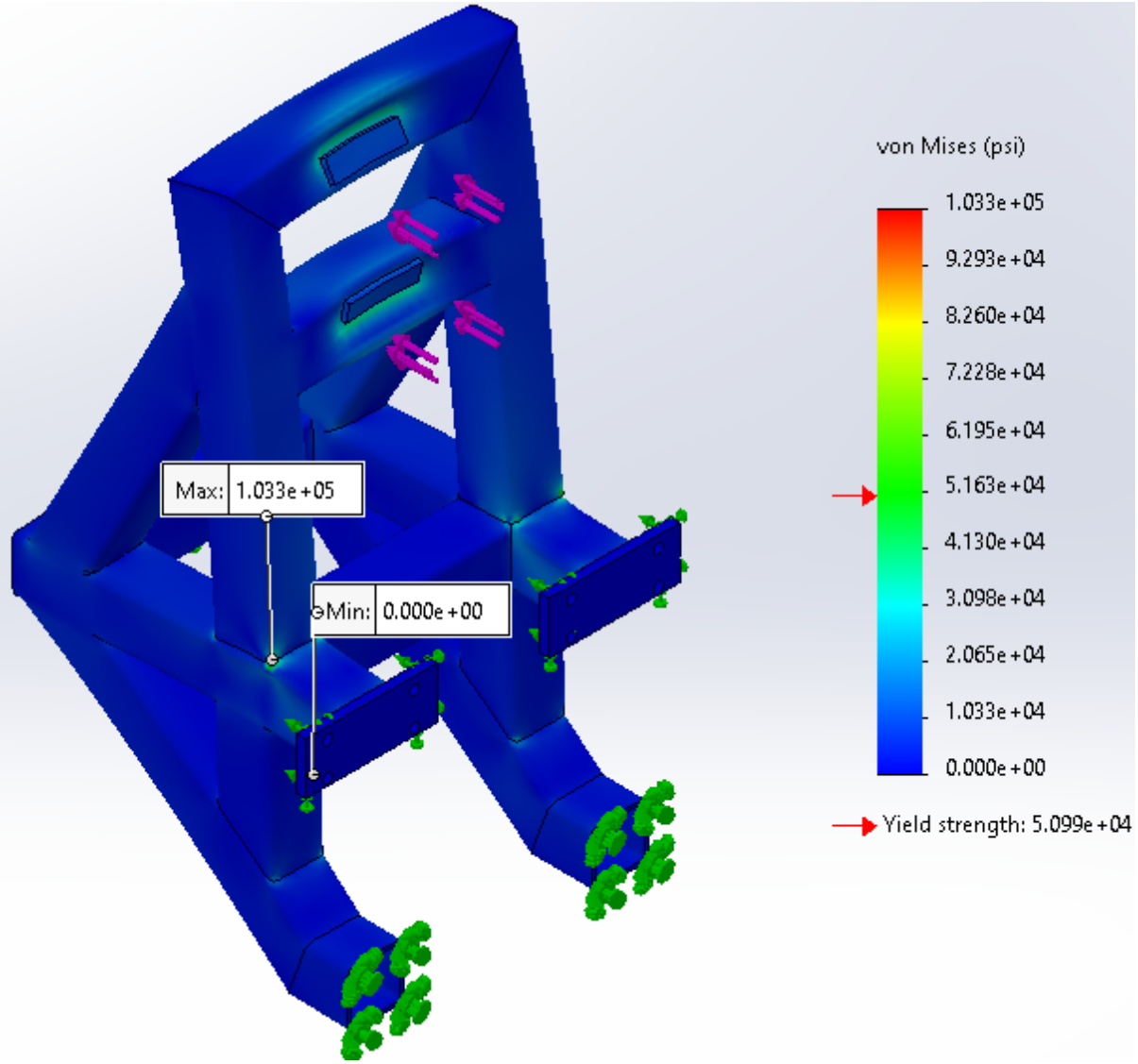

Figure 45. FEA front ram- stress (von Mises (psi)

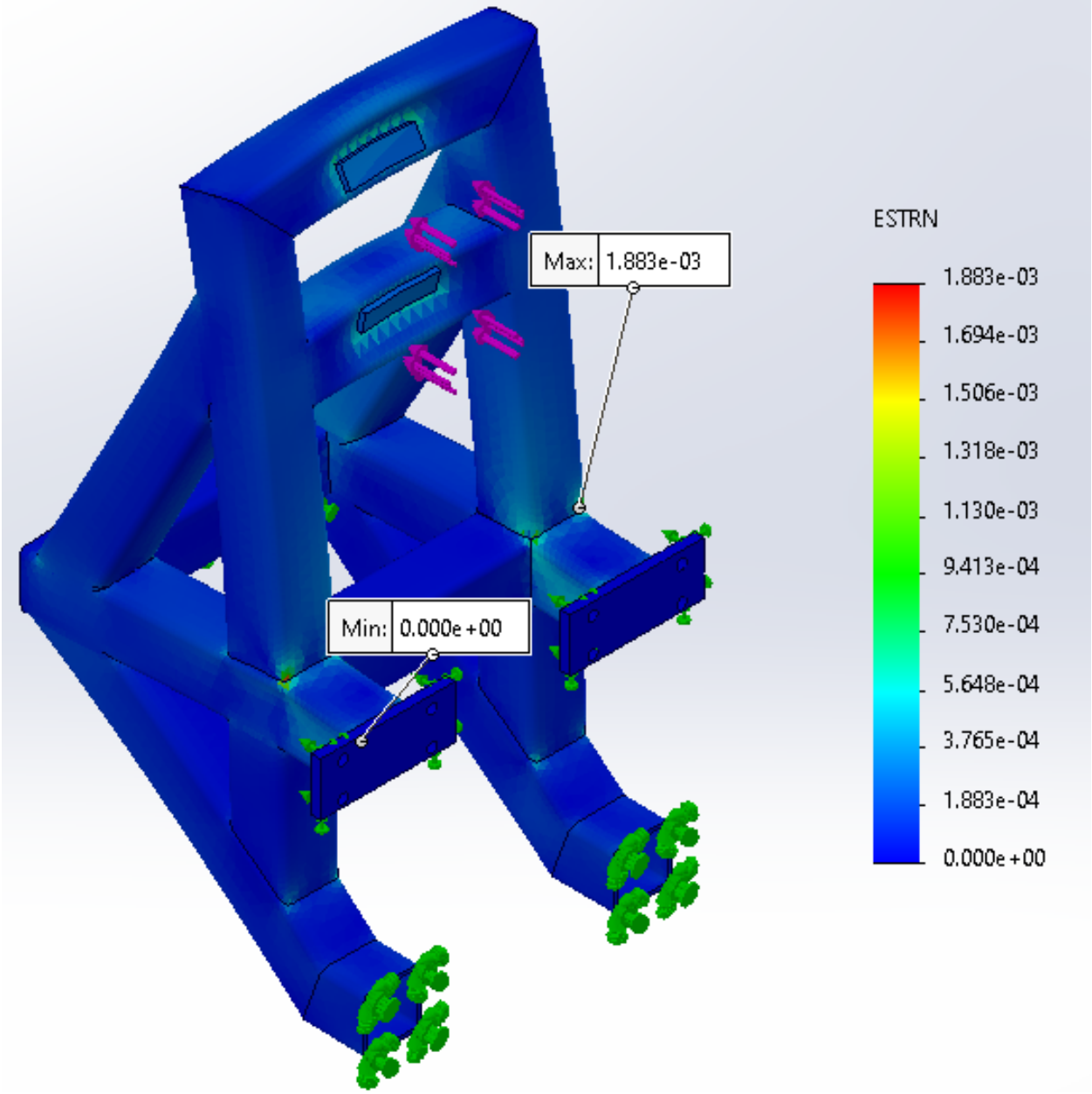

Figure 46. FEA front ram-displacement (in)

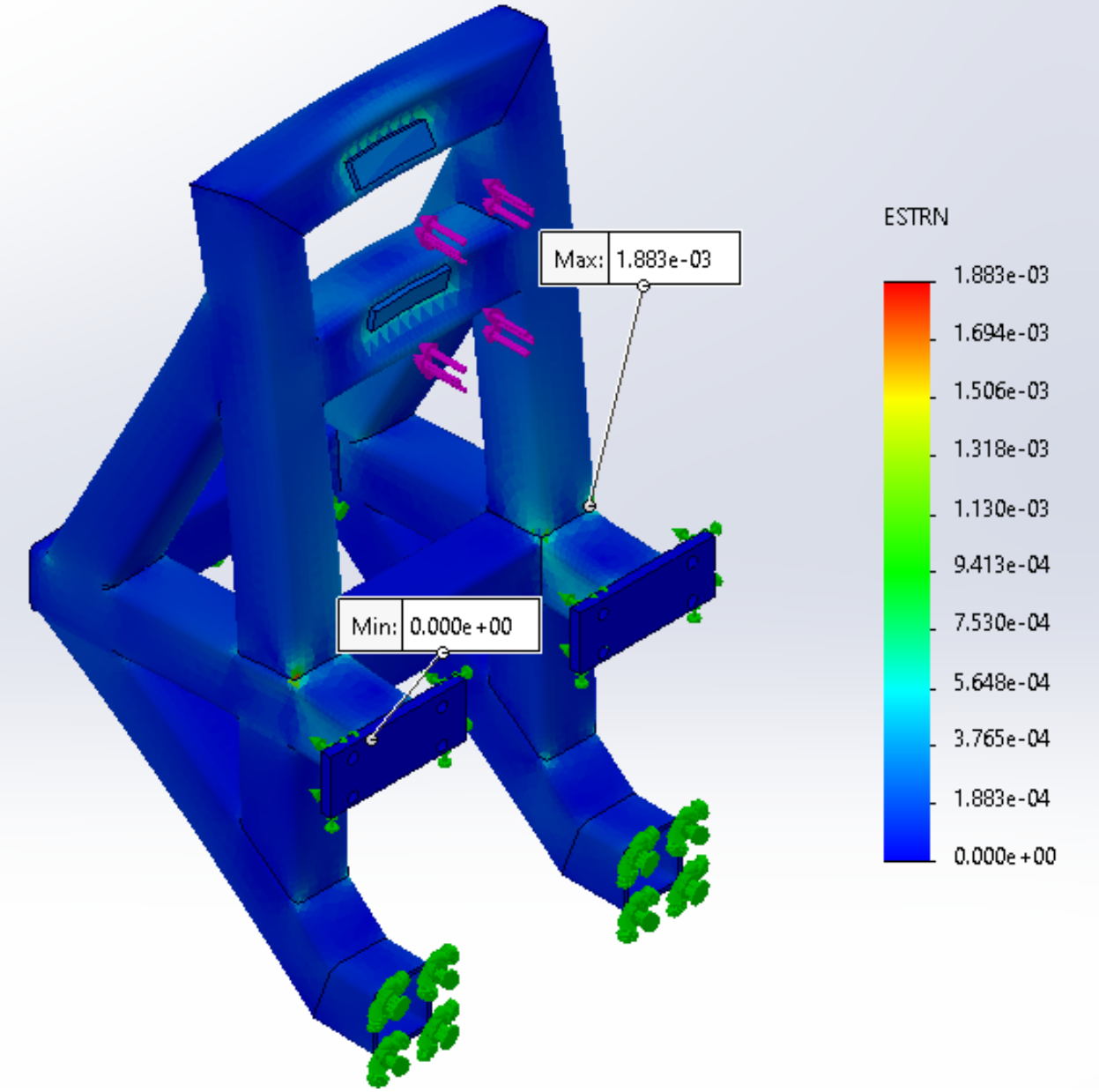

Figure 47. FEA front ram-strain

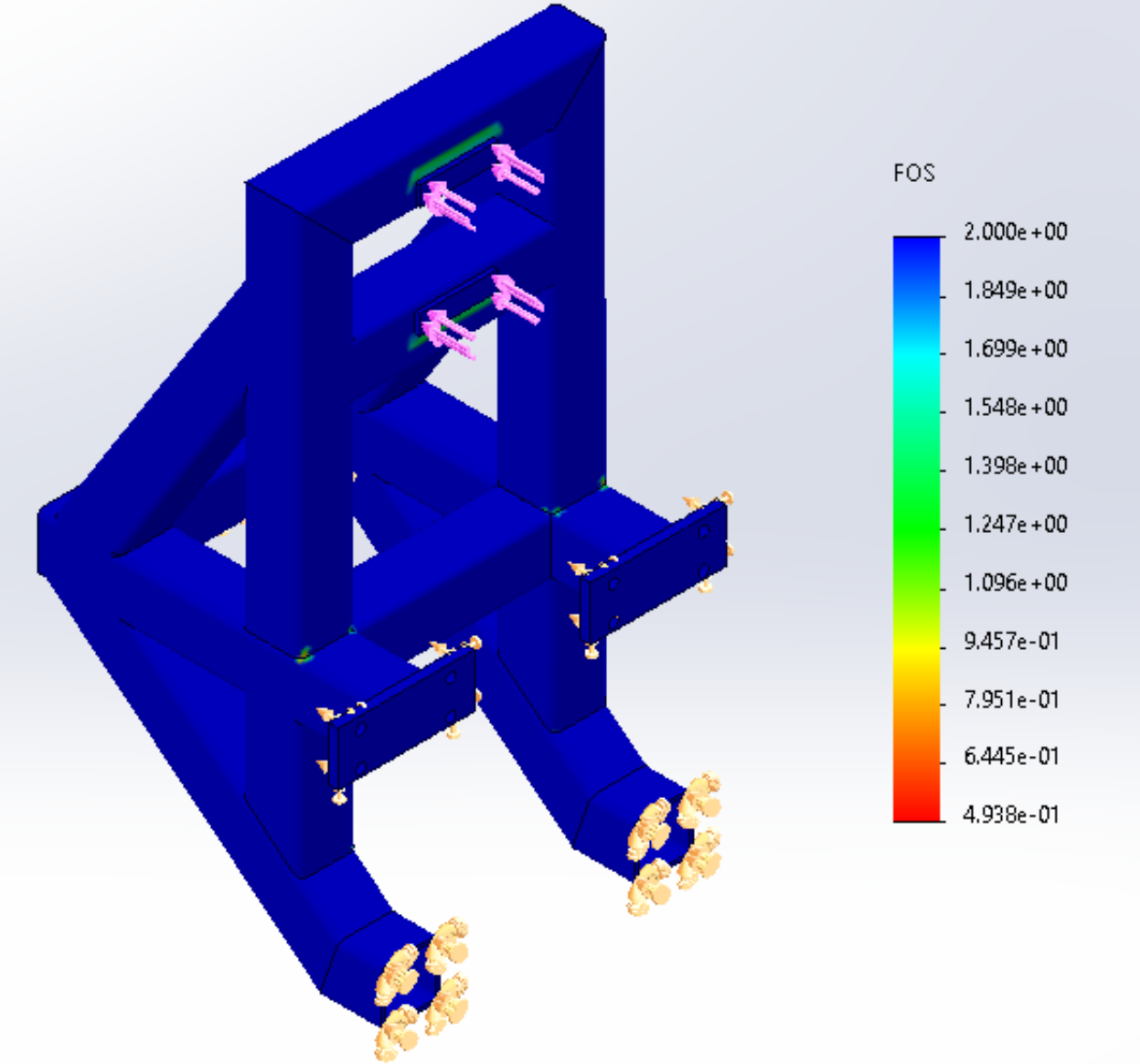

Figure 48. FEA front ram-Factor of Safety

FEA-Rear Ram

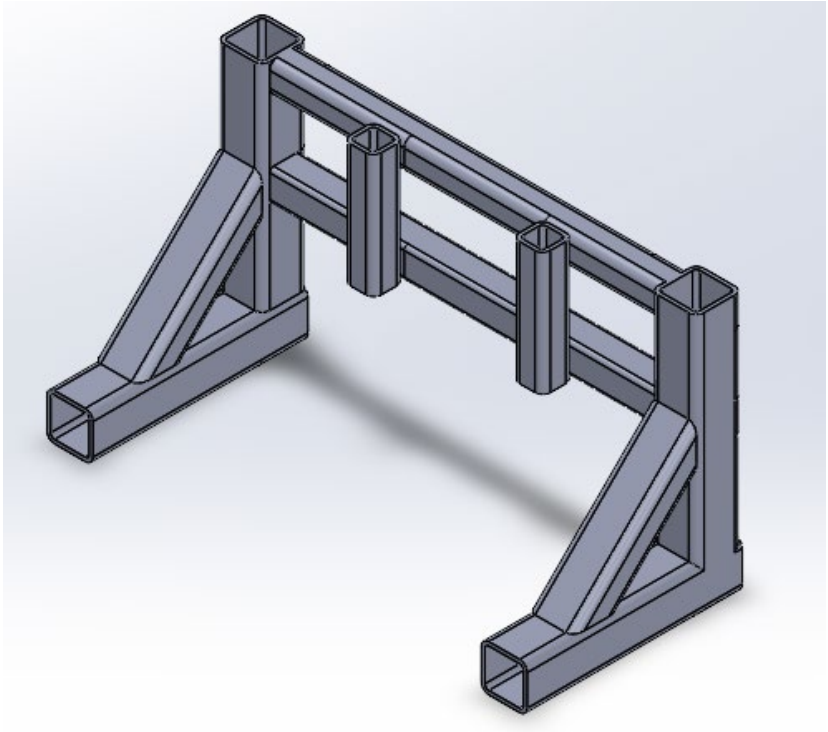

Figure 49. Rear ram SolidWorks design

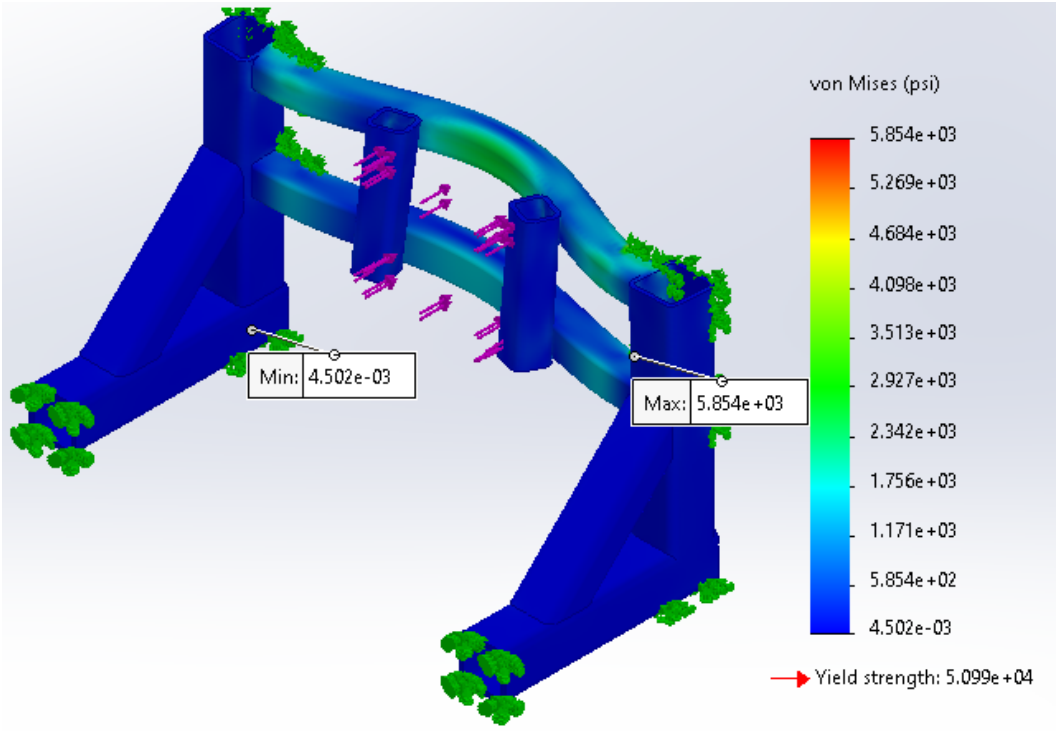

Figure 50. FEA rear ram - stress (von Mises (psi))

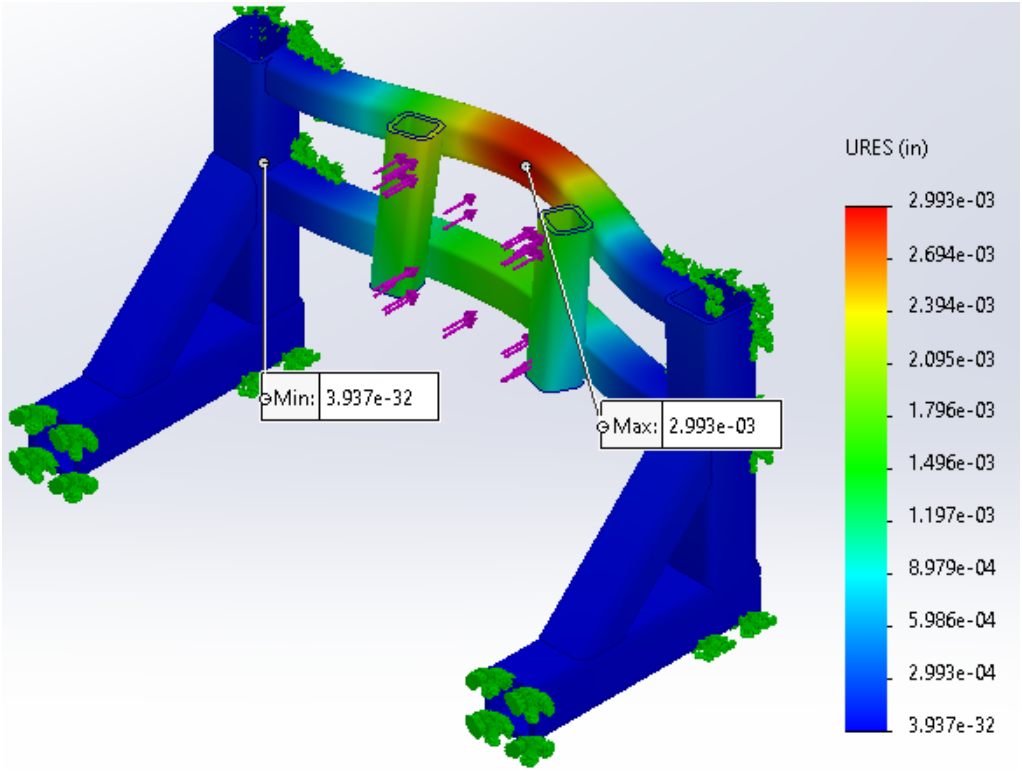

Figure 51. FEA rear ram-displacement (in)

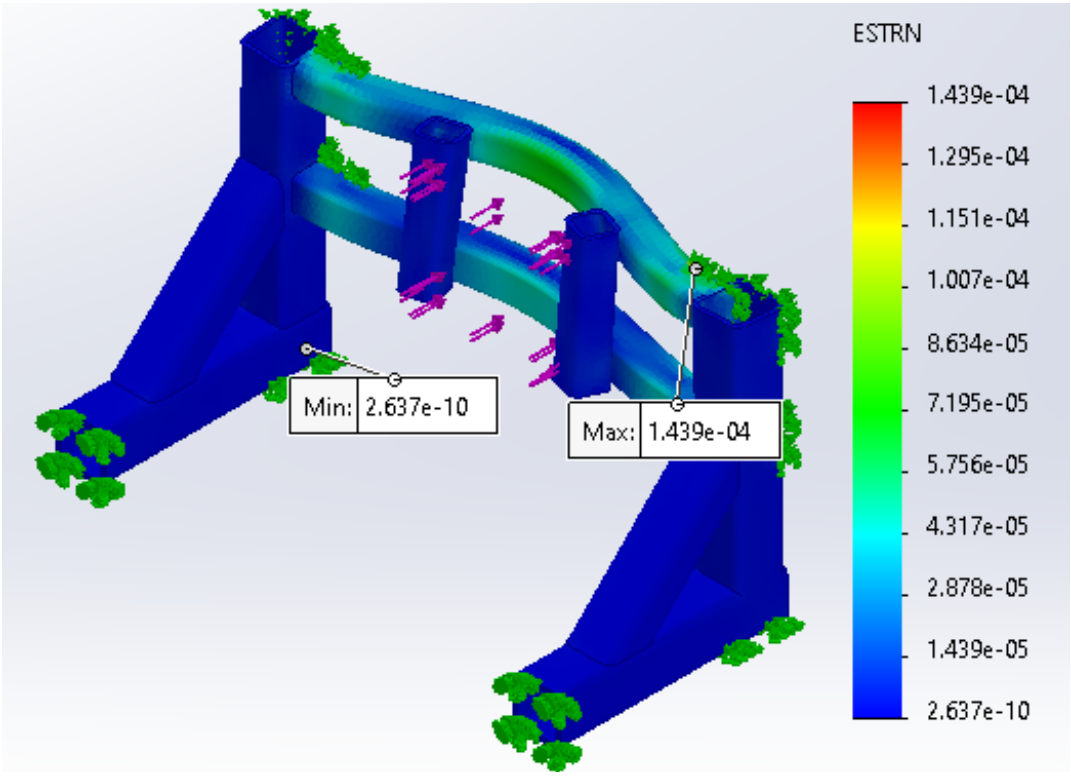

Figure 52. FEA rear ram-strain

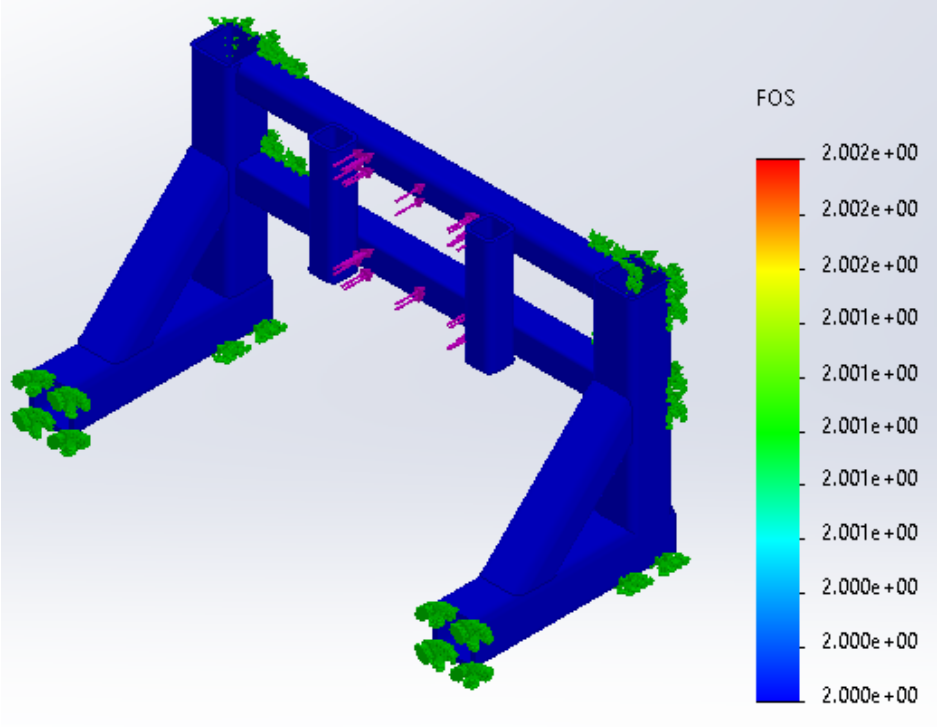

Figure 53. FEA rear ram-Factor of Safety

APPENDIX B

APPENDIX B

HEALTHY BEARING LATERAL LOADING CASES

Effects of Lateral Load at 97 kph (60 mph) and Unloaded Railcar

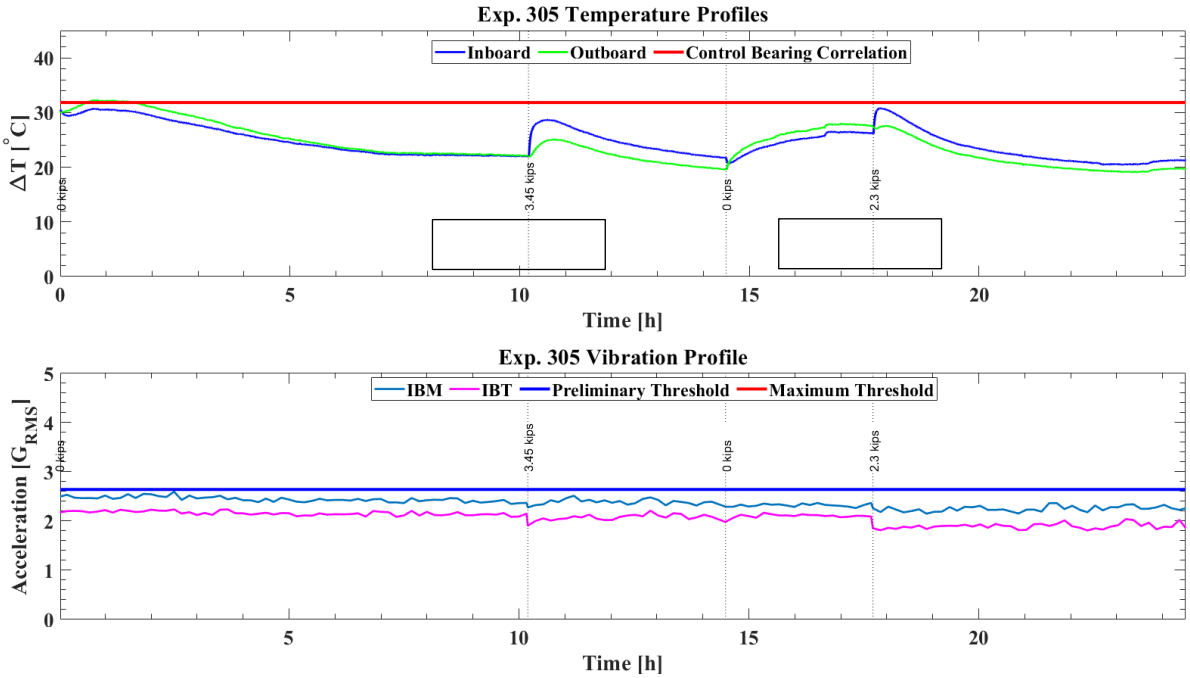

Figure 54. Control bearing temperature and acceleration at 97 kph (60 mph) and 17% load (empty railcar) with varying lateral loads

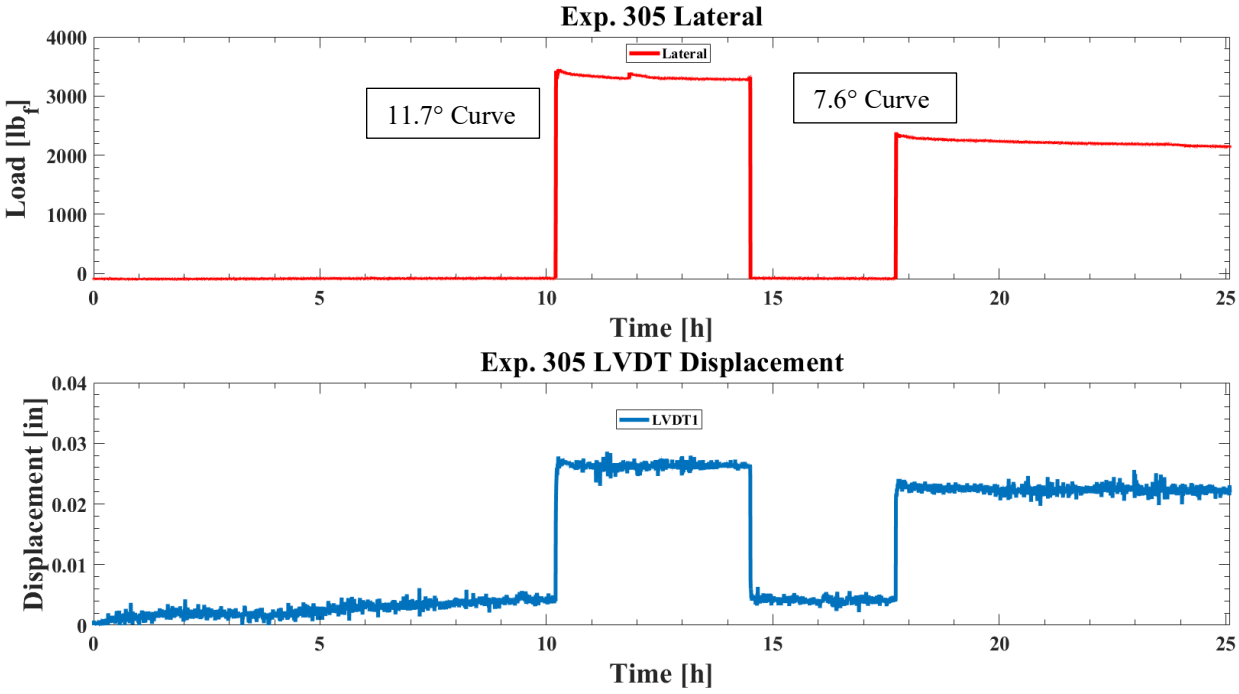

Figure 55. Control bearing lat. load and disp., 97 kph (60 mph) and 17% load (empty railcar) with varying lateral loads

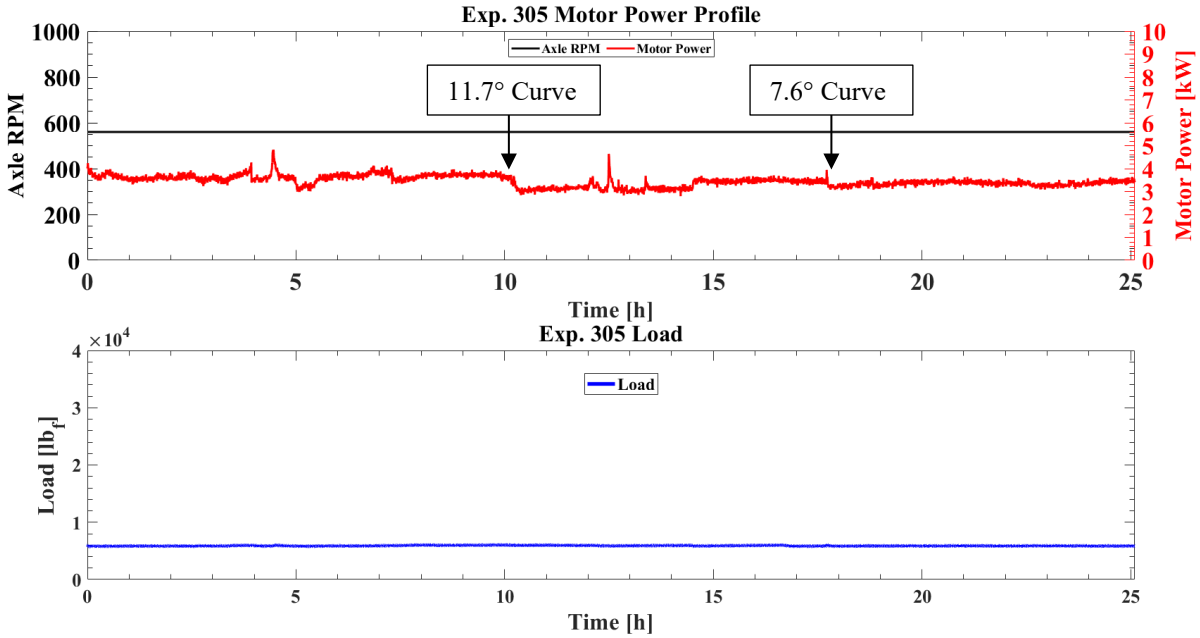

Figure 56. Control bearing power and vert. load, 97 kph (60 mph) and 17% load (empty railcar) with varying lateral loads

Table 10. Lateral response summary of a control bearing operating at 97 kph (60 mph) and 17% load (empty railcar)

F_{lat} [kN] / [kips]	Max ΔT [ºC] / [ºF]	Avg. ΔT [ºC] / [ºF]	Accel. [G_{RMS}]	Power [kW]	Disp. [mm] / [in]	ΔT / F_{lat} [ºC/kN] / [ºC/kips]
0	22.3 / 40.1	22.3 / 40.1	2.3	3.5	0.102 / 0.004	-
15.6 / 3.5	28.6 / 51.5	25.5 / 45.9	2.4	3.1	0.660 / 0.026	0.38 / 1.7
10.2 / 2.3	30.7 / 55.3	26.5 / 47.7	2.3	3.3	0.559 / 0.022	0.83 / 3.7

Effects of Lateral Load at 97 kph (60 mph) and Fully Loaded Railcar

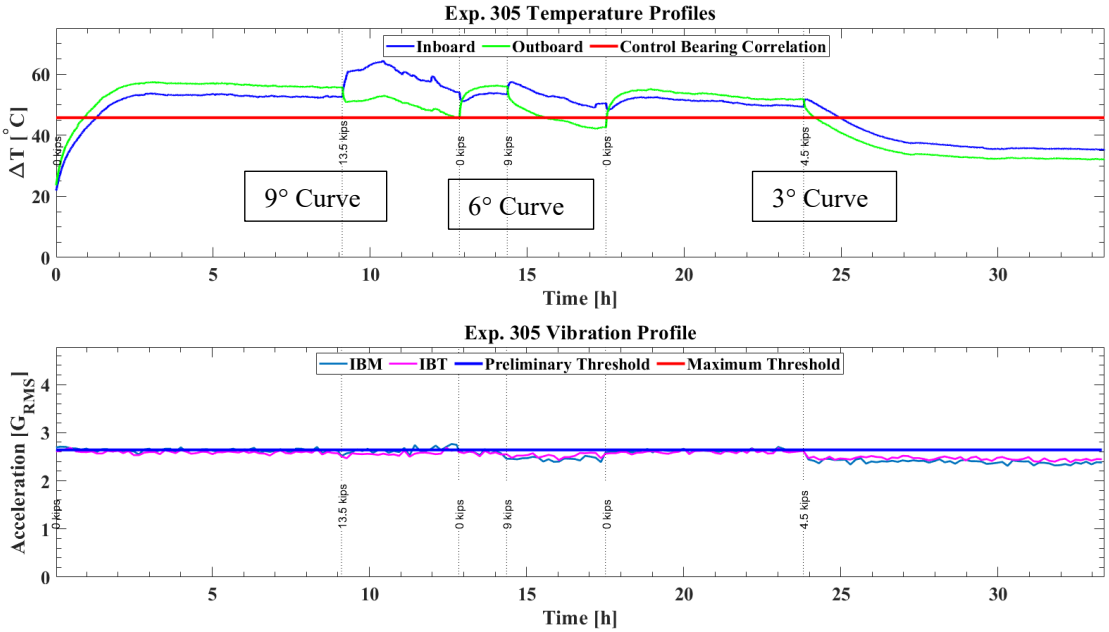

Figure 57. Control bearing temperature and acceleration at 97 kph (60 mph) for 100% load (fully loaded railcar) with varying lateral loads

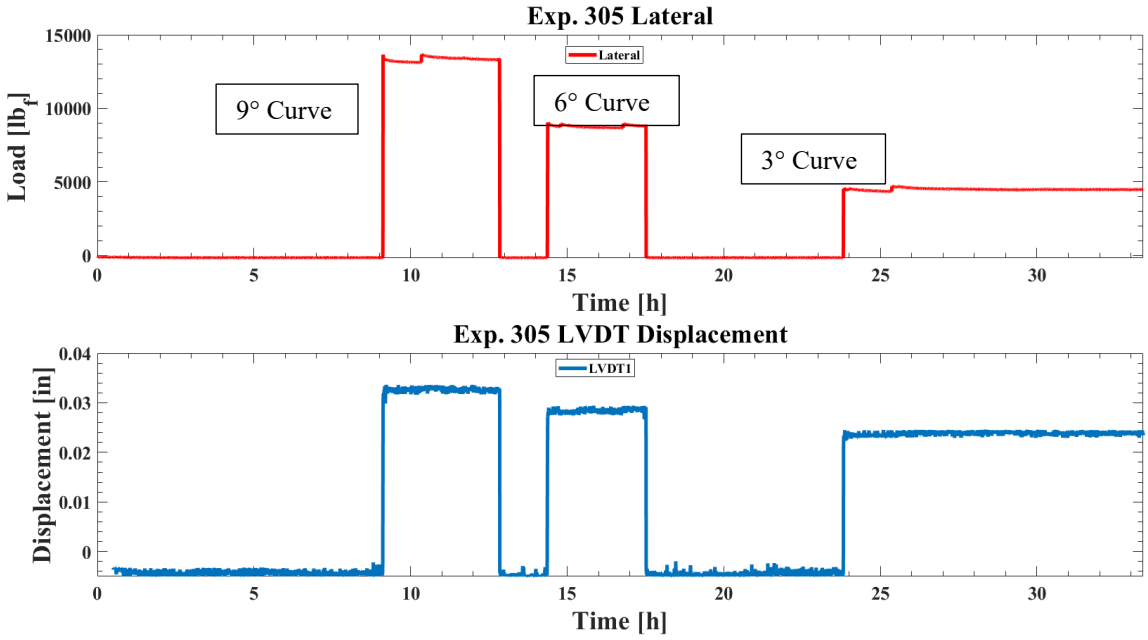

Figure 58. Control bearing lateral load and displacement at 97 kph (60 mph) for 100% load (fully loaded railcar) with varying lateral loads

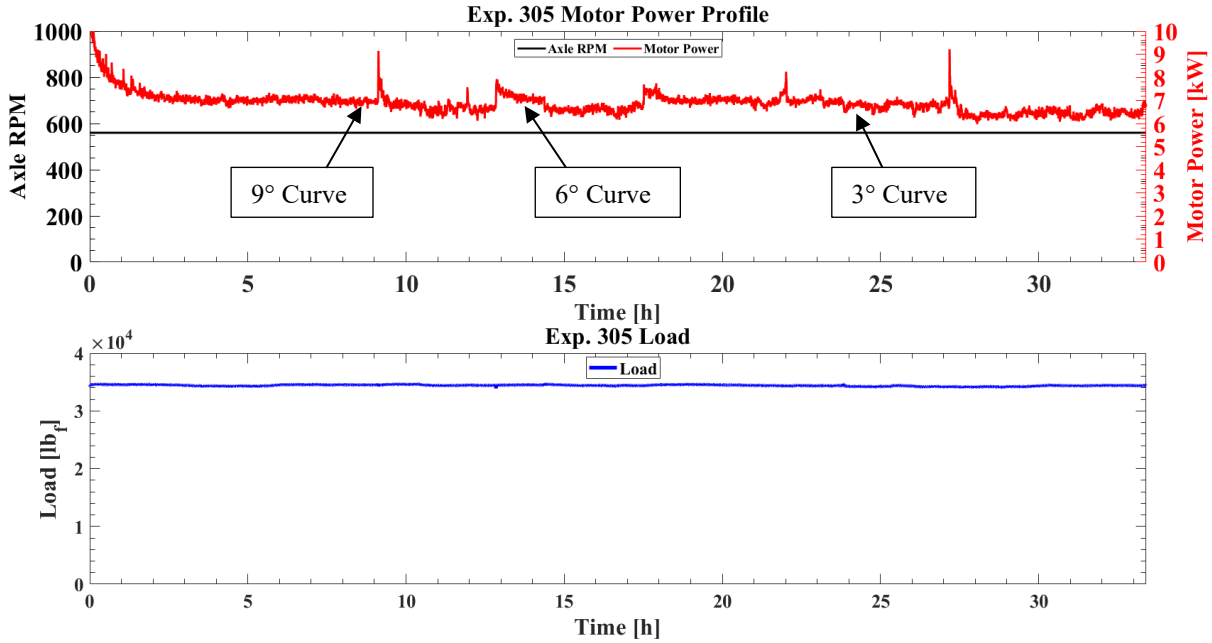

Figure 59. Control bearing motor power and vertical load at 97 kph (60 mph) for 100% load (fully loaded railcar) with varying lateral loads

Table 11. Lateral response summary of a control bearing operating at 97 kph (60 mph) for 100% load (fully loaded railcar)

F_{lat} [kN] / [kips]	Max ΔT [°C] / [°F]	Avg. ΔT [°C] / [°F]	Accel. [G_{RMS}]	Power [kW]	Disp. [mm] / [in]	ΔT / F_{lat} [°C/kN] / [°C/kips]
0	56 / 100.8	56 / 100.8	2.6	7.1	-0.102 / -0.004	-
60.1 / 13.5	64 / 115.2	60 / 108.0	2.6	6.8	0.762 / 0.030	0.13 / 0.6
40.0 / 9	57.5 / 103.5	56.8 / 102.2	2.5	7.1	0.711 / 0.028	0.04 / 0.2
20.0 / 4.5	51.5 / 92.7	53.8 / 96.8	2.3	6.8	0.584 / 0.023	-0.22 / -1.0

Effects of Lateral Load at 40 kph (25 mph) and Fully Loaded Railcar

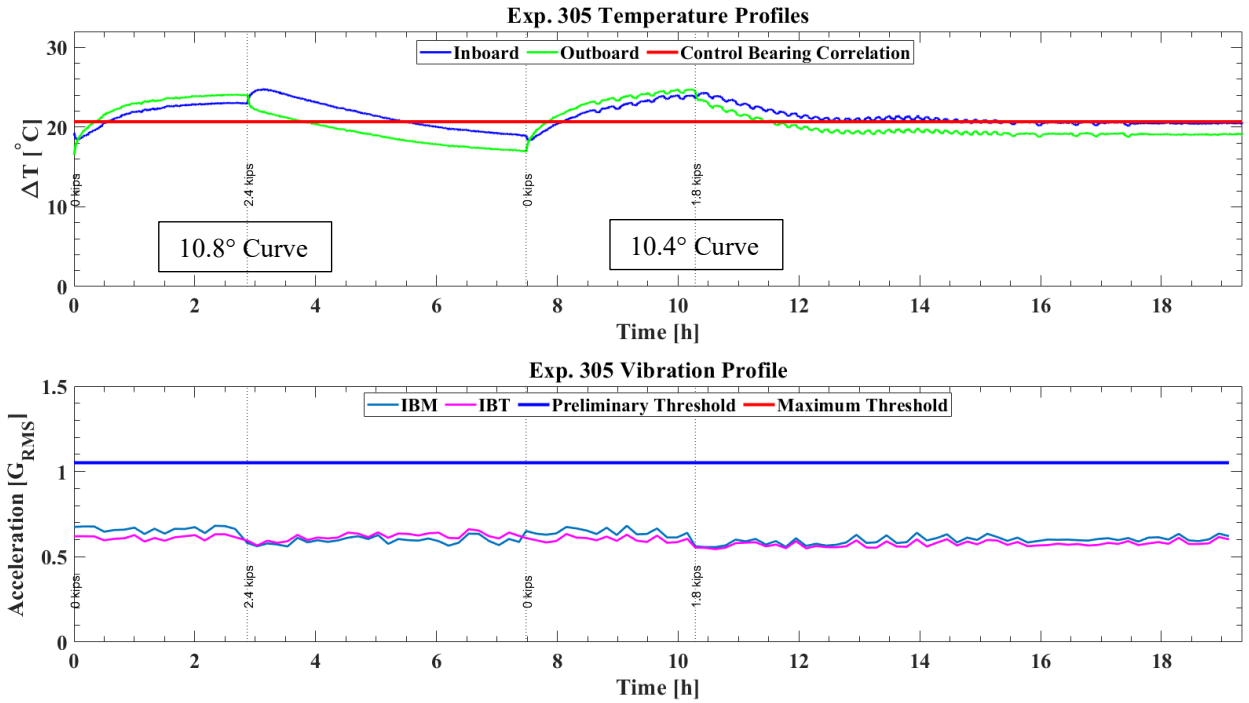

Figure 60. Control bearing temperature and acceleration at 40 kph (25 mph) for 100% load (fully loaded railcar) with varying lateral loads

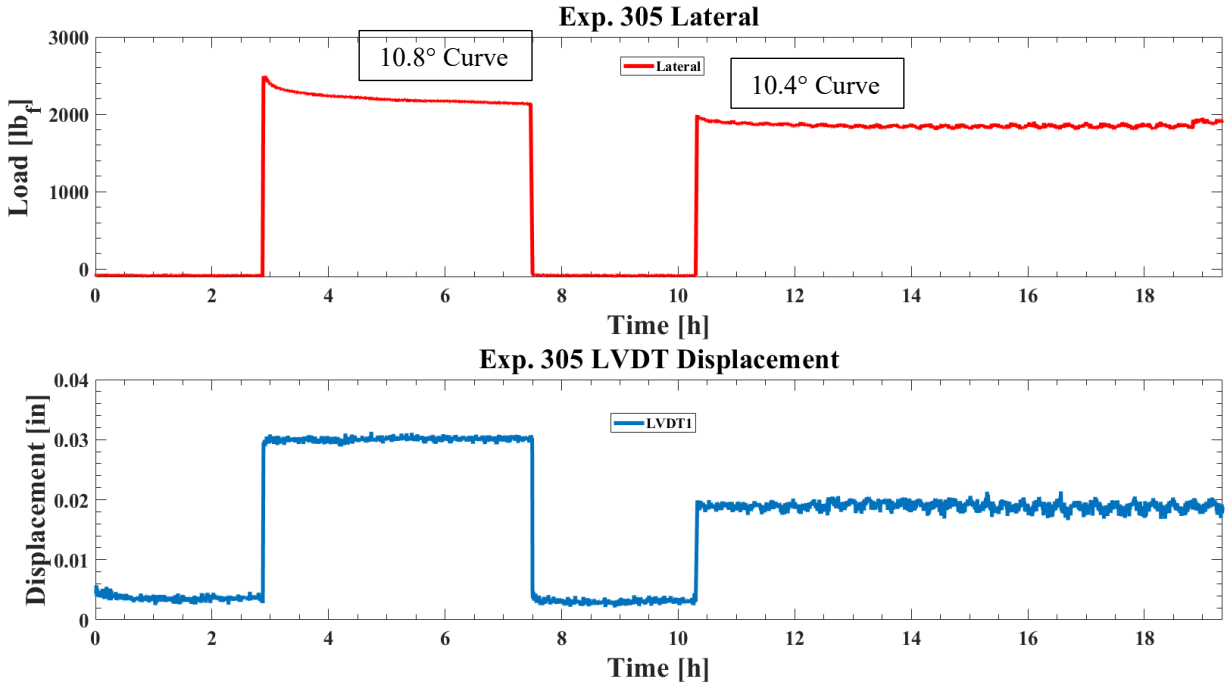

Figure 61. Control bearing lateral load and displacement at 40 kph (25 mph) for 100% load (fully loaded railcar) with varying lateral loads

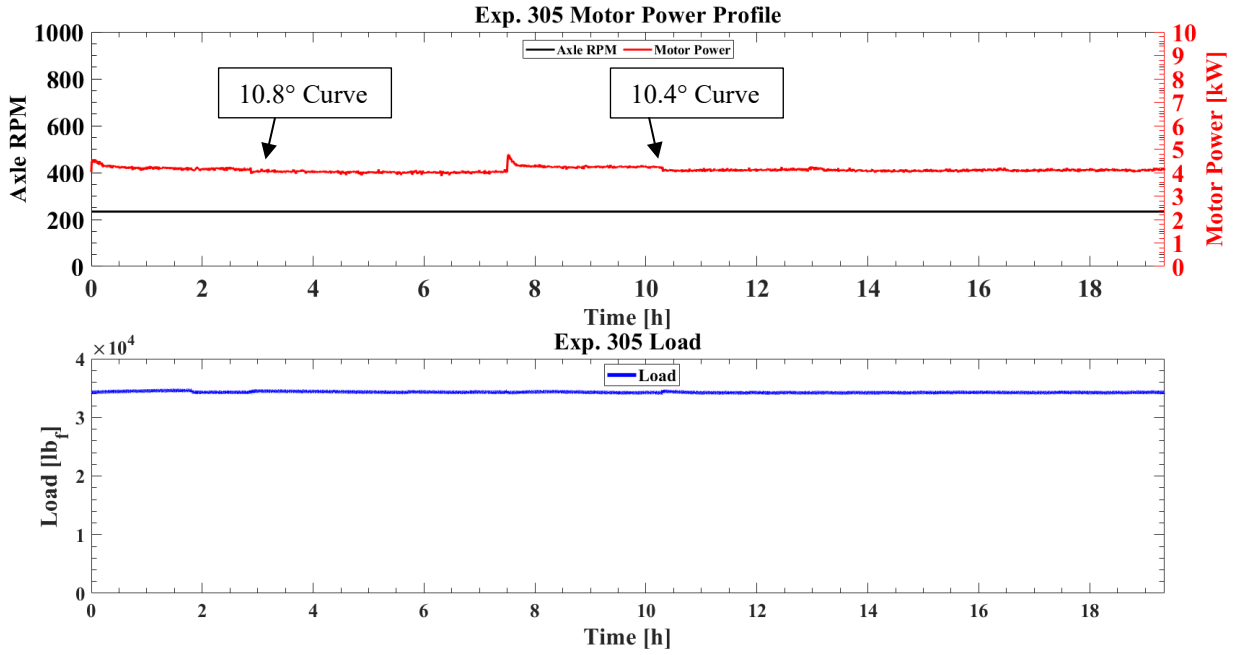

Figure 62. Control bearing motor power and vertical load at 40 kph (25 mph) for 100% load (fully loaded railcar) with varying lateral loads

Table 12. Lateral response summary of a control bearing operating at 40 kph (25 mph) for 100% load (fully loaded railcar)

F_{lat} [kN] / [kips]	Max ΔT [ºC] / [ºF]	Avg. ΔT [ºC] / [ºF]	Accel. [G_{RMS}]	Power [kW]	Disp. [mm] / [in]	ΔT / F_{lat} [ºC/kN] / [ºC/kips]
0	24.0 / 43.2	24.0 / 43.2	0.7	4.1	0.076 / 0.003	-
10.7 / 2.4	24.6 / 44.3	24.3 / 43.7	0.6	3.9	0.737 / 0.029	0.07 / 0.3
8.0 / 1.8	24.2 / 43.6	24.1 / 43.4	0.6	4.2	0.457 / 0.018	0.02 / 0.1

APPENDIX C

APPENDIX C

DEFECTIVE BEARING LATERAL LOADING CASES

Effects of Lateral Load at 97 kph (60 mph) and Unloaded Railcar

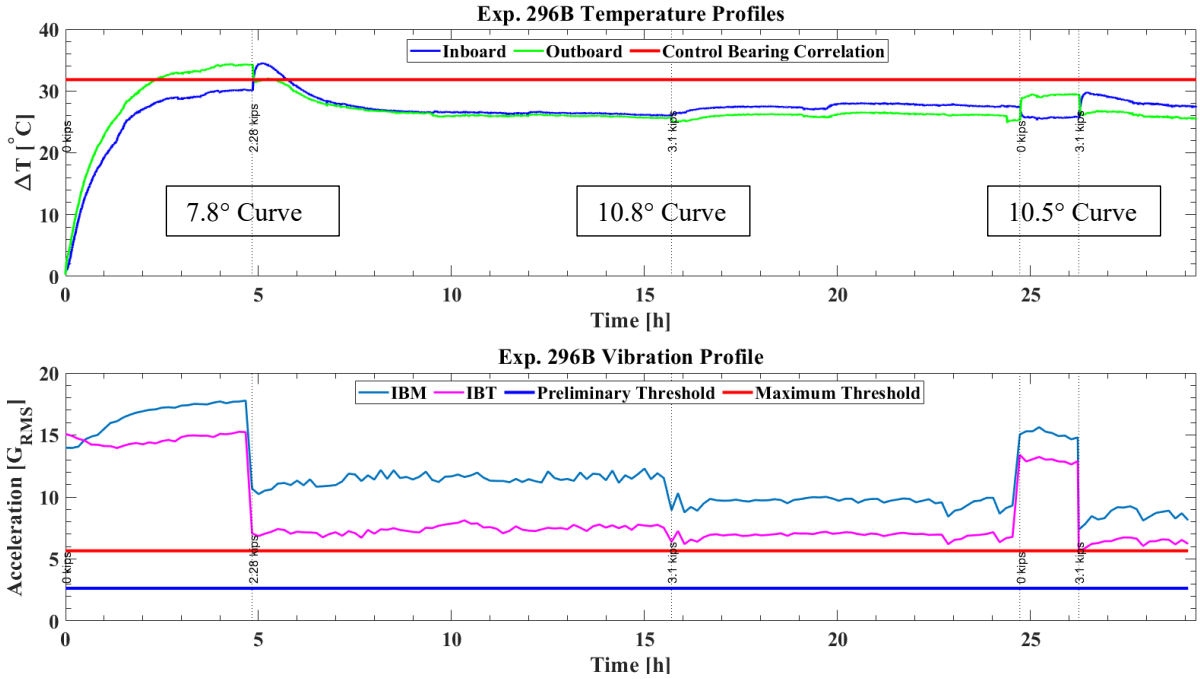

Figure 63. Defective bearing temperature and acceleration at 97 kph (60 mph) for 17% load (unloaded railcar) with varying lateral loads

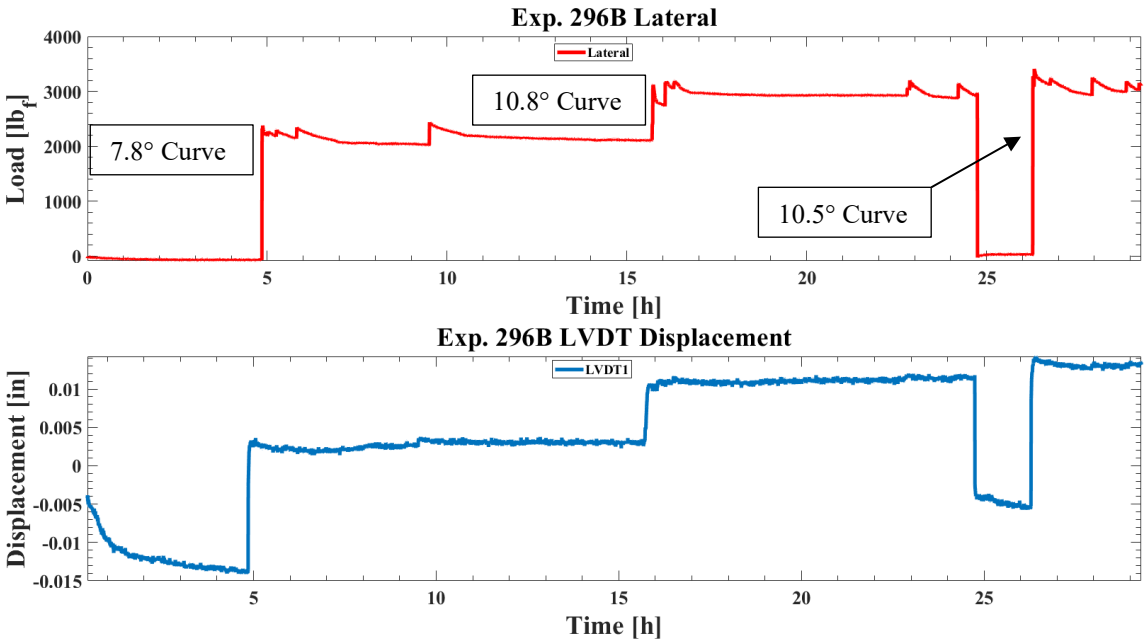

Figure 64. Defective bearing lateral load and displacement at 97 kph (60 mph) for 17% load (unloaded railcar) with varying lateral loads

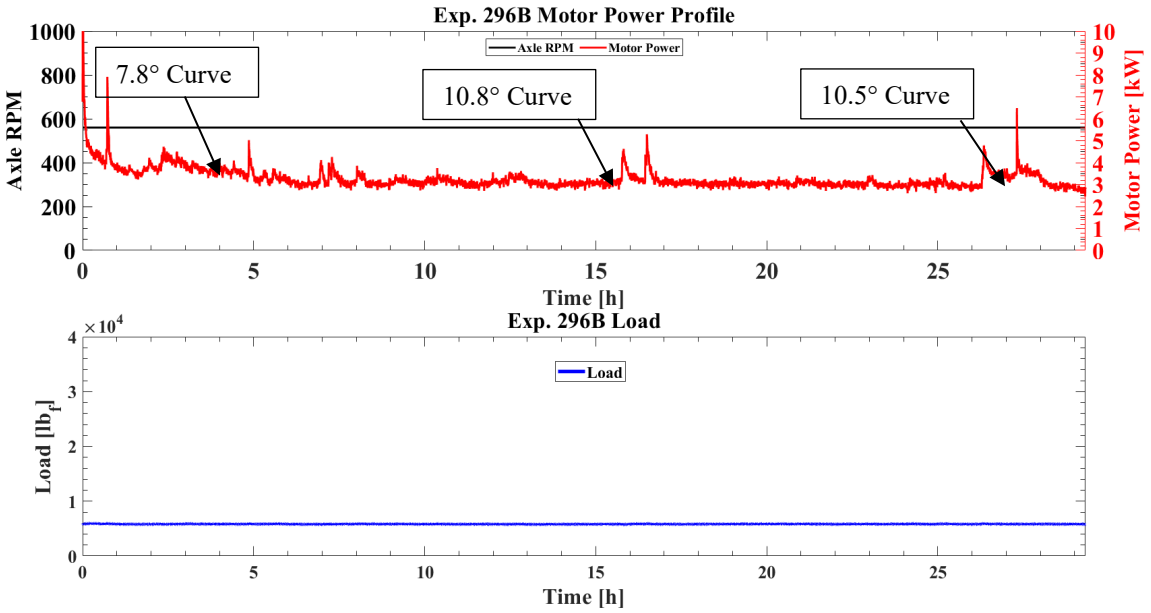

Figure 65. Defective bearing motor power and vertical load at 97 kph (60 mph) for 17% load (unloaded railcar) with varying lateral loads

Table 13. Lateral response summary of a defective bearing operating at 97 kph (60 mph) for 17% load (unloaded railcar)

F_{lat} [kN] / [kips]	Max ΔT [ºC] / [ºF]	Avg. ΔT [ºC] / [ºF]	Accel. [G_{RMS}]	Power [kW]	Disp. [mm] / [in]	ΔT / F_{lat} [ºC/kN] / [ºC/kips]
0	34.2 / 61.6	34.2 / 61.6	17.5	3.7	-0.305 / -0.012	-
10.1 / 2.3	34.5 / 62.1	33.5 / 60.3	11.8	3.5	0.051 / 0.002	0.20 / 0.9
13.8 / 3.1	27.4 / 49.3	30.8 / 55.4	9.5	3.2	0.254 / 0.010	-0.49 / -2.2
13.8 / 3.1	29.4 / 52.9	31.8 / 57.2	9	3.3	0.330 / 0.013	-0.34 / -1.5

Effects of Lateral Load at 72 kph (45 mph) and Unloaded Railcar

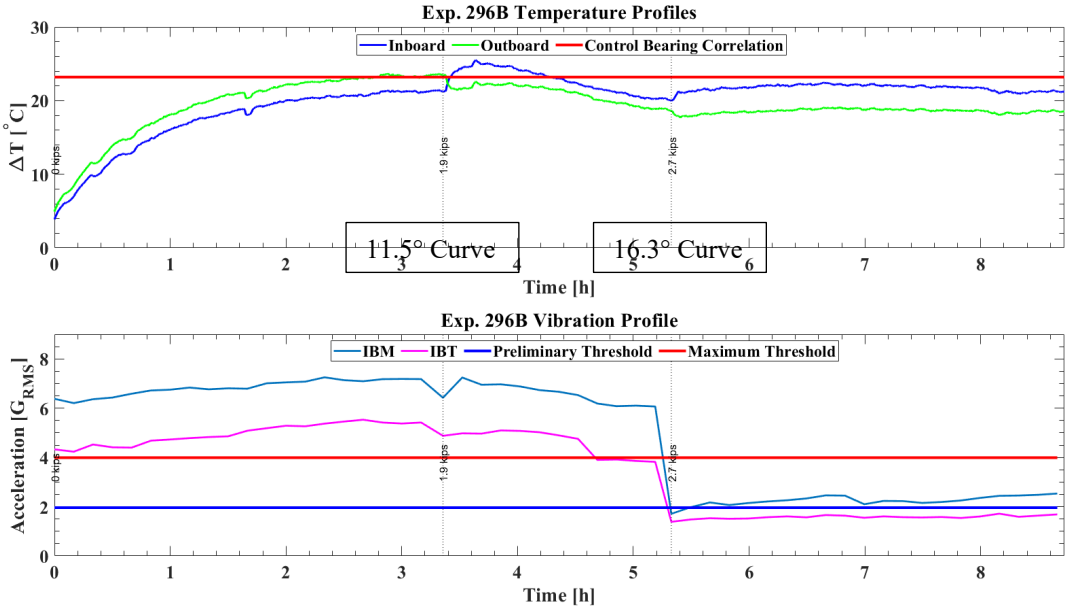

Figure 66. Defective bearing temperature and acceleration at 72 kph (45 mph) for 17% load (unloaded railcar) with varying lateral loads

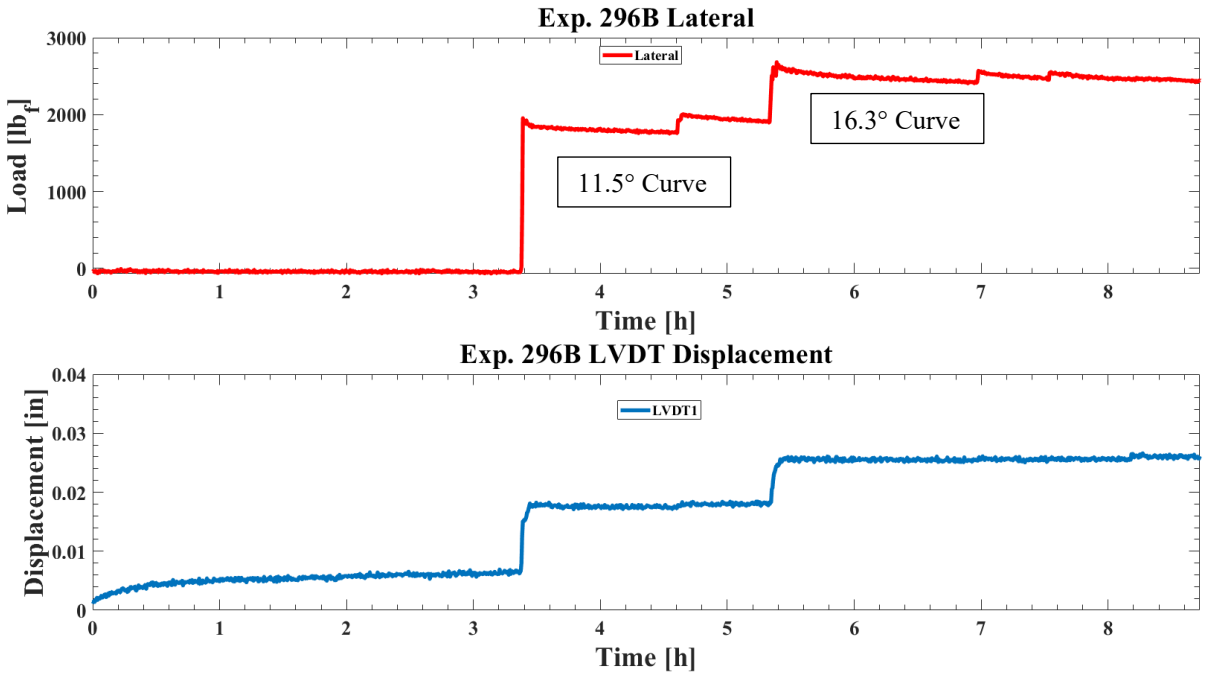

Figure 67. Defective bearing lateral load and displacement at 72 kph (45 mph) for 17% load (unloaded railcar) with varying lateral loads

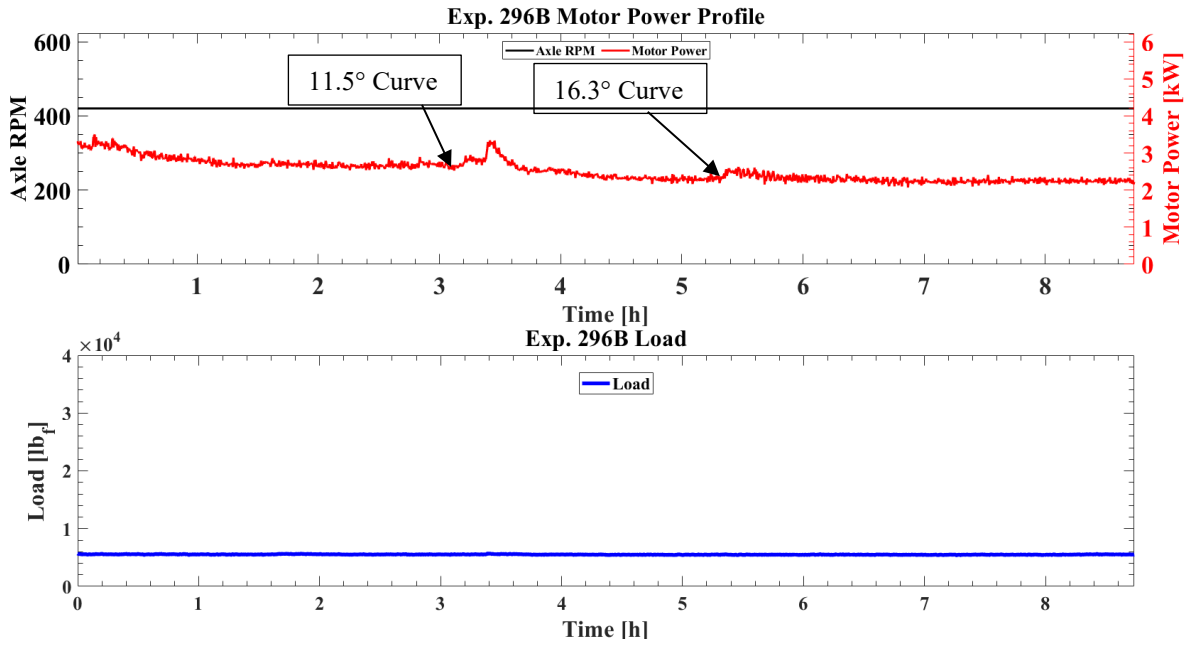

Figure 68. Defective bearing motor power and vertical load at 72 kph (45 mph) for 17% load (unloaded railcar) with varying lateral loads

Table 14. Lateral response summary of a defective bearing operating at 72 kph (45 mph) for 17% load (unloaded railcar)

F_{lat} [kN] / [kips]	Max ΔT [°C] / [°F]	Avg. ΔT [°C] / [°F]	Accel. [G_{RMS}]	Power [kW]	Disp. [mm] / [in]	ΔT / F_{lat} [°C/kN] / [°C/kips]
0	23.7 / 42.7	23.7 / 42.7	7.2	2.7	0.102 / 0.004	-
8.5 / 1.9	25.2 / 45.4	24.5 / 44.1	6.5	2.9	0.432 / 0.017	0.18 / 0.8
12.0 / 2.7	22.5 / 40.5	23.1 / 41.6	2.3	2.4	0.635 / 0.025	-0.09 / -0.4

Effects of Lateral Load at 40 kph (25 mph) and Fully Loaded Railcar

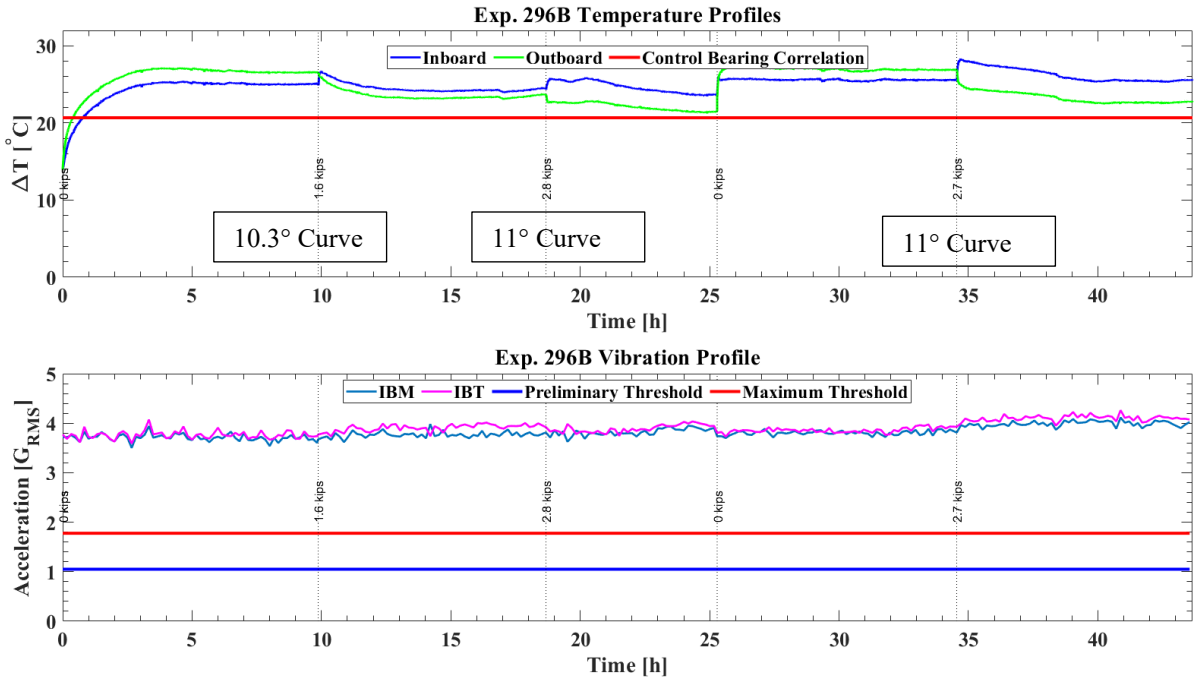

Figure 69. Defective bearing temperature and acceleration at 40 kph (25 mph) for 100% load (fully loaded railcar) with varying lateral loads

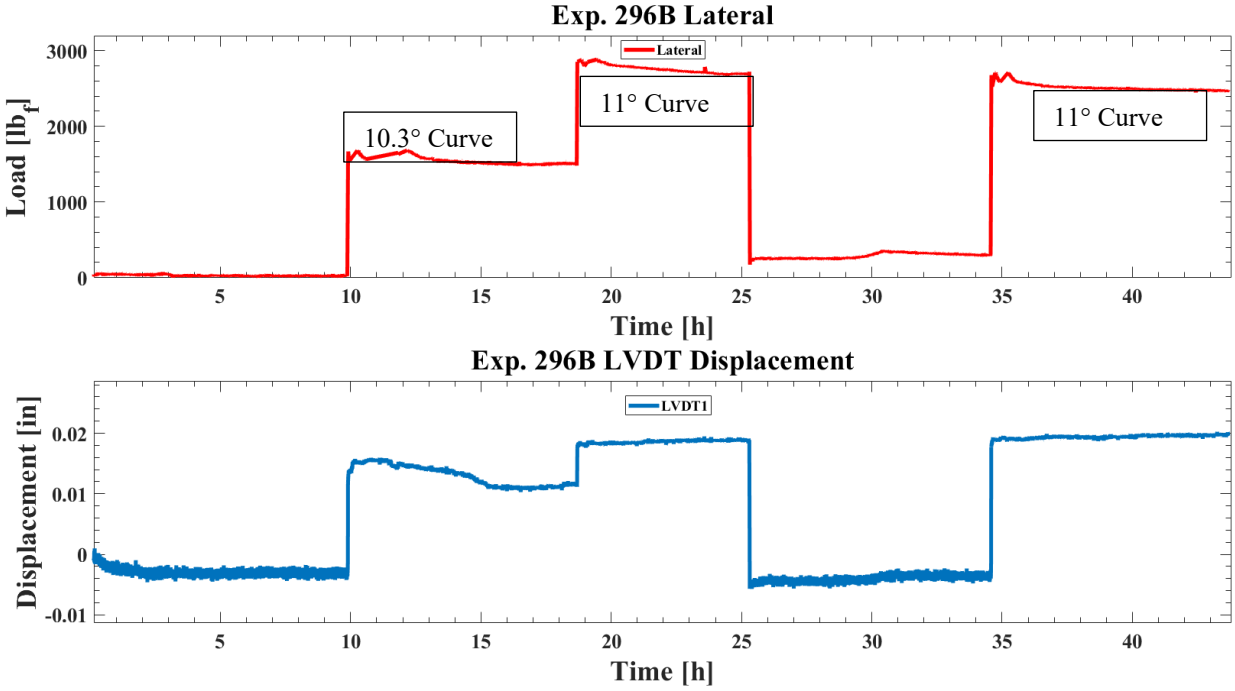

Figure 70. Defective bearing lateral load and displacement at 40 kph (25 mph) for 100% load (fully loaded railcar) with varying lateral loads

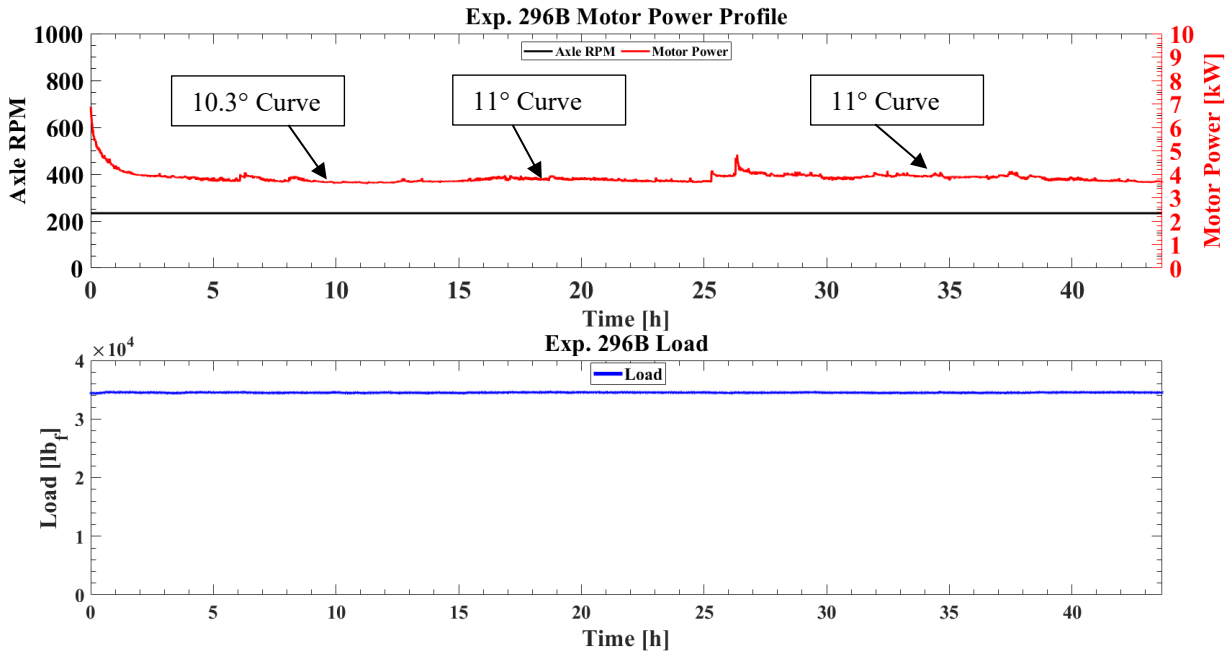

Figure 71. Defective bearing motor power and vertical load at 40 kph (25 mph) for 100% load (fully loaded railcar) with varying lateral loads

Table 15. Lateral response summary of a defective bearing operating at 40 kph (25 mph) for 100% load (fully loaded railcar)

F_{lat} [kN] / [kips]	Max ΔT [ºC] / [ºF]	Avg. ΔT [ºC] / [ºF]	Accel. [G_{RMS}]	Power [kW]	Disp. [mm] / [in]	ΔT / F_{lat} [ºC/kN] / [ºC/kips]
0	25.0 / 45.0	25 / 45.0	3.7	3.9	0.076 / 0.003	-
7.1 / 1.6	26.5 / 47.7	25.8 / 46.4	3.8	3.6	0.381 / 0.015	0.20 / 0.9
12.5 / 2.8	25.5 / 45.9	25.3 / 45.5	3.8	3.7	0.457 / 0.018	0.04 / 0.2
12.0 / 2.7	27.8 / 50.0	26.4 / 47.5	4	3.9	0.483 / 0.019	0.22 / 1.0

VITA

Abel David Sanchez Trinidad attended the University of Texas Rio Grande Valley (UTRGV) and received his Bachelor of Science in Mechanical Engineering in December 2023. Abel joined the RGV Baja Racing Team in 2018 and later became Captain of the team from 2020 to 2025. In 2021, he joined the University Transportation Center for Railway Safety (UTCRS), where he conducted research on the performance of reconditioned freight bearings. After obtaining his bachelor's degree, he continued his studies at UTRGV and his research with UTCRS to obtain a Master of Science in Mechanical Engineering in May 2026. Abel can be reached by email at abel.santri24@outlook.com.